Fall 2020

Artificial Intelligence Approaches for Structural Health Monitoring of Aerospace Structures

Kimberly A. Cardillo

Recommended Citation

Cardillo, K. A.(2020). *Artificial Intelligence Approaches for Structural Health Monitoring of Aerospace Structures.* (Master's thesis). Retrieved from https://scholarcommons.sc.edu/etd/6149

ARTIFICIAL INTELLIGENCE APPROACHES FOR STRUCTURAL HEALTH MONITORING OF AEROSPACE STRUCTURES

by

Kimberly A. Cardillo

Bachelor of Science
University of South Carolina, 2019

Submitted in Partial Fulfillment of the Requirements

For the Degree of Master of Science in

Mechanical Engineering

College of Engineering and Computing

University of South Carolina

2020

Accepted by:

Victor Giurgiutiu, Director of Thesis

Lingyu Yu, Reader

Cheryl L. Addy, Vice Provost and Dean of the Graduate School

DEDICATION

I would like to dedicate my hard work, desire to learn, and determination to accomplish excellence to my mother. Growing up, her love and words of wisdom she shared with me have always kept me moving towards my goals. She will always be in my heart in everything I strive for and achieve in life. Rest in peace to my beautiful angel.

ACKNOWLEDGEMENTS

I would like to thank my research advisor, Dr. Victor Giurgiutiu for his support and guidance for these past two years. Not only have you created a community in LAMSS, you have pushed everyone, including myself, past their comfort zone to explore the vast things we are capable of and I will be forever grateful. You have made me a better learner, thinker and professional. I am extremely blessed for everything you have provided for me.

I would also like to thank all my LAMSS colleagues for all their support and welcoming me into LAMSS and helping me to feel comfortable. Without everyone’s help and guidance, I would not have been able to achieve the goals I had made when first joining research.

I would also like to thank my father who has always been my number one fan. Dad, you are my rock and I will always appreciate everything you have taught me and done for me. Lastly, I would like to thank my friends who always supported me throughout my time here at research.

ABSTRACT

Structural health monitoring (SHM) and non-destructive evaluation (NDE) have been a significant research topic to help with damage detection in aerospace structures. SHM and NDE techniques are based on extracting damage sensitive features to determine the criticality of damage and lifetime of a structure. Acoustic emission (AE) signal detection is an important technique in SHM and NDE especially for fatigue crack growth. AE signals for thin aerospace structures consist of ultrasonic guided Lamb waves that propagate through the structure. This thesis focuses on AE signal repeatability, load at which AE signals occur, feature extraction, artificial intelligence and electro-mechanical impedance of a piezoelectric wafer active sensor (PWAS) in response to a crack in thin aerospace structures. The artificial intelligence techniques explored include machine learning model classification and deep learning classical and convolutional neural networks designed to understand the meaning behind each AE signal that comes from a fatigue crack.

The goal of this research is to distinguish AE signals from fatigue growing cracks into two categories; crack face rubbing and crack growth. From there, we want to determine the crack length based on the AE signal. With the understanding of the AE signal and artificial techniques created from this research, when applied to industry, we will be able to locate cracks on an aerospace structure and determine whether the structure needs maintenance before it results in catastrophic failure.

TABLE OF CONTENTS

DEDICATION iii

ACKNOWLEDGEMENTS iv

ABSTRACT v

LIST OF TABLES ix

LIST OF FIGURES x

LIST OF SYMBOLS xv

LIST OF ABBREVIATIONS xvii

CHAPTER 1 PIEZOELECTRIC WAFER ACTIVE SENSOR 1

- 1.1 INTRODUCTION TO SENSING TECHNIQUES 1
- 1.2 PIEZOELECTRIC CONSTITUTIVE EQUATIONS AND ADMITTANCE EQUATION 2
- 1.3 STATISTICAL SIGNIFICANCE FOR EXPERIMENTAL RESULTS 3
- 1.4 EXPERIMENTAL SET-UP AND PROCEDURE 4
- 1.5 DATA AND ERROR ANALYSIS FOR THE TWO EXPERIMENTS 8
- 1.6 SUMMARY AND CONCLUSIONS 14

CHAPTER 2 LOW CYCLE FATIGUE CRACK EXPERIMENT TO CAPTURE AE SIGNALS 16

- 2.1 INTRODUCTION 16
- 2.2 STATE OF THE ART FEATURE EXTRACTION FOR ALUMINUM 2024 18
- 2.3 EXPERIMENTAL SET-UP 25

2.4 EXPERIMENTAL PROCEDURE FOR LCF CRACK GROWTH 29

2.5 EXPERIMENTAL RESULTS 30

2.6 SUMMARY AND CONCLUSIONS 41

CHAPTER 3 INTRODUCTION TO ARTIFICIAL INTELLIGENCE TECHNIQUES 44

3.1 ARTIFICIAL INTELLIGENCE STATE OF THE ART 44

3.2 MACHINE LEARNING CLUSTERING TECHNIQUES 46

3.3 MACHINE LEARNING CLASSIFICATION MODELS 50

3.4 DEEP LEARNING NEURAL NETWORKS 55

CHAPTER 4 MACHINE LEARNING FEATURE EXTRACTION AND MODEL CLASSIFICATION FOR EXPERIMENTAL AE SIGNALS 60

4.1 EXPERIMENTAL SET-UP AND PROCEDURE 61

4.2 SIGNAL DETECTION PROCESSING: FEATURE EXTRACTION 62

4.3 PRINCIPAL COMPONENT ANALYSIS 69

4.4 CLASSIFICATION MODELING 72

4.5 SUMMARY AND CONCLUSIONS 74

CHAPTER 5 DEEP LEARNING CLASSICAL AND CONVOLUTIONAL NEURAL NETWORKS 75

5.1 INTRODUCTION 75

5.2 EXPERIMENTAL PROCEDURE AND DATA 75

5.3 CLASSICAL NEURAL NETWORK: LSTM 76

5.4 CONVOLUTIONAL NEURAL NETWORKS 77

5.5 SUMMARY AND CONCLUSIONS 81

CHAPTER 6 SUMMARY AND CONCLUSIONS 84

6.1 FUTURE WORK 85

6.2 MAJOR CONTRIBUTIONS 88

REFERENCES 90

LIST OF TABLES

Table 1.1 RMSD, MAPD, and CC values for the three frequency ranges....10

Table 1.2 RMSD, MAPD, and CC values for the smaller frequency ranges....12

Table 1.3 Percent difference of bonding condition slopes and free PWAS slopes....14

Table 4.1 Features that distinguish between T1 and T2 signals....64

Table 4.2 Features and hit numbers table for T1, T2 and noise AE signals....68

LIST OF FIGURES

Figure 1.1 Device used to simulate a 'free' PWAS. 5

Figure 1.2 Experimental set-up including the 'free' PWAS, and EMIS machine and software. 6

Figure 1.3 Five PWAS damage location specimen. 7

Figure 1.4 Aluminum specimen with various PWAS bonding quality conditions. 8

Figure 1.5 Plots of real impedance at (a) 10-40 kHz, (b) 10-150 kHz, and (c) 300-450 kHz. 9

Figure 1.6 Plots of the real impedance at ranges of (a) 22-27 kHz, and (b) 58-68 kHz. 11

Figure 1.7 Comparison between free and bonded PWAS. 13

Figure 1.8 Representation of the method used to find a best fit line. 13

Figure 1.9 Plot of the slopes of the best fit line for each specimen. 14

Figure 2.1 Diagram of fatigue specimen with a PWAS 5 mm from the crack. [19] 19

Figure 2.2 AE hits captured by the PWAS with simultaneous load readings. [19] 20

Figure 2.3 Description of load level at which group A and group B occurred at. [19] 21

Figure 2.4 (a) Time and frequency domain of a typical group A waveform, (b) time and frequency domain of a typical group B waveform. [19] 21

Figure 2.5 Time and frequency domain for group C. [19] 22

Figure 2.6 (a) Actual group D waveform, (b) denoised group D waveform, (c) frequency domain for group D. [19] 23

Figure 2.7 Time and frequency domain for group E. [19] 24

Figure 2.8 Time and frequency domain for group F. [19] 24

Figure 2.9 Time and frequency domain for group G. [19]......................................25

Figure 2.10 Time and frequency domain for group H. [19]......................................25

Figure 2.11 Side 1 and side 2 of specimen with applied NRB and sensors......................................28

Figure 2.12 Experimental set-up of all devices used to help monitor and conduct the LCF experiment.......................................28

Figure 2.13 Picture of specimen loaded in the MTS machine prior to testing......................................29

Figure 2.14 Detailed methodology of machinery and instrumentation used in LCF experiment. 30

Figure 2.15 Crack initiation and crack growth data tables......................................31

Figure 2.16 Eddy current measurements at (a) ~21 mm, (b) ~22.5 mm, and (c) ~23 mm. 32

Figure 2.17 Sensor hits and loading for 60 cycles with loading frequency of 0.5 Hz. 33

Figure 2.18 Sensor hits and loading for 10 cycles with loading frequency of 0.5 Hz assigned to groups 1 or 2. 34

Figure 2.19 Group 1 waveform for (a) near field PWAS 1, (b) near field S9225 1, (c) far field PWAS 2, and (d) far field S9225 2 with loading frequency of 0.5 Hz. 35

Figure 2.20 Group 2 waveform for (a) near field PWAS 1, (b) near field S9225 1, and (c) far field PWAS 2 with loading frequency of 0.5 Hz. 35

Figure 2.21 Sensor hits and loading for 60 cycles with loading frequency of 0.25 Hz. 36

Figure 2.22 Sensor hits and loading for 10 cycles with loading frequency of 0.25 Hz assigned to groups 1 or 2. 36

Figure 2.23 Group 1 waveforms for (a) near field PWAS 1, (b) near field S9225 1, (c) far field PWAS 2, and (d) far field S9225 2 with loading frequency of 0.25 Hz. 37

Figure 2.24 Group 2 waveforms for (a) near field PWAS 1, and (b) near field S9225 1 with loading frequency of 0.25 Hz. 37

Figure 2.25 Sensor hits and loading for 60 cycles with loading frequency of 0.1 Hz. 38

Figure 2.26 Sensor hits and loading for 10 cycles with loading frequency of 0.1 Hz assigned to group 1. 39

Figure 2.27 Group 1 waveforms for (a) near field PWAS 1, (b) near field S9225 1, (c) far field PWAS 2, and (d) far field S9225 2 with loading frequency of 0.1 Hz. 39

Figure 2.28 Normalized hit and normalized load for 60 cycles for AE hits from all sensors with loading frequency of 0.07 Hz. 40

Figure 2.29 10 cycles with waveforms assigned to either group 1 or 2 with loading frequency of 0.07 Hz. 41

Figure 2.30 Group 1 waveform for (a) near field PWAS 1, (b) near field S9225 1, (c) far field PWAS 2, and (d) far field S9225 2 with loading frequency of 0.07 Hz. 43

Figure 2.31 Group 2 waveform for (a) near field PWAS 1, and (b) near field S9225 1 with loading frequency of 0.07 Hz. 43

Figure 3.1 Hierarchical tree split into clusters based on relative distance. 48

Figure 3.2 (a) Linear principal components viewed on the original axis and (b) the principal components shown as the new coordinate system. [38] 50

Figure 3.3 (a) Linear discriminant analysis and (b) quadratic discriminant analysis. [38] 52

Figure 3.4 SVM clustering for (a) arbitrary hyperplanes, and (b) optimal hyperplane. [39] 53

Figure 3.5 Example of k-nearest neighbor clustering. [38] 54

Figure 3.6 (a) Classified data split into various boundaries, and (b) decision tree binary sequence used to cluster new data. [38] 55

Figure 3.7 (a) Gaussian Mixture model distributions for testing data and (b) new data point probability based on Naïve Bayes classification model. [38] 56

Figure 3.8 Multilayer perception (MLP). [39] 56

Figure 3.9 Structure of the LSTM neural network. 58

Figure 3.10 General construction of a convolutional neural network. 59

Figure 4.1 (a) AE sensor side of the specimen, (b) strain gauge side of the specimen, and (c) sensor side of the specimen with sensor distances from the crack. 62

Figure 4.2 Methodology for HCF testing in the MTS machine. 62

Figure 4.3 (a) Typical T1 signal at ~7 mm and (b) typical T2 signal at ~7 mm. 64

Figure 4.4 (a) Parallel coordinate plot to help distinguish features and (b) parallel coordinate plot to help distinguish the median of features. 69

Figure 4.5 (a) PCA plot for 4-48 kcycles and crack length of 3.5-8 mm and (b) Pareto chart describing the variance of the first four principal components. 70

Figure 4.6 *k*-means clustering results based on first and second principal component. 71

Figure 4.7 Hierarchical clustering of crack-related hits. 71

Figure 4.8 (a) Scatter plot, and (b) confusion matrix for test data with 100% classification accuracy for KNN, DT, and SVM models. 73

Figure 4.9 (a) Scatter plot, and (b) confusion matrix for test data with 84.26% classification accuracy for NB model. 73

Figure 4.10 (a) Scatter plot, and (b) confusion matrix for test data with 96.06% classification accuracy for DA model. 74

Figure 5.1 Training process for frequency domain LSTM network. 79

Figure 5.2 Confusion matrix for test data run through trained frequency domain LSTM network. 79

Figure 5.3 Example Choi William transforms for crack-related and noise AE signals. 80

Figure 5.4 Pretrained convolutional neural network called AlexNet. 81

Figure 5.5 (a) Montage of convolutional layer 1 from pretrained AlexNet neural network, (b) a close up of green-activating filter 79, (c) input of hit #27, and (d) hit #27 activated with filter 79. 82

Figure 5.6 Accuracy and loss graphs for training convolutional neural. 82

Figure 5.7 Confusion matrix of the testing data run through the trained network. 83

LIST OF SYMBOLS

Y	Distance between two features.
F	Ending point of a feature vector.
C	Derived clusters.
L	Linkage calculation.
Σ	Covariance matrix.
$\boldsymbol{x}$, $\underline{\boldsymbol{x}}$	Feature vector.
$\overline{\boldsymbol{x}}$, $\underline{\overline{\boldsymbol{x}}}$	Mean of the feature vector.
A	Transformation matrix.
$\{z\}_i$	Variance component for i =1, 2, 3…n where i =1 is the highest variance component and n is the number of features.
d	Number of dimensions for discriminant analysis.
p_{max}	Maximum value of the distance between the mean of a feature vector and the furthest data point.
k	Layer number for multi-layer perception in neural networks.
$z_i^{(k)}$	Excitation of a node in multi-layer perception.
ω_{ij}	Weight in regard to multi-layer perception.
$D(\{x\})$	Support vector machine variable.
α_i	Lagrange multipliers for support vector machines.
y_i	Cluster label for support vector machines.
$v(\{\boldsymbol{x}\})$	Novelty index for outlier analysis.
S_i	Mechanical strain.

s_{ij}^{E}	Mechanical compliance holding electric field constant.
T	Mechanical stress.
d_{mi}	Piezoelectric coupling constant.
E	Electric field.
D_m	Charge density.
ε_{mk}^{T}	Dielectric constant holding mechanical stress constant.
Y_{free}	Admittance of a ‘free’ PWAS.
ω	Angular frequency.
w	Width of the PWAS.
l	Length of the PWAS.
t_c	Thickness of the PWAS.
δ	Dielectric loss that is tangent to the PWAS transducer.
$Z_a(\omega)$	Mechanical impedance of the sensor.
$Z_s(\omega)$	Mechanical impedance of the structure or host.
Y_p^{E}	Young’s modulus of the sensor with no electric field.
σ_Z	Standard deviation.
$Re(Z_k)$	Real impedance value.
$\underline{Z}$	Mean real impedance value.

LIST OF ABBREVIATIONS

AE	Acoustic Emission
AI	Artificial Intelligence
CC	Correlation Coefficient
DA	Discriminant Analysis
DT	Decision Tree
FFT	Fast Fourier Transform
GP	Gaussian Process
GUI	Graphical User Interface
HCF	High Cycle Fatigue
KDF	Kernel Density Function
KNN	K-Nearest Neighbor
LCF	Low Cycle Fatigue
LSTM	Long Short-Term Memory
MAPD	Mean Absolute Percentage Deviation
MFC	Micro-Fiber Composite
ML	Machine Learning
MLP	Multi-Layer Perception
NB	Naïve Bayes
NDE	Non-Destructive Evaluation
NRB	Non-Reflective Boundary

PCA	Principal Component Analysis
PCC	Pearson Correlation Coefficient
PLB	Pencil Lead Break
PR	Pattern Recognition
PWAS	Piezoelectric Wafer Active Sensor
PZT	Piezoelectric Transducer
ReLU	Rectified Linear Unit
RGB	Red, Green, Blue
RMSD	Root Mean Square Deviation
RUL	Remaining Useful Life
SIF	Stress Intensity Factor
SHM	Structural Health Monitoring
SLDV	Scanning Laser Doppler Vibrometer
SVM	Support Vector Machines

CHAPTER 1

PIEZOELECTRIC WAFER ACTIVE SENSOR

There are many methods that are used for detecting acoustic emission (AE) signals and it is important to find the method that best suits your application. Variations in methodology could include capturing of in-plane or out-of-plane ultrasonic waves, size of sensor, frequency range, etc. The methods used for detecting AE are either passive or active techniques. Piezoelectric wafer active sensors (PWAS), S9225 sensors and PICO sensors were compared experimentally based on the hit- and waveform-based analysis due to an AE source [1], [2]. R15α is another common sensor and was used to collect AE data from pencil led breaks (PLB) as well as ball drops on a C-beam used in steel bridges [3]. Fiber Bragg grating sensors were used to evaluate the frequency and transient response of the AE source on an aluminum panel [4]. Scanning laser Doppler vibrometers (SLDV) used a laser to detect AE, which reduces the need to apply a sensor to your specimen [5]. All these sensing methods were used to detect AE in a specimen through the active or passive sensing of ultrasonic Lamb waves.

1.1 INTRODUCTION TO SENSING TECHNIQUES

AE sensors can be used to evaluate the damage of a specimen or the bonding quality of the sensor through electro-mechanical impedance. Changes in the electrical admittance of piezoelectric (PZT) sensors due to debonding on a graphite/epoxy-fiber-reinforced composite plate was experimentally evaluated [6]. Different bonding conditions of PWAS were evaluated with the imaginary part of the admittance on an aluminum washer as well as the real part of the impedance on an aluminum surface [7].

The admittance of a PWAS can give information about the bonding quality or damage of the sensor itself, but the admittance has been known to help determine the damage of the host structure. The admittance of a PWAS due to damage detection at various distances from the sensor was theoretically and experimentally examined and numerical significance has been provided for the experimental results [8]. A further investigation of the numerical significance of the impedance of a PWAS is seen in the following section.

1.2 PIEZOELECTRIC CONSTITUTIVE EQUATIONS AND ADMITTANCE EQUATION

To understand the admittance or impedance measurements of a piezoelectric wafer active sensor (PWAS), it is important to understand and comprehend the piezoelectric constitutive equations. By manipulating the constitutive equations, a theoretical equation can be obtained for the admittance or impedance of a PWAS.

An understanding of a piezoelectric wafer active sensor (PWAS) comes from the basic electro-mechanical properties it has. In simple terms, as a PWAS is mechanically stretched or compressed, it produces an electrical response. It will also produce a mechanical response (stretching or compressing) when an electrical signal is applied to it. The basic constitutive equations that prove this relationship are seen in equation (1) below.

$$\begin{gathered} S_i = s_{ij}^E T_j + d_{mi} E_m \\ D_m = d_{mi} T_i + \varepsilon_{mk}^T E_k \end{gathered} \tag{1}$$

where *S* is the mechanical strain, *T* is the mechanical stress, *E* is the electric field, *D* is the charge density, *s* is the mechanical compliance, *d* is the piezoelectric coupling constant, and ε is the dielectric constant of the PWAS. The subscripts *i, j, m* and *k* indicate the direction of stress, strain or electric field. The admittance of the PWAS originates from the current running through the transducer. The current can be found by taking the derivative of the charge density with respect to time and integrating it over the area of the transducer. Knowing the admittance is equal to the current, *I*, over the applied voltage, *V*, the final equation can be found in equation (2). This is the admittance of a 'free' PWAS, meaning it is not bonded or touching any other surface.

$$Y_{free}(\omega) = i\omega \frac{wl}{t_c}\left[\varepsilon_{33}^{T}(1 - i\delta)\right] \tag{2}$$

where ω is the angular frequency, δ is the dielectric loss that is tangent to the transducer, *w* is the width, *l* is the length, and t_c is the thickness of the transducer. A 'free' PWAS does not help with structural health monitoring (SHM) and is merely a reference for bonded cases. When a PWAS is bonded to a host structure, it changes the response of the transducer. The admittance of a bonded PWAS is affected by both the mechanical impedance of the structure as well as the mechanical impedance of the PWAS. The admittance of a bonded PWAS is seen in equation (3).

$$Y(\omega) = i\omega \frac{wl}{t_c}\left[\varepsilon_{33}^{T}(1 - i\delta) - d_{31}^{2} Y_{p}^{E} + \frac{Z_a(\omega)}{Z_a(\omega) + Z_s(\omega)} d_{31}^{2} \hat{Y}^{E} \left(\frac{\tan kl}{kl}\right)\right] \tag{3}$$

where Y_p^E is the Young's modulus of the PWAS with no electric field, *k* is the wave number of the transducer, $Z_a(\omega)$ is the mechanical impedance of the sensor, and $Z_s(\omega)$ is the mechanical impedance of the structure.

1.3 STATISTICAL SIGNIFICANCE FOR EXPERIMENTAL RESULTS

Admittance is more difficult to extract information from in comparison to the impedance because the real part of the admittance has many more resonances that may not be as significantly distinct as the imaginary part of the impedance, i.e. slope. Giurgiutiu et al. [8] numerically evaluate the real part of the impedance.

Giurgiutiu et al. [8] used the impedance method to introduce a good match between simulation and experimental results for PWAS distance from damage in thin circular aluminum plates. They used the real part of the impedance to determine at what distance a PWAS is from a slit in an aluminum plate where the PWAS is located at the center of the plate. To add numerical value to the results, they calculated the root mean square deviation (RMSD), mean absolute percentage deviation (MAPD), and correlation coefficient (CC). These equations are shown below.

$$RMSD = \sqrt{\sum_{k=1}^{N}[Re(Z_k)_j - Re(Z_k)_i]^2 / \sum_{k=1}^{N}[Re(Z_k)_i]^2} \tag{4}$$

$$MAPD = \frac{1}{N}\sum_{k=1}^{N}\left|[Re(Z_k)_j - Re(Z_k)_i]/Re(Z_k)_i\right| \tag{5}$$

$$CC = \frac{1}{N\sigma_{Z_j}\sigma_{Z_i}}\sum_{k=1}^{N}[Re(Z_k)_j - Re(\underline{Z})_j] * [Re(Z_k)_i - Re(\underline{Z})_i] \tag{6}$$

where $Re(Z_k)_i$ represents the real impedance values for the pristine specimen and $Re(Z_k)_j$ represents the corresponding real impedance values for the damaged specimen. N is the total number of points, $(\underline{Z})_i$ and $(\underline{Z})_j$ are the mean real impedance values of the pristine and damaged specimens respectively, and σ_{Z_i} and σ_{Z_j} signify the standard deviation of the pristine and damaged specimens, respectively.

1.4 EXPERIMENTAL SET-UP AND PROCEDURE

Two different experiments were conducted for the purpose of this paper. The first experiment involves gathering the real part of the impedance of PWAS with various damage locations. The second experiment involves gathering the imaginary part of the electrical admittance response for five different bonding conditions. The PWAS used are round, 7 mm diameter, 0.5 mm thick that are manufactured with positive and negative wires soldered to the electrodes. Both experiments used a device to resemble the 'free' PWAS condition and can be seen in Figure 1.1. This 'free' PWAS was used as a baseline for both experiments.

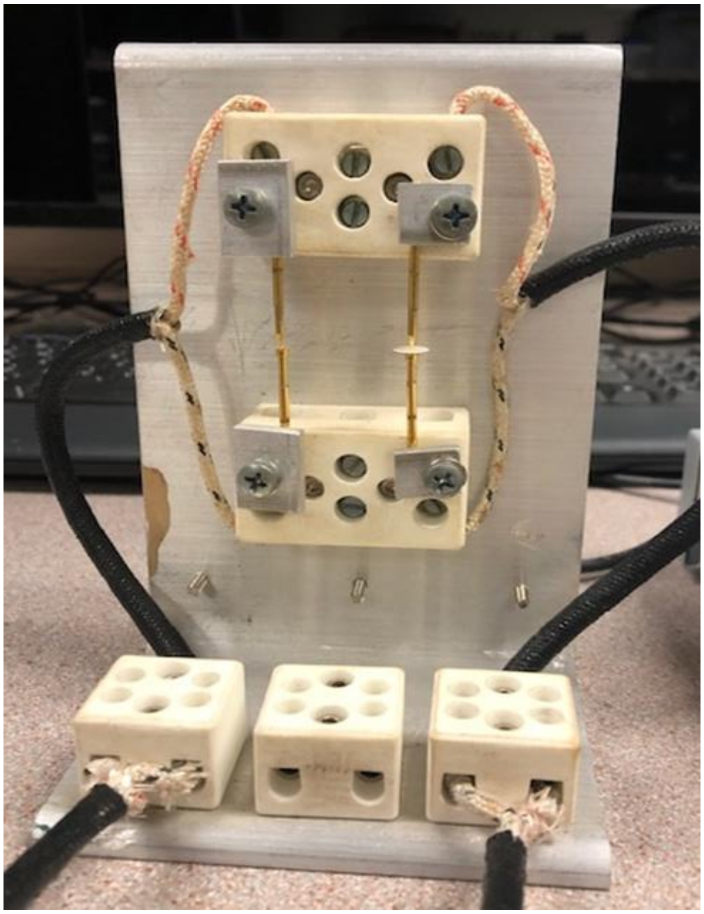

Figure 1.1 Device used to simulate a 'free' PWAS.

The experiments were set up so that the Omicron Electronics Impedance Analyzer Bode 100 was used to send signals and detect data in a PWAS with various damage locations or bond qualities. A wire with one end BNC connection and the other end with positive and negative connections was used to connect the positive and negative sided

PWAS to the Impedance Analyzer. The Impedance Analyzer was connected to a laptop through a USB connection. The Bode Analyzer Suite software on the laptop was used as the interface to measure and record the data. A picture of the experimental set-up can be found in Figure 1.2.

Figure 1.2 Experimental set-up including the ‘free’ PWAS, and EMIS machine and software.

1.4.1 Damage detection experimental set-up

In addition to the ‘free’ PWAS, five additional PWAS were bonded to round 1 mm thick Aluminum 2024-T6 specimens with a diameter of 10 cm. Each specimen had damage on it that resembles a crack of 10 mm in length. The first specimen was the pristine condition where there was no crack. The other four specimens had cracks 10 mm, 17 mm, 32 mm and 47 mm away from the PWAS. A picture of the specimen is found in Figure 1.3.

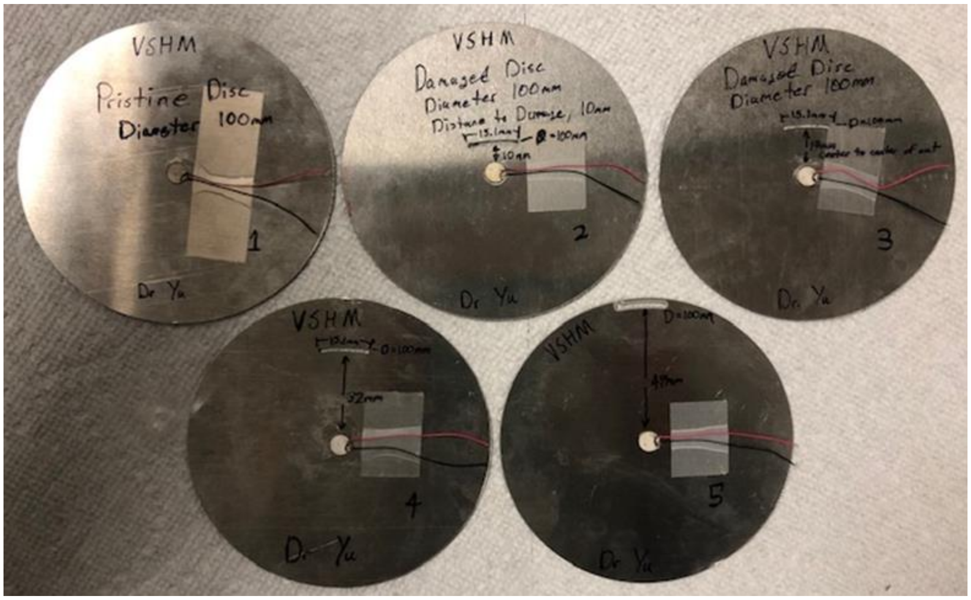

Figure 1.3 Five PWAS damage location specimen.

A single, linear sweep measurement was done from 10 kHz to 1 MHz with 1601 data points for the ‘free’, pristine, 10 mm, 17 mm, 32 mm and 47 mm damage locations. The real part of the impedance was very busy and hard to distinguish where the resonance peaks were located. For more refined results the procedure was repeated for three different ranges, 10-40kHz, 10-150kHz and 300-450kHz. This was repeated three times to ensure the readings were correct. The data was graphed in Python and analyzed to determine if there were significant properties and patterns. Some of the properties the results were analyzed for were location, amplitude, and shifting of frequency peaks as well as slope for the imaginary part.

1.4.2 Bonding quality experimental set-up

The five different bonds consist of a fully bonded PWAS, a PWAS that is 75% bonded, 50% bonded, 25% bonded and a PWAS that resembles a ‘free’ situation as seen in Figure 1.1. The other four conditions were bonded with M-Bond 200 to a 1 mm thick

Aluminum 2024-T6 specimen approximately 4 cm away from one another. A picture of the specimen can be found in Figure 1.4.

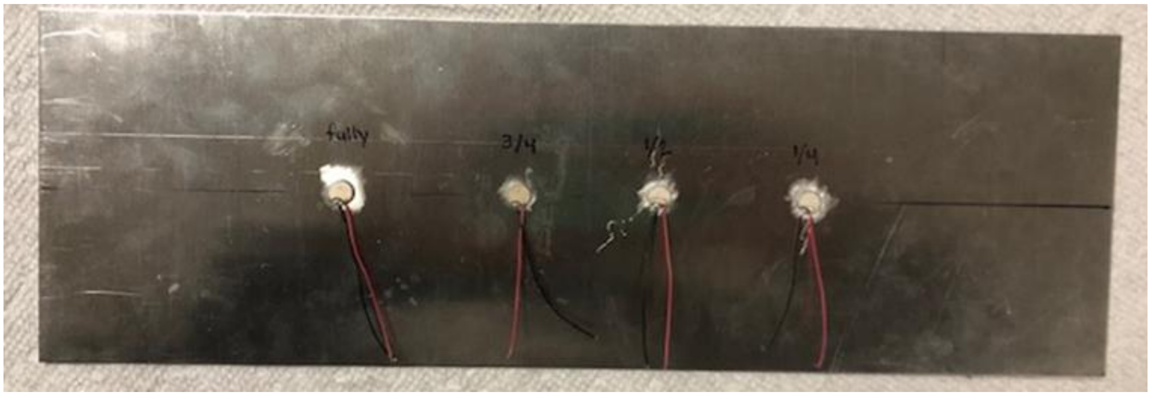

Figure 1.4 Aluminum specimen with various PWAS bonding quality conditions.

A single, linear sweep measurement was done from 10-40kHz for the imaginary part of the admittance with 1601 data points for the ‘free’, fully bonded, 75%, 50% and 25% bonded conditions. This was repeated three times to ensure the readings were correct. The data was graphed in Python and analyzed to determine if there were significant properties and patterns. Some of the properties the results were analyzed for were location, amplitude, and shifting of frequency peaks as well as slope for the imaginary part.

1.5 DATA AND ERROR ANALYSIS FOR THE TWO EXPERIMENTS

1.5.3 Assumptions made for post-processing purposes

Many assumptions were made to interpret the data that was collected. Since the quality of the bond is being explored, it is important to assume that only quality of the bond is affecting the electrical response of the PWAS. This means that the environmental effects are ignored. Environmental effects, such as temperature, humidity and pressure are ignored because they might influence the results. All data was collected in one sitting to keep environmental effects consistent. In real life applications, PWAS are typically bonded to a material such as Aluminum or composites, but the material is typically not resting on another surface. It is assumed that the table the specimen is resting on in these experiments does not affect the electrical response of the PWAS. Another important assumption is that for the second experiment, the admittance reading of one PWAS was not affected by another PWAS bonded beside it.

1.5.4 Results for damage detection in circular plates

Analysis started with plotting a large frequency range, and then selecting several smaller ranges based on observations. The ranges chosen are 10-40 kHz, 10-150 kHz, and 300-400 kHz all of which can be seen in Figure 1.5.

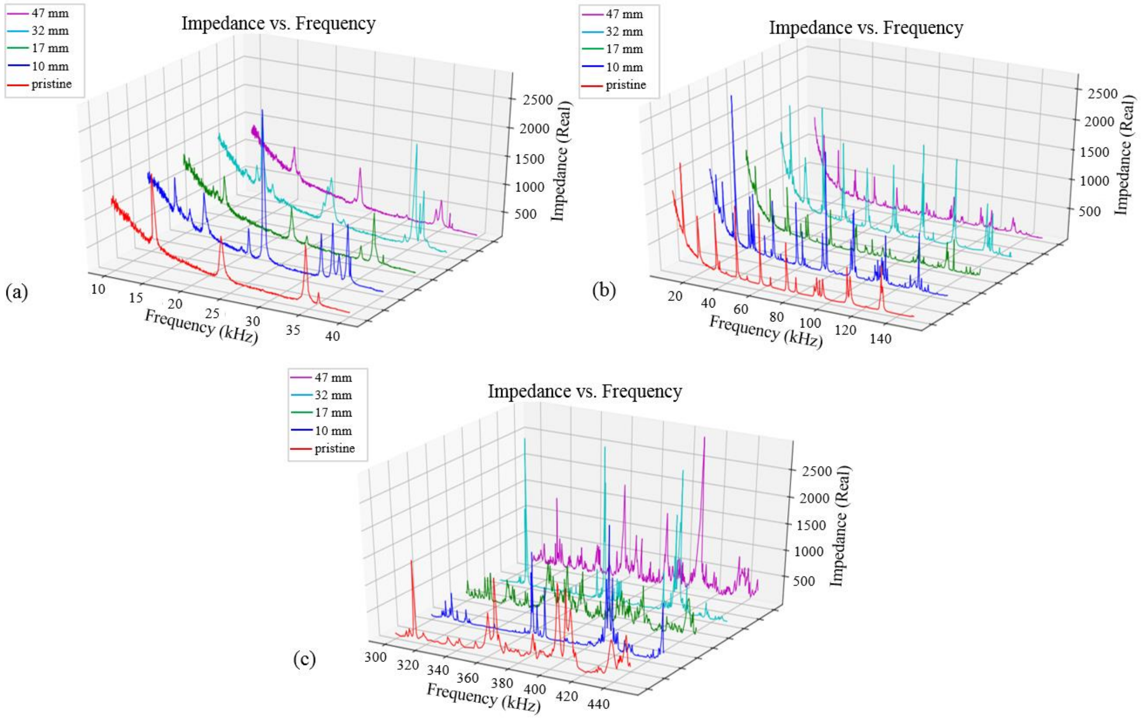

Figure 1.5 Plots of real impedance at (a) 10-40 kHz, (b) 10-150 kHz, and (c) 300-450 kHz.

Error analysis methods were then used on these three ranges to find a correlation between the different damaged specimen. The methods used were root mean square deviation (RMSD), mean absolute percentage deviation (MAPD), and correlation coefficient (CC), which were chosen based on previous research [8]. The equations associated with each of these methods are provided in equations (4), (5), and (6). When analyzing the values of each method, it is helpful to know what the numbers mean. For RMSD and MAPD a higher value represents larger deviation between the two data sets, while a lower value represents a better fit. The CC method has values between 1 and -1. A value close to 1 represents a strong positive correlation, a value close to -1 represents a strong negative correlation, and a value near zero represents a weak correlation. The statistical values for the previously stated frequency ranges are provided below in Table 1.1. In this table, the meaning of the values in the second row are as follows: *0* is the pristine specimen, *1* is 10 mm damage specimen, *2* is the 17 mm damage specimen, *3* is the 32 mm damage specimen, and *4* is the 47 mm damage specimen. The *0 - 1* is the correlation for the pristine and 10 mm damage specimens and so on.

Table 1.1 RMSD, MAPD, and CC values for the three frequency ranges

	10 - 40 kHz				**10 - 150 kHz**				**300 - 450 kHz**			
	0-1	*0-2*	*0-3*	*0-4*	*0-1*	*0-2*	*0-3*	*0-4*	*0-1*	*0-2*	*0-3*	*0-4*
RMSD	0.50	0.17	0.47	0.28	0.68	0.34	0.82	0.44	0.92	0.79	1.15	0.87
MAPD	0.35	0.10	0.38	0.13	0.64	0.36	1.21	0.40	0.92	1.43	1.37	1.34
CC	0.72	0.96	0.75	0.90	0.71	0.91	0.61	0.85	0.22	0.26	-0.02	0.40

Analyzing these values shows no clear correlation for any of the methods. When looking for a correlation between the statistical values and the distance to the damage, the values have no clear fit. The values fluctuate with no recognizable pattern. In attempt to find a better correlation, the same methods were used on a smaller frequency range. A lower frequency range of 22-27 kHz and a higher frequency range of 58-68 kHz were used (see Figure 1.6). The plots at these smaller ranges display a visual correlation. In each range the 10 mm specimen exhibits splitting of the resonances, the 32 mm specimen has multiple peaks, and the 17 mm and 47 mm are shifted to the right of the pristine peak. Although this is a clear visual trend, it is hard to quantify and does not lend itself to interpolation between the damages. The statistical values are provided in Table 1.2 and show the same lack of correlation as before. This method proves to be difficult and lacks solid correlations with resonance frequencies and damage location.

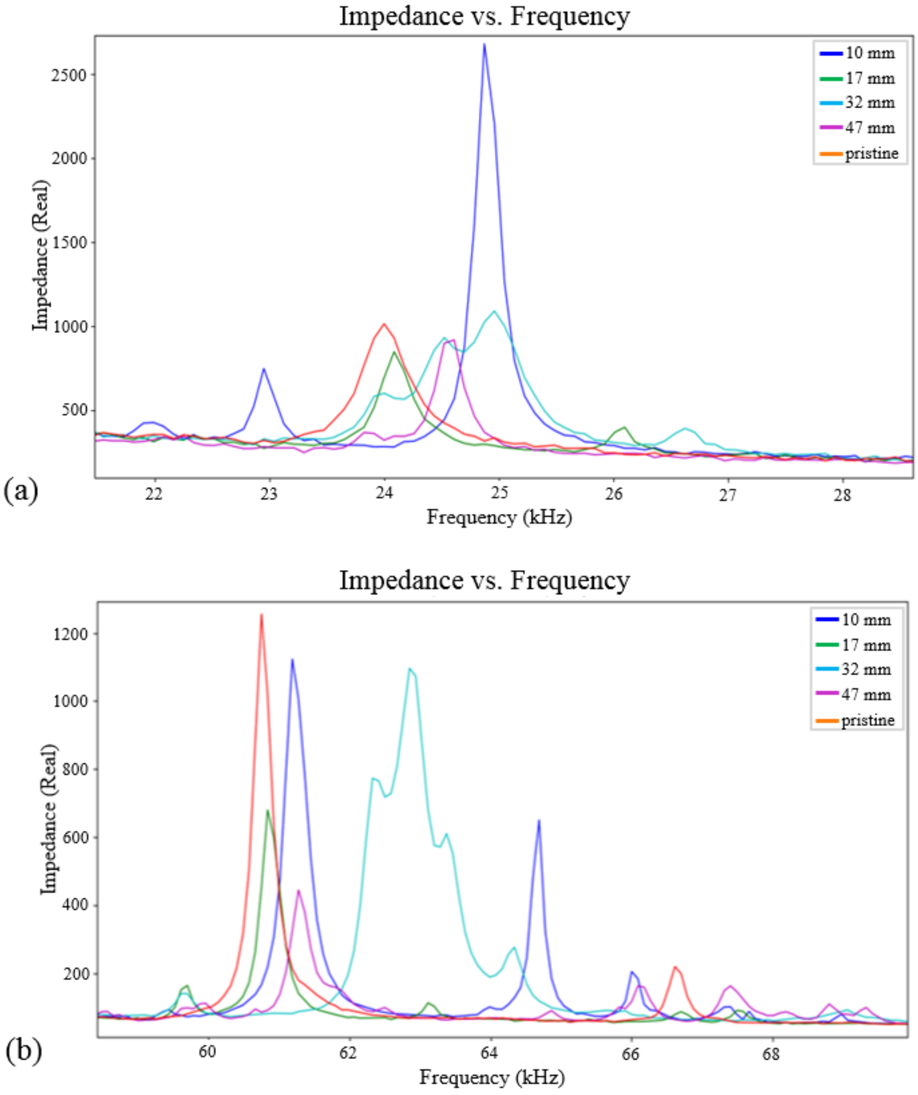

Figure 1.6 Plots of the real impedance at ranges of (a) 22-27 kHz, and (b) 58-68 kHz.

Table 1.2 RMSD, MAPD, and CC values for the smaller frequency ranges

	22 - 27 kHz				**58 - 68 kHz**			
	0-1	*0-2*	*0-3*	*0-4*	*0-1*	*0-2*	*0-3*	*0-4*
RMSD	1.21	0.25	0.65	0.49	1.06	0.52	1.50	0.85
MAPD	0.67	0.14	0.49	0.23	0.73	0.18	1.92	0.37
CC	-0.10	0.87	0.25	0.26	0.19	0.86	-0.14	0.10

1.5.5 Results for PWAS bonding quality experiment

The analysis for bonding quality consisted of comparing the slopes for each bonding condition to a fully bonded specimen and a free specimen. Before analyzing, the difference between the admittance of a free PWAS and bonded PWAS must be understood. Through prior research it is known that the bonding condition affects the imaginary part of the admittance, therefore this method was used [6]. Figure 1.7 shows the relationship by plotting the imaginary part of admittance versus frequency.

From the graph it’s clear that the bonding of a PWAS onto a structure causes a significant decrease in slope, with a difference of 66% for a fully bonded specimen. The slope then increases as the PWAS de-bonds due to the PWAS behaving more like a ‘free’ PWAS. To analyze the change the admittance was plotted at a large range to find the most consistent data. The range of consistent data was chosen to be 10-20 kHz, and a linear fit was used to find the slope. This process is represented in Figure 1.8.

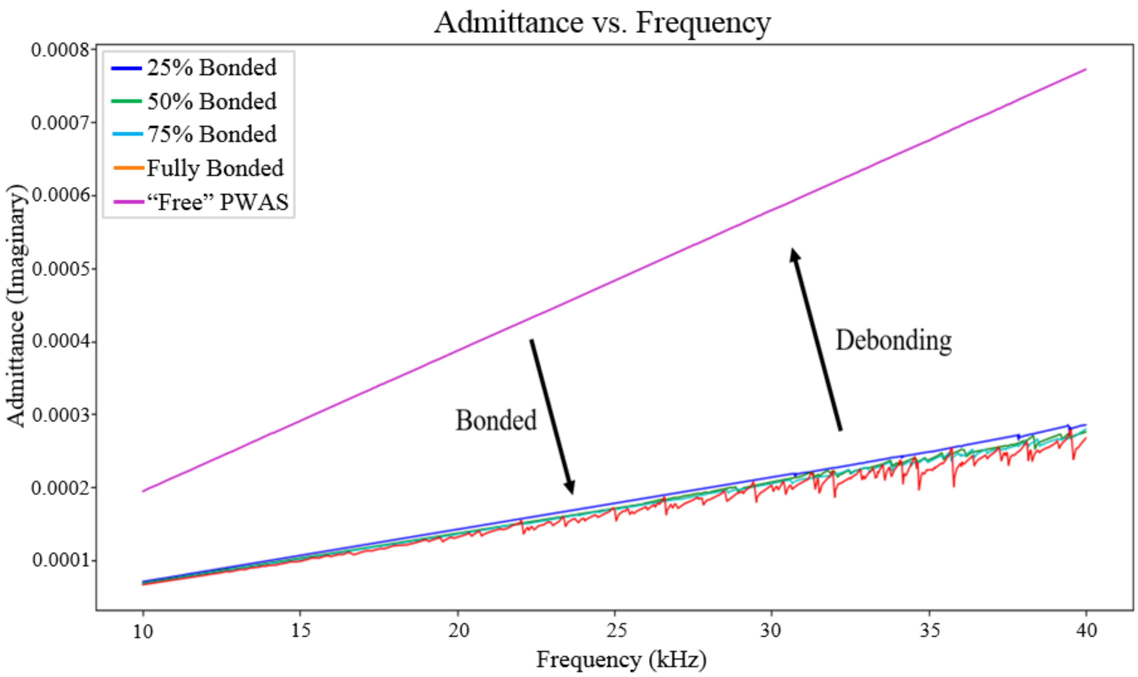

Figure 1.7 Comparison between free and bonded PWAS.

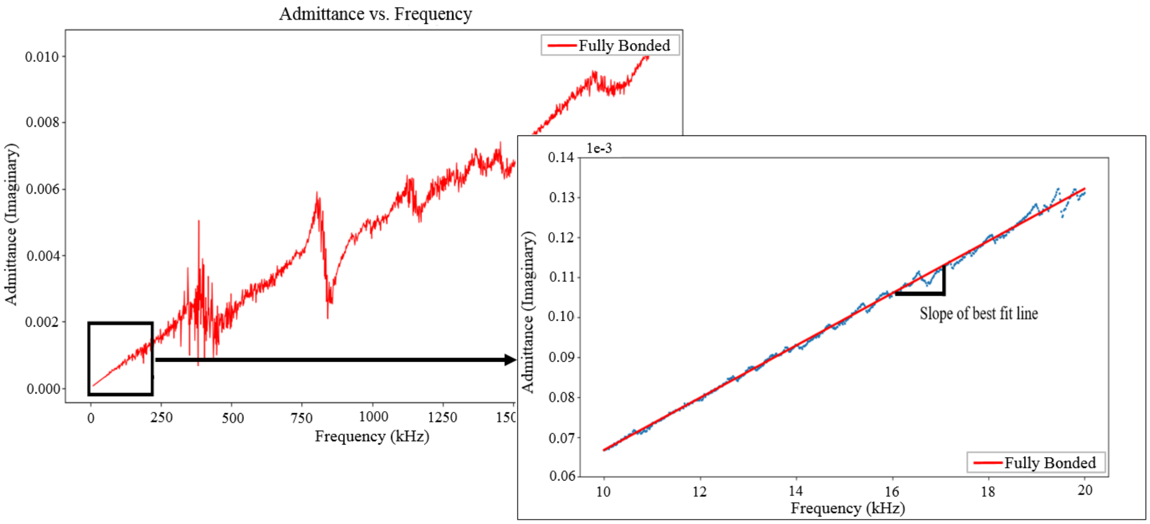

Figure 1.8 Representation of the method used to find a best fit line.

Using this process, the slope for each bonding condition was found. The slopes are plotted in Figure 1.9 and a clear linear trend between the slope and bonding condition is seen. As the debonding progresses, the slope of the imaginary admittance increases. From the figure, it is seen the points do not lie perfectly on the line. This is attributed to the difficulty of defining an exact bonding condition through the application of the adhesive. The linear fit can also be observed through comparing the bonded specimen slopes and the ‘free’ specimen slope (see Table 1.3). Similarly, the table shows the slope progressing toward the slope of the ‘free’ PWAS as the bonding level decreases. The method of comparing the imaginary admittances provides many similar ways of determining the linear fit, but these two are quick and easiest to observe.

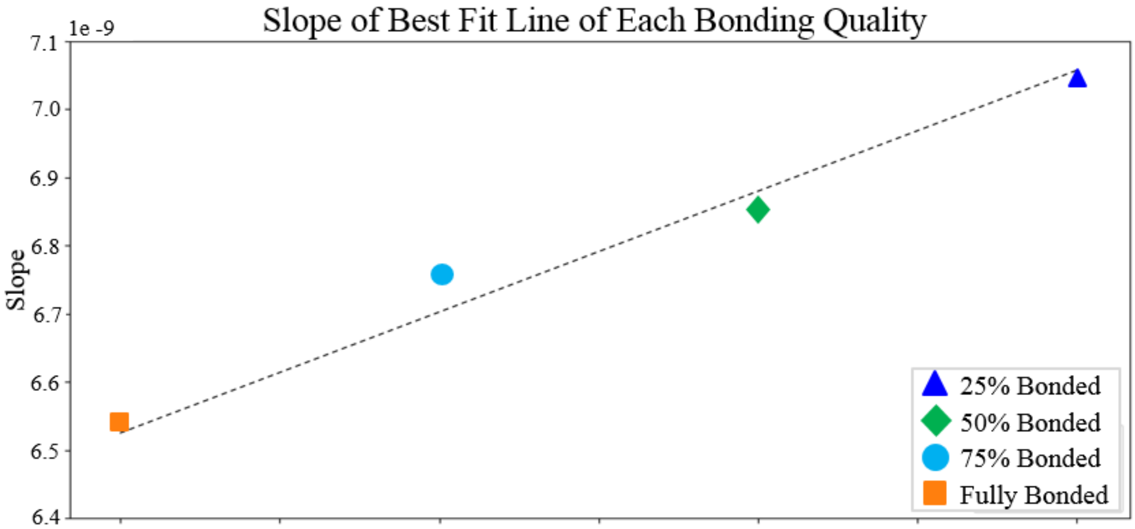

Figure 1.9 Plot of the slopes of the best fit line for each specimen.

Table 1.3 Percent difference of bonding condition slopes and free PWAS slopes

Bonding Condition	% Difference with Respect to Free PWAS
Fully Bonded	66%
75% Bonded	65%
50% Bonded	64%
25% Bonded	63%

1.6 SUMMARY AND CONCLUSIONS

The first experiment (damage detection) explored the difficulties in reading the real part of the impedance. There was a trend in visual resonance peaks for a specific damage location specimen, but it was hard to determine why that trend occurred when comparing it to other damage location responses. This concludes that the real part of the impedance does change with structure damage locations, but further work and evaluation must be done to determine the trend. The second experiment (bond quality) gave a better trend that allows us to get more information on the bonding of the PWAS. The imaginary part of the admittance provides the quality of the bonding of the PWAS to its host structure. Comparing a perfectly bonded PWAS to a ‘free’ PWAS, the slope of the fully bonded PWAS is 66% of the free PWAS. As the PWAS becomes unbonded, the slope slowly increases. In future work, it might be helpful to compare these results to results with a controlled environmental effect. PWAS may be used for aerospace purposes, which means temperature, humidity and pressure will change and could affect the reading of the electrical response.

CHAPTER 2

LOW CYCLE FATIGUE CRACK EXPERIMENT TO CAPTURE AE SIGNALS

2.1 INTRODUCTION

Aerospace structures, including aircrafts and ships, are mainly constructed with an aluminum body. Due to the mechanical and environmental properties, these aerospace structures experience consistent vibration. The vibrations can cause microscopic cracks in high stress areas in the structure and have been known to lead to catastrophic failure. The aerospace structure can be evaluated between flights, but that takes a lot of time and money. The goal is to develop a way to evaluate the health of the material at equal time intervals whether the structure is in flight or not. This method of evaluation is called structural health monitoring.

Structural health monitoring (SHM) and non-destructive evaluation (NDE) are damage detection strategies that allow one to determine the health of a material and to predict its lifespan [10], [11]. Together, SHM and NDE have been proven to be effective in detecting fatigue cracks in a structure. Specifically, the study of acoustic emission (AE) is a well-established and reliable method used in SHM and NDE to detect damage. AE has a wide range of applications including being used to detect the loosened/tightened state of a bolted structure [12] or to detect delamination or impact localization in composite plates [13], [14]. There is also a vast practice of using AE to detect fatigue cracks. Acoustic emission is used to detect fatigue cracks in materials including T-section girders and welded steel for bridges [15], transverse weld toe for bridges [16], and wind turbine blades [17]. AE is also used to evaluate fatigue cracks in thin aerospace structures including aircrafts [18]. Applying fatigue loading to an aircraft material (aluminum 2024) to study signatures in acoustic emission waveforms due to a fatigue crack was also studied [1], [19].

Once a set of AE data is collected, the data must be processed and analyzed to interpret its significance. There are many methods that are used to analyze data, which include signal enhancement, signal separation, source location, source characterization, etc. [20]. Many researchers use the fast Fourier transform (FFT) to analyze signals based on their frequency spectrum [21]. Joseph et al. [22] used the Pearson Correlation Coefficient (PCC) to study how similar two waveforms can be to one another based on their time and frequency domains. Many researchers have used Lamb wave propagation as well as signal time of arrival for source localization [23], [24].

There are some common problems in the study of acoustic emission signals. An AE signal can be produced not only from the damage in question but also from outside sources, including environmental noise. The AE from outside sources is a contributor to the large amount of data typically collected during AE testing [2], [3]. Another issue when sensing AE is based on the sensitivity the sensor has due to bonding quality/technique and wire soldering of the sensor. The mitigation of these issues is described later in the chapter. Section 2.2 describes the state of the art procedure and results of an LCF experiment performed by Bhuiyan [19]. The rest of the chapter describes the procedure and results of an LCF experiment performed and compares the results to the results from section 2.2.

2.2 STATE OF THE ART FEATURE EXTRACTION FOR ALUMINUM 2024

An important factor in research is the repeatability of an experiment. Waveforms due to acoustic emission signals can look different based on many factors. Some of those factors include the types of sensors being used or the size and shape and material of the specimen or the acoustic emission source including damage, environmental factors, etc. With many different possibilities of waveform signatures, it is important to determine a level of confidence in the types/source of signatures observed for a type of damage. It is also important to understand how various parameters can affect these waveforms such as the frequency of loading in a fatigue crack. When there is fatigue on a specimen with a crack in it, the crack will open and close and the idea is to be able to determine whether the crack is open, closed or somewhere in the middle.

An overview of the hit signature and waveform signature analysis done for a cyclically loaded specimen with a crack from reference [19] is explained in this section. Various features are examined in this chapter, including the appearance of the time domain waveform, frequency peaks and the load at which the waveform occurs.

2.2.1 Experimental set-up and procedure for fatigue loading

The specimen used is a 304 mm length, 100 mm width and 1 mm thick aircraft grade aluminum Al-2024 T3. The specimen was placed in an MTS machine which axially and cyclically loaded the specimen between 2.3 kN and 23 kN with a frequency of 4 Hz. These loads are 6.5% and 65% of the tensile yield strength (345 MPa) of the material. After initiating the crack and growing it to 20 mm, the specimen was removed from the MTS machine and the proper AE sensing instrumentation was employed. The AE sensing instrumentation included a PWAS sensor that was glued to the specimen 5 mm from the crack using M-Bond 200. To reduce the amount of reflective AE waves, a non-reflective boundary (NRB) made of clay was applied to the specimen. In addition, a strain gage was attached to the specimen to simultaneously capture the load to help analyze and group the hits. A schematic of the specimen with all the proper instrumentation attached is seen in Figure 2.1. Once the proper instrumentation was installed, the specimen was placed back in the MTS machine. This time, to monitor the crack growth, the load and frequency of the axial loading was reduced. The load was varied sinusoidally between 1.23 kN and 12.3 kN at a frequency of 0.05 Hz, which is a low cycle fatigue (LCF) experiment. With the help of a bandpass filter (filters out signals between 30 kHz to 700 kHz) and MISTRAS AE instrumentation, AE hits were captured.

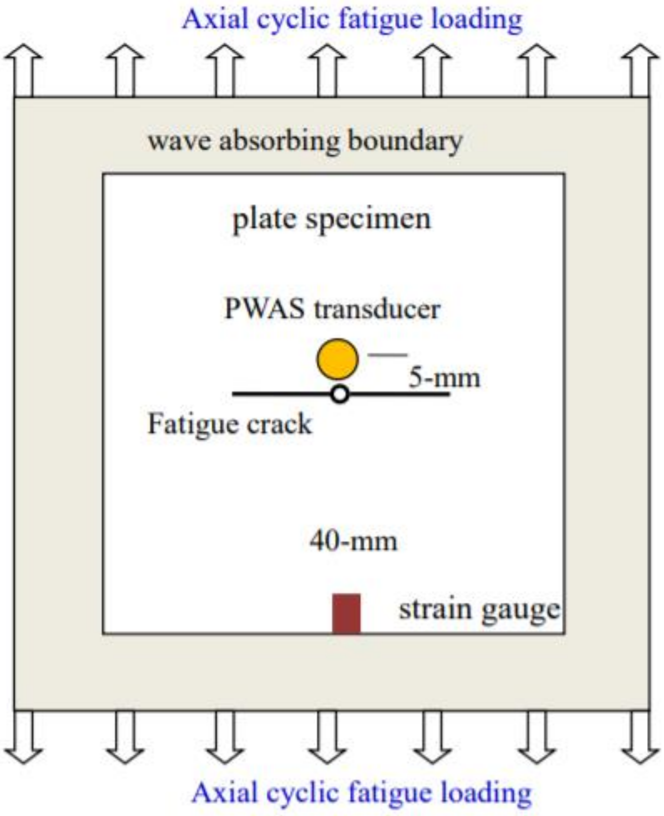

Figure 2.1 Diagram of fatigue specimen with a PWAS 5 mm from the crack. [19]

2.2.2 *Experimental results*

Based on the information provided by the MISTRAS AE instrumentation, the captured time and frequency domain of all the waveforms can be plotted with the sinusoidal loading. Once all the hits were placed on a loading graph, the hits were assigned to eight different groups (A-H) based on the major frequency peaks and at the load the hit occurred. Based on these factors, the grouped hits can be hypothesized to originate from either crack growth or crack rubbing and clapping. A hit plot of 50 cycles and the load pattern is found in Figure 2.2. In the figure, the hits are color coded based on their respective groups.

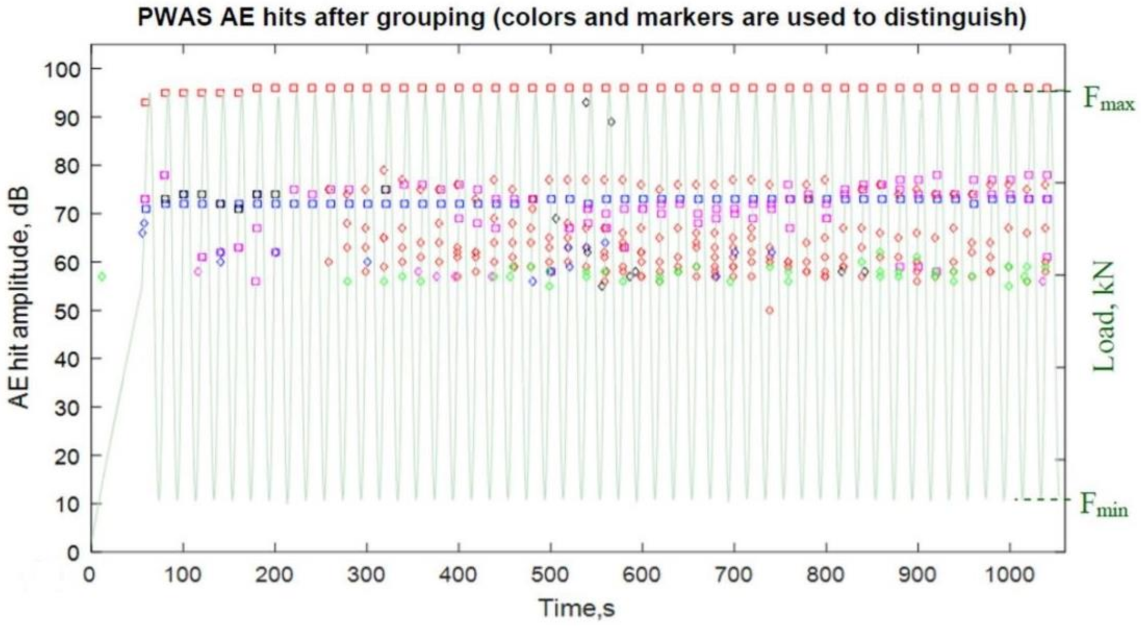

Figure 2.2 AE hits captured by the PWAS with simultaneous load readings. [19]

The hits during these 50 cycles were grouped into eight different groups based on the time and frequency domain of the waveform. Group A included waveforms that had the same time and frequency domain and occurred almost consistently at 72 dB. Group A hits happened at approximately 84% of the maximum fatigue load. To understand the percentage of the maximum load at which the hit occurred can be described by Figure 2.3. Its major frequency content occurs at ~40 kHz, ~100 kHz, and ~350 kHz. Group B waveforms all occurred at a higher amplitude of 96 dB and occurred at 78% of the maximum load. Its major frequency content occurs at ~60 kHz, ~100 kHz, and ~230 kHz and then a drop at ~450 kHz. The hit plot as well as waveforms for group A and B can be found in Figure 2.4.

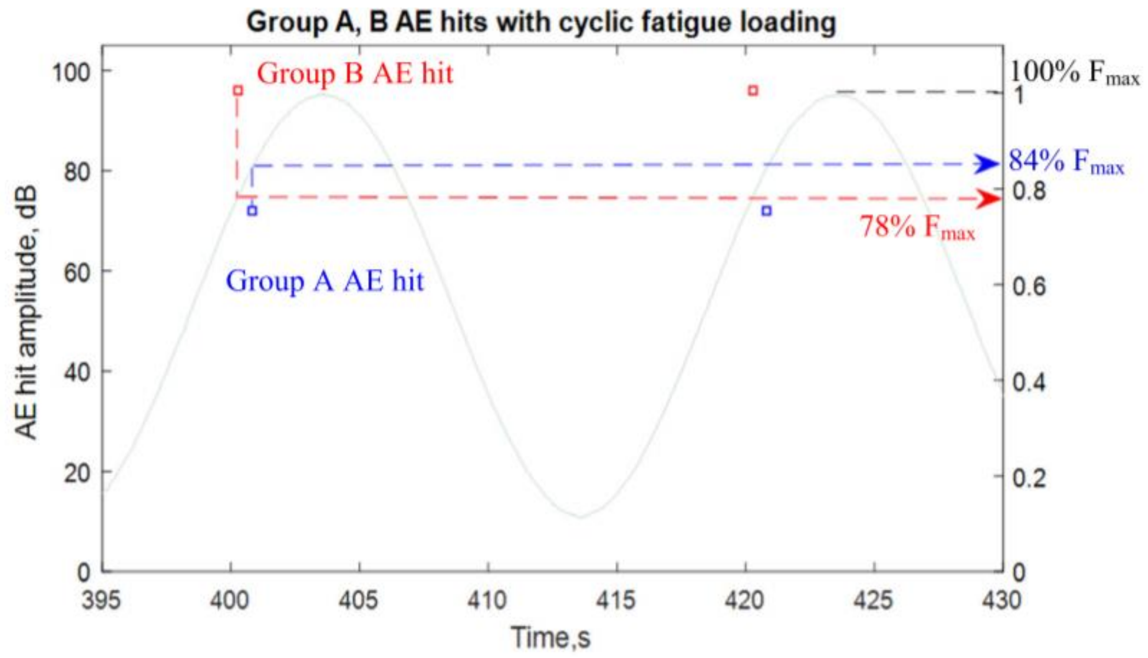

Figure 2.3 Description of load level at which group A and group B occurred at. [19]

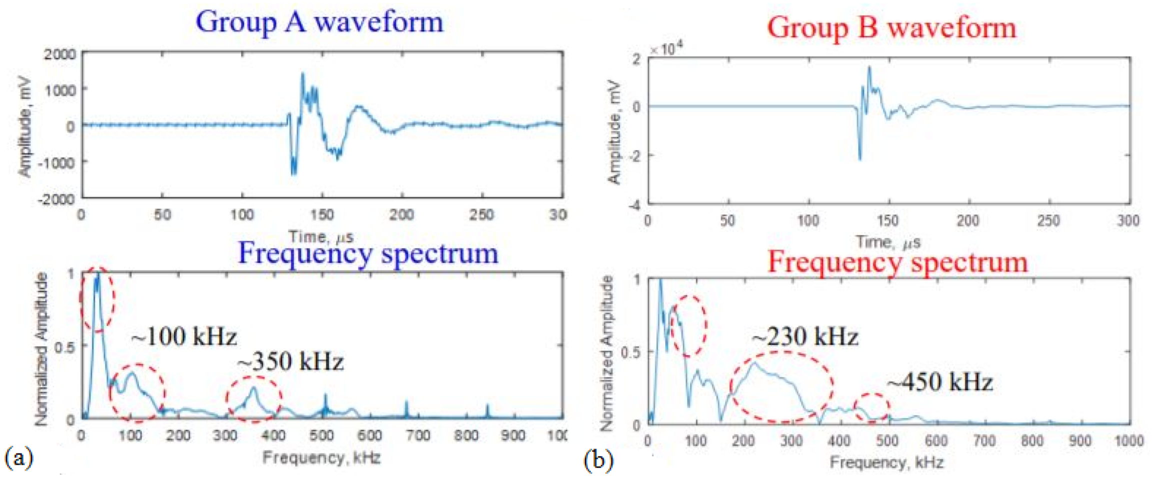

Figure 2.4 (a) Time and frequency domain of a typical group A waveform, (b) time and frequency domain of a typical group B waveform. [19]

Group C did not consistently occur at the same amplitude and averaged at ~81% of the fatigue loading. Group C had high frequency content at ~30 kHz and ~100 kHz and a typical group C waveform can be seen in Figure 2.5. Group D was a relatively small group that occurred at 78% of the maximum load and were present only in the first 300 s of cyclic loading. Group D had high frequency content at low frequencies and then again at ~230 kHz, ~450 kHz and ~550 kHz. Group D hit plot and typical waveform can be seen in Figure 2.6.

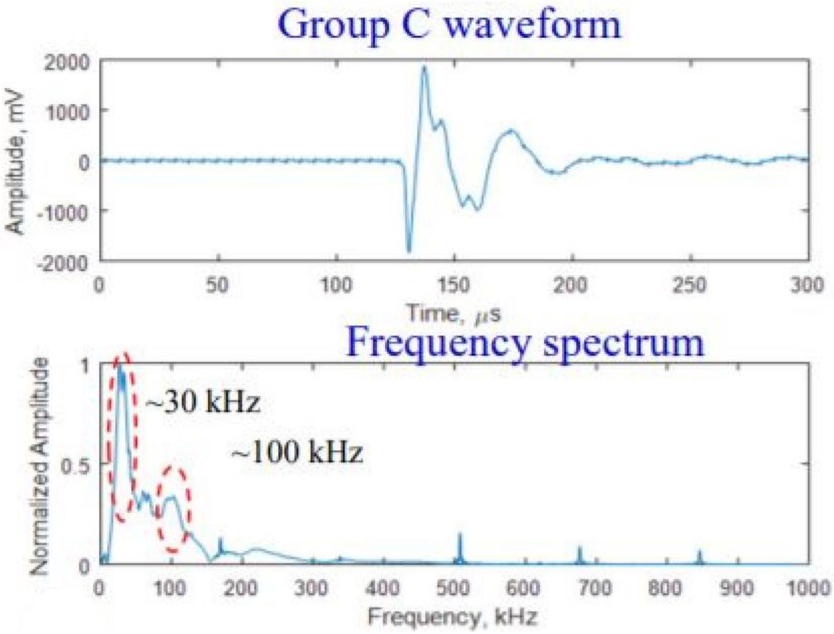

Figure 2.5 Time and frequency domain for group C. [19]

Group E hits happened as a cluster with about two or three hits for every loading cycle. The first hit in the cycle always had the highest amplitude compared to the second and third hits. These hits varied between 51% and 58% of the maximum load and appeared after ~250 s into the cyclic loading. A typical waveform for group E is shown in Figure 2.7. In the Figure 2.7, you can see that the dominant frequency peaks occur at ~30 kHz, 60 kHz and 200 kHz.

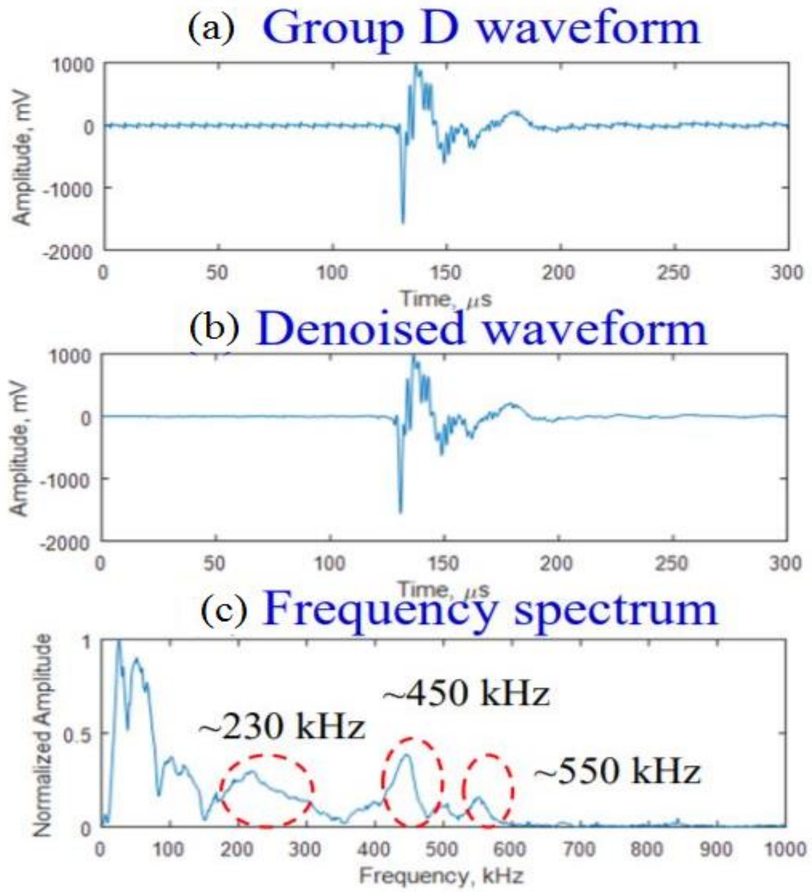

Figure 2.6 (a) Actual group D waveform, (b) denoised group D waveform, (c) frequency domain for group D. [19]

Group F hits occurred at about 57% of the maximum load and occurred in every cycle and happened at similar times as group E hits. Group F hits had a similar frequency spectrum as group E, but group F had an additional frequency peak at 450 kHz. A typical Group F waveform can be seen in Figure 2.8. Group G hits occurred between 78% and 81% of the maximum load and the hits occurred sporadically throughout the 50 cycles. Group G frequency spectrum is very similar to Group C except it doesn’t have some of the low frequency peaks including 40 kHz. A typical Group G waveform can be seen in Figure 2.9.

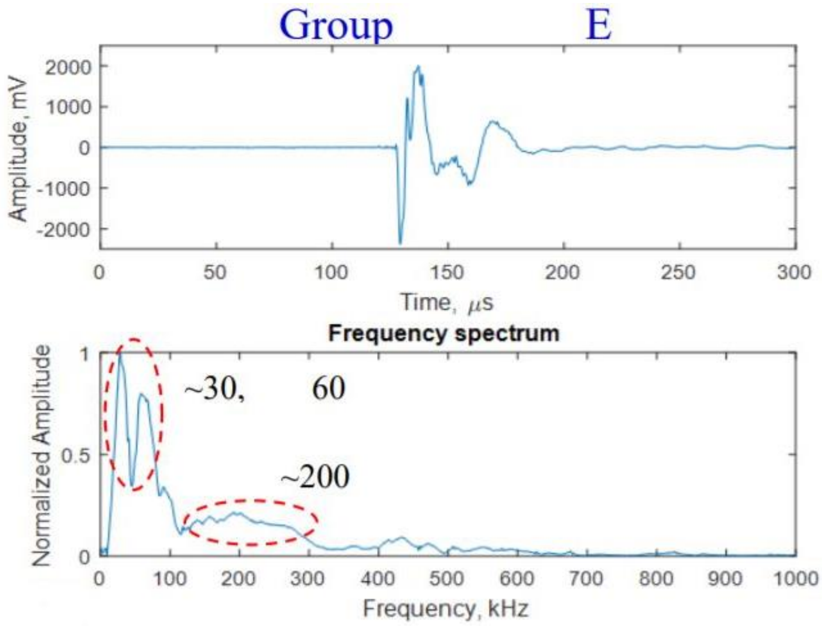

Figure 2.7 Time and frequency domain for group E. [19]

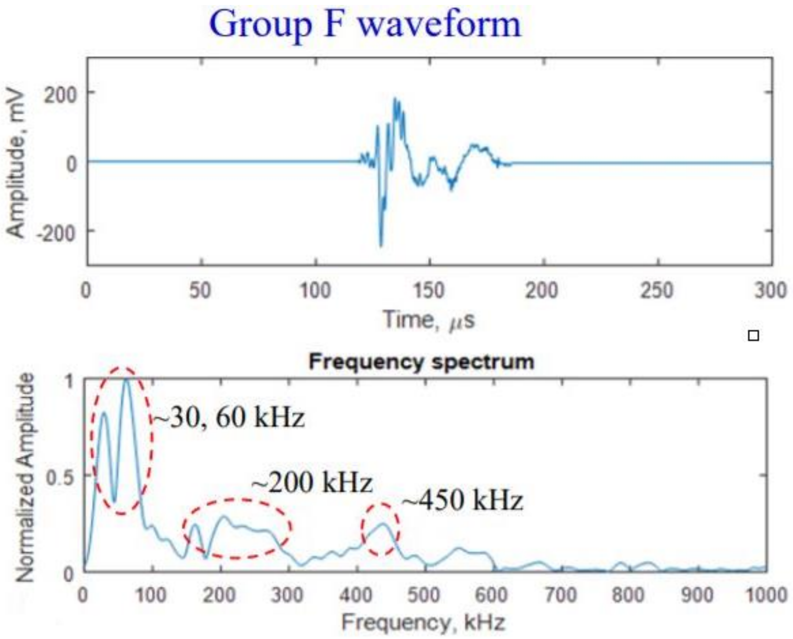

Figure 2.8 Time and frequency domain for group F. [19]

Group H was grouped because it only reached about 23% of the maximum load. These hits occurred the least in the 50 cycles and had major frequency peaks at ~40 kHz, ~70 kHz, ~100 kHz, and ~200 kHz. A typical Group H waveform can be found in Figure 2.10.

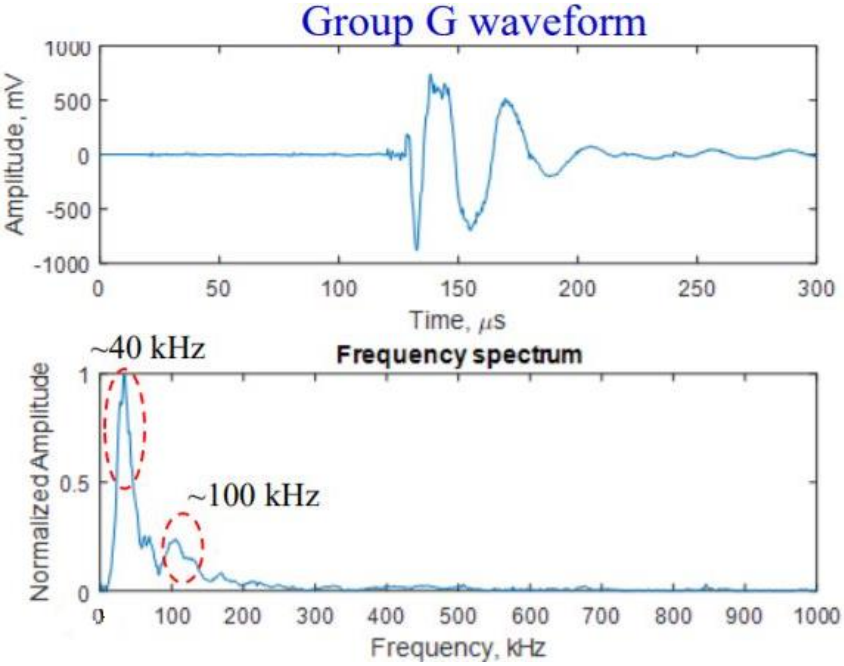

Figure 2.9 Time and frequency domain for group G. [19]

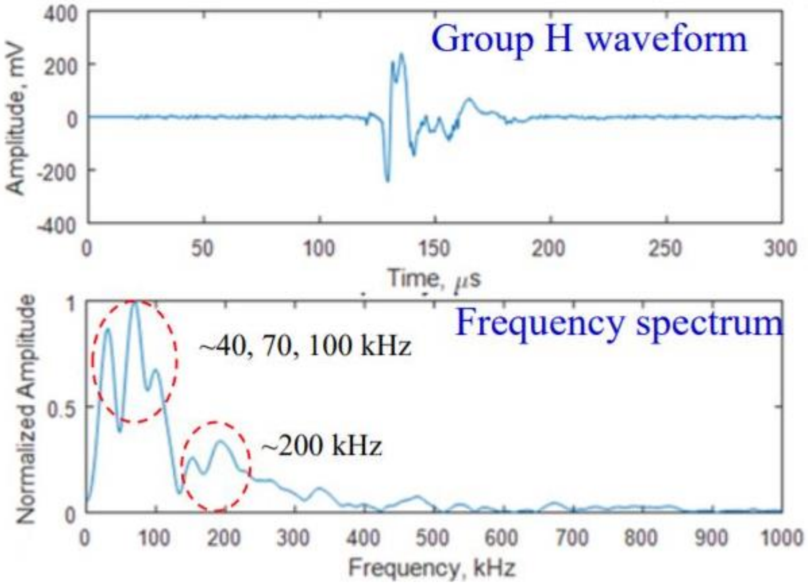

Figure 2.10 Time and frequency domain for group H. [19]

2.3 EXPERIMENTAL SET-UP

An Aluminum 2024-T3 specimen that is 304 mm long, 101 mm wide and 1 mm thick is used to simulate an aluminum plate that would be used in an aircraft. A 1 mm hole is drilled into the center of the specimen to ensure the crack will grow in the center. Prior to placing the specimen in the cyclic loading MTS machine, the machine was zeroed. The specimen was then placed into the MTS machine with 2 inches of the specimen being gripped on either side. The MTS machine being used has two different load cells. One load cell is 50,000 lbf and the other is 5,000 lbf. Since the testing load does not exceed 4,945 lbf, the 5,000 lbf load cell was chosen for more accuracy. A sinusoidal load of 2.2 kN to 22 kN ($R= \sigma_{min}/\sigma_{max} =0.1$) was applied to the specimen to grow the crack to ~21 mm. These values were chosen because they are 6.5% and 65% of the tensile yield strength of the specimen which are the load levels typically used in practical aircraft testing. The fatigue crack was initiated after about 35,000 cycles and it took 4,571 cycles to grow the crack to ~21 mm. The growth of the crack was tracked with the use of ruler tape applied directly on the specimen.

After the crack was grown to 20 mm, the specimen was removed from the MTS machine. A non-reflective boundary (NRB) made of clay was applied to the specimen to eliminate the reflective AE waves that may occur. The sensors used to detect the acoustic emissions are two piezoelectric wafer active sensors (PWAS) and two S9225 sensors. On side 1 of the specimen, the two PWAS were bonded to the specimen using M-Bond AE-15 at 5 mm and 25 mm away from the crack. The two S9225 sensors were bonded on the other side of the crack mirroring the first two sensors. The S9225 sensors were bonded to the specimen using hot glue from a hot glue gun. On side 2 of the specimen, a strain gage was bonded to the specimen using M-Bond AE-15 at 35 mm from the crack. The layout of the specimen can be seen in Figure 2.11.

Once all the clay boundaries and sensors were applied to the specimen, the MTS machine was zeroed, the load cell was chosen to be 5,000 lbf, and the specimen was placed back into the MTS machine and some baseline procedures were conducted. When the specimen is first placed into the machine, the machine fluctuates between compression and tension. The load was set to 100 lbf to reduce fluctuation and have consistency for pre-testing measurements. The pre-testing measurements include setting a threshold, pencil lead break (PLB), impedance test, eddy current measurement, and pictures of the crack and crack tips. The threshold of the AEwin software was set right above the environmental noise level and then raised 2 dB to ensure the environmental noise won’t be detected during testing. A pencil lead break (PLB) was done to ensure all sensors were working properly based on time of arrival and amplitude of the hits. Generally, the PWAS recorded a higher amplitude than the S9225 sensors. PWAS recorded a higher amplitude than S9225 sensors because PWAS are sensitive to both in-plane and out-of-plane motion whereas S2995 sensors are only sensitive to out of plane motion. An eddy current measurement was taken to determine the length of the crack prior to any testing. An impedance test was also conducted using an Impedance Analyzer and Bode Analyzer Suite software to get a baseline of the bonding of the two PWAS. Lastly, a camera was used to take a picture of the crack and crack tips prior to any testing. A picture of the experimental set up can be seen in Figure 2.12 and a picture of the specimen can be seen in Figure 2.13. After all these baseline measurements were conducted, the fatigue experiment can be conducted.

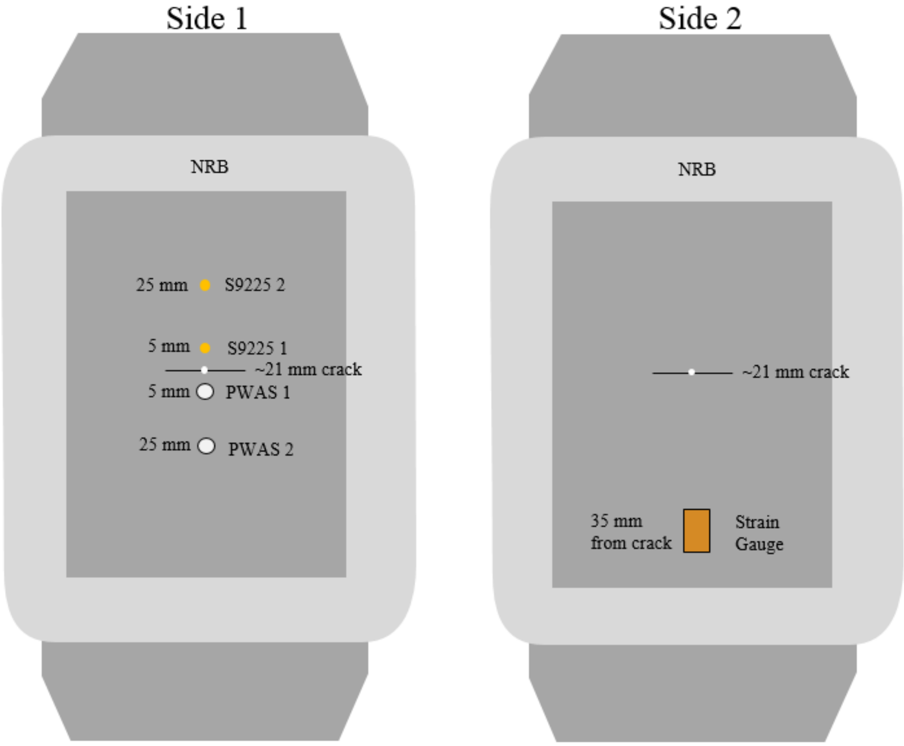

Figure 2.11 Side 1 and side 2 of specimen with applied NRB and sensors.

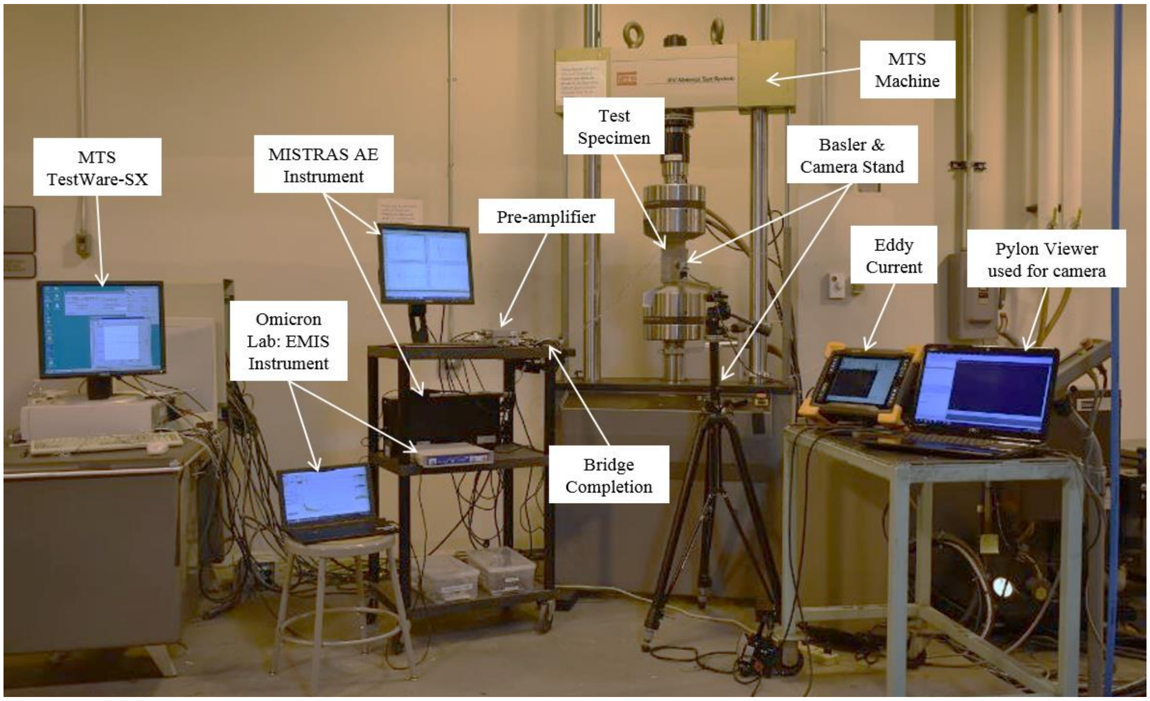

Figure 2.12 Experimental set-up of all devices used to help monitor and conduct the LCF experiment.

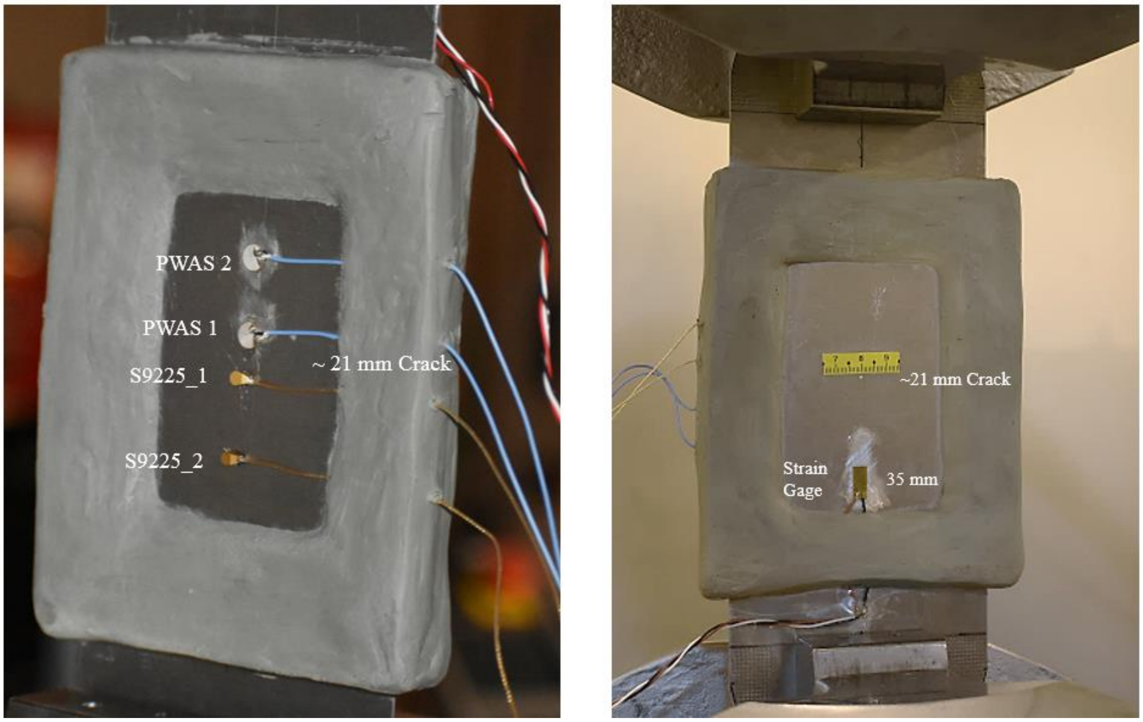

Figure 2.13 Picture of specimen loaded in the MTS machine prior to testing.

2.4 EXPERIMENTAL PROCEDURE FOR LCF CRACK GROWTH

A lower sinusoidal load of 1.23 kN to 12.3 kN was applied at a low frequency to control the growth of the crack. The frequencies ranged from 0.05 Hz to 2 Hz. The crack was monitored using AEwin which provided a time and frequency domain for all the AE events. The strain gage gave a sinusoidal strain reading which was later converted into a normalized load which allowed for the recording of the load at which the AE event occurred. Although the load could be measured directly from the load cell, we decided that we wanted synchronized loading values with the hits that occurred on AEwin. The camera was used to video the crack throughout the low cycle fatigue (LCF) crack growth. Periodically, the loading on the specimen was stopped at maximum load and an Eddy Current, Impedance measurement, and picture of the crack was conducted to monitor the length of the crack and to ensure the bonding of the PWAS had not changed. This methodology is detailed out in Figure 2.14.

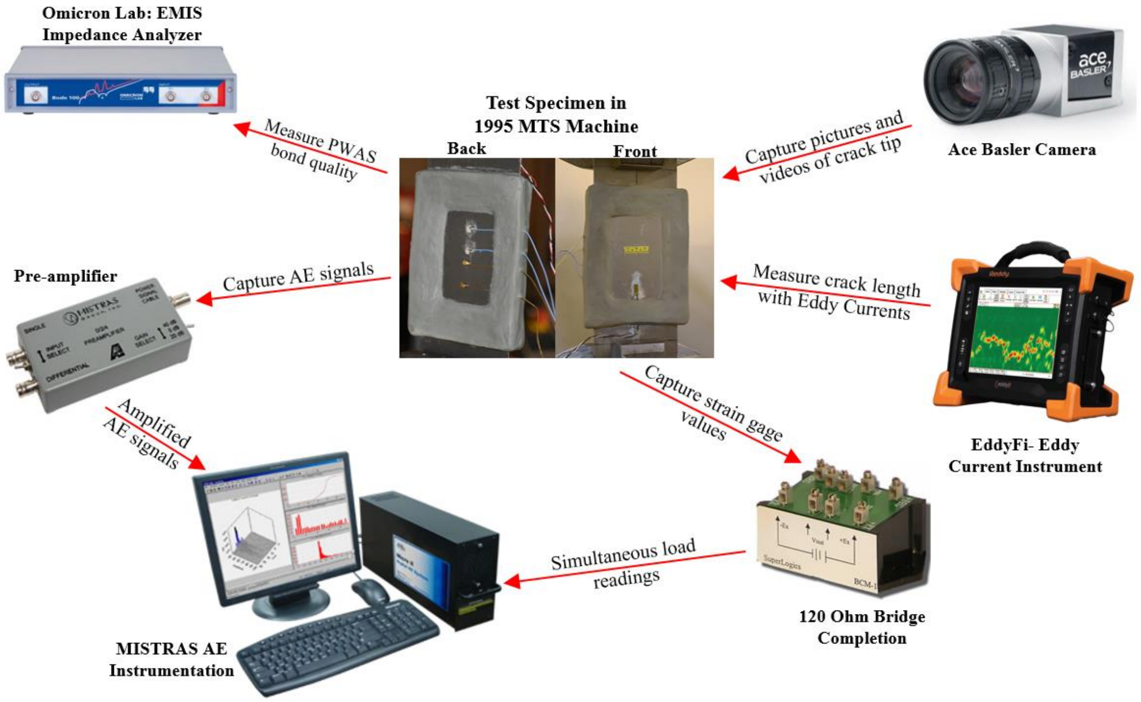

Figure 2.14 Detailed methodology of machinery and instrumentation used in LCF experiment.

2.5 EXPERIMENTAL RESULTS

The crack was grown from ~21 to ~23 mm in 5,320 cycles and eddy current measurements were taken periodically throughout the experiment. A table of crack initiation data and a table showing data from crack growth cycles can be seen in Figure 2.15. An example of eddy current measurements taken at ~21 mm, ~22.5 mm and ~23 mm can be seen in Figure 2.16. Through visualization of the crack length with the use of ruler tape, it was observed that the red area in Figure 2.16 representes the visual crack length while the yellow and green indicated internal fracture that cannot be seen with the human eye. The jagged lines along the length of the crack prove that the crack faces are not perfectly smooth. The results in this section include the waveforms and discussion from 60 cycles at 0.5 Hz, 0.25 Hz, 0.1 Hz and 0.07 Hz. Results from various frequency loadings are introduced as a way to determine if frequency of loading can change the signature of an AE signal. Based on obervation of the crack through a camera and an eddy current, the crack did not grow during any of the cycles being reviewed in this section; all AE hits are from crack rubbing and clapping. For each set of 60 cycles, the normalized hit amplitudes from all four sensors as well as the normalized sinusoidal load recorded from the strain gage were plotted onto one graph. A further analysis of the waveforms for 10 of the 60 cycles was conducted. The waveforms were then subjectively separated into two different groups based on frequency peaks.

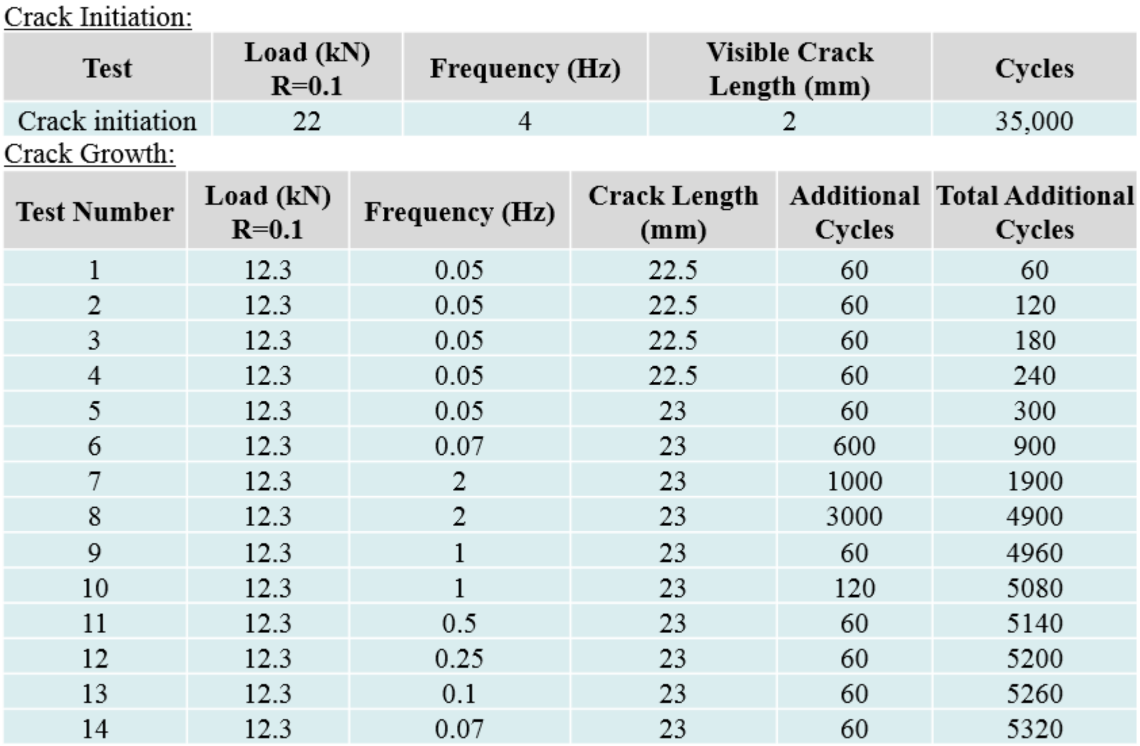

Crack Initiation:

Test	Load (kN) R=0.1	Frequency (Hz)	Visible Crack Length (mm)	Cycles
Crack initiation	22	4	2	35,000

Crack Growth:

Test Number	Load (kN) R=0.1	Frequency (Hz)	Crack Length (mm)	Additional Cycles	Total Additional Cycles
1	12.3	0.05	22.5	60	60
2	12.3	0.05	22.5	60	120
3	12.3	0.05	22.5	60	180
4	12.3	0.05	22.5	60	240
5	12.3	0.05	23	60	300
6	12.3	0.07	23	600	900
7	12.3	2	23	1000	1900
8	12.3	2	23	3000	4900
9	12.3	1	23	60	4960
10	12.3	1	23	120	5080
11	12.3	0.5	23	60	5140
12	12.3	0.25	23	60	5200
13	12.3	0.1	23	60	5260
14	12.3	0.07	23	60	5320

Figure 2.15 Crack initiation and crack growth data tables

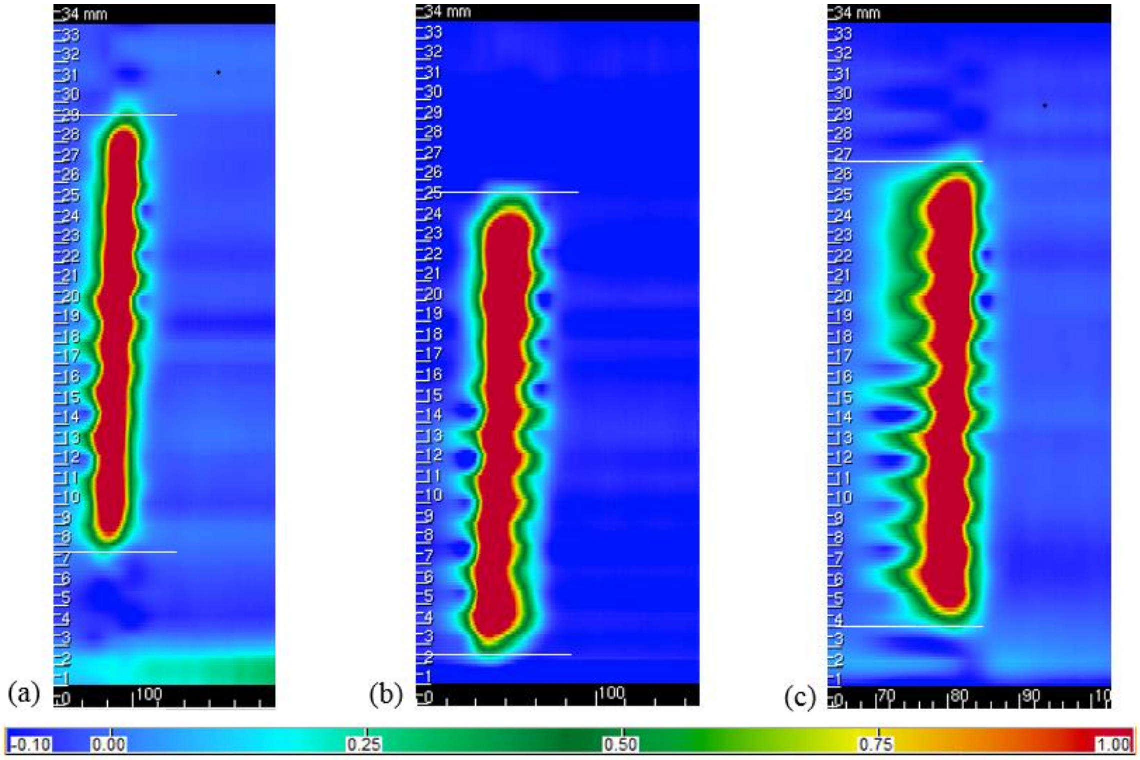

Figure 2.16 Eddy current measurements at (a) ~21 mm, (b) ~22.5 mm, and (c) ~23 mm.

2.5.3 Waveform groups for 60 cycles at 0.5 Hz

With the test specimen in the MTS machine, it was loaded to 12.3 kN (2765 lbf) with R=0.1 and a frequency of 0.5 Hz. The specimen was sinusoidally loaded for 60 cycles and data was collected from PWAS 1, PWAS 2, S9225 1, and S9225 2. As AE data was being collected, the strain gage measured the strain simultaneously which was then converted and normalized to force in lbf. A plot of the sensor hits and loading for 60 cycles at 0.5 Hz can be seen in Figure 2.17. In the figure, you can see that the sensors did not detect any AE signals at some loading cycles. After reviewing the results of the signals, there were two AE signal signatures observed at three different loads and amplitudes. Based on subjective signal types, the signals were clustered into two different groups. A plot of just 10 of the 60 total cycles, which show both groups (as seen in yellow), can be seen in Figure 2.18. All signals were captured during the loading of the specimen and none during unloading. This indicates that uneven surfaces on opposite faces of the crack only came in contact during loading. Typically, the signals were captured at about 87% of the load which is 10.701 kN (2405.55 lbf). There were some hits that were recorded at about 42% of the maximum load which is 5.166 kN (1161.3 lbf). It is important to note that sensor S9225 2 does not function properly and records slightly lower recorded amplitudes.

Figure 2.17 Sensor hits and loading for 60 cycles with loading frequency of 0.5 Hz.

Typical group 1 AE waveforms had high amplitudes and were captured by all four sensors and can be seen in Figure 2.19. These signals typically occurred at about 87% of the maximum load and had maximum low frequency content and additional peaks at ~150 Hz, ~275 Hz, and ~375 Hz. Occasionally, there were low amplitude group 1 signals that occurred at 87% of the maximum load as seen by the corresponding hits at 81.34 s and the signals were only captured by near field sensors. On other occasions, group 1 signals had low amplitudes and occurred at only 42% of the maximum load. No matter the load or amplitude, group 1 signal signatures were similar. Group 2 signals can be seen in Figure 2.20. These signals also occurred at 87% of the maximum load and had a lower amplitude than group 1 hits. Group 2 frequency domain waveforms consisted of only low frequency content and a small frequency peak at ~150 Hz.

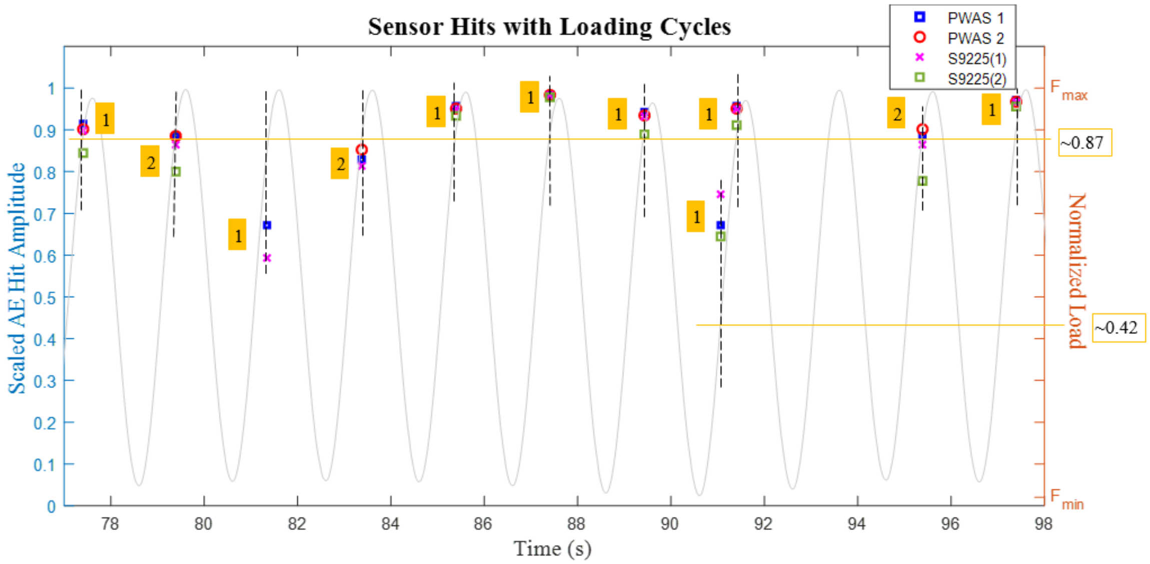

Figure 2.18 Sensor hits and loading for 10 cycles with loading frequency of 0.5 Hz assigned to groups 1 or 2.

2.5.4 Waveform groups for 60 cycles at 0.25 Hz

The results in this sub-section are for a sinusoidally loaded specimen with a loading frequency of 0.25 Hz. The maximum load applied was 12.3 kN (2765 lbf), R=0.1 for 60 cycles. A plot of the load and AE signals from all four sensors can be seen in Figure 2.21. After reviewing the results, a section of 10 cycles was focused on where two AE signal signatures appeared. This plot along with the group numbers (as seen in red) can be seen in Figure 2.22. All signals were captured during the loading of the specimen and none during unloading. The signal signatures are similar to the signatures of group 1 and 2 with a loading frequency of 0.5 Hz (section 2.5.3) except they appeared at different loads and amplitudes. The two loads discovered were at 89% of the maximum load which was 10.947 kN (2460.85 lbf) and at 77% of the maximum load which is at 9.471 kN (2129.05 lbf). Group 1 only appeared at 89% of the maximum load while group 2 appeared at both loads.

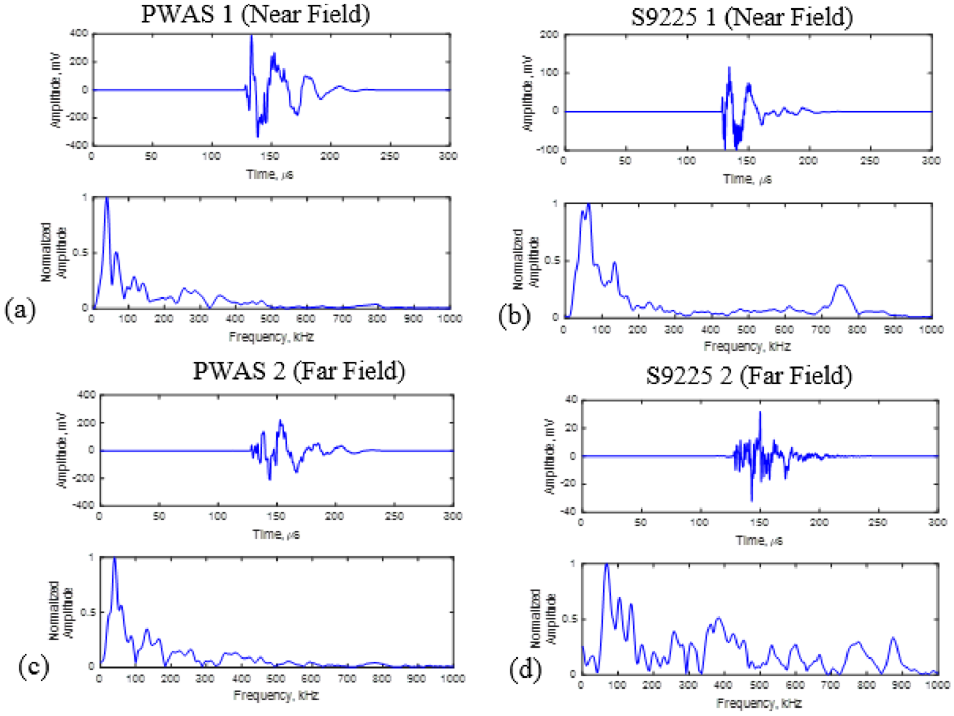
PWAS 1 (Near Field)

S9225 1 (Near Field)

PWAS 2 (Far Field)

S9225 2 (Far Field)

Figure 2.19 Group 1 waveform for (a) near field PWAS 1, (b) near field S9225 1, (c) far field PWAS 2, and (d) far field S9225 2 with loading frequency of 0.5 Hz.

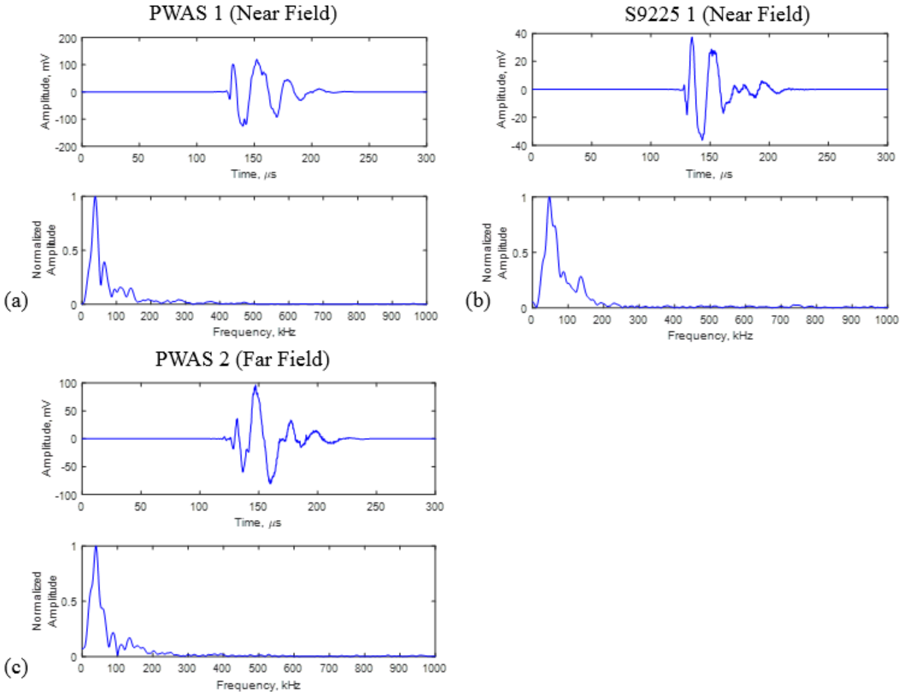
PWAS 1 (Near Field)

S9225 1 (Near Field)

PWAS 2 (Far Field)

Figure 2.20 Group 2 waveform for (a) near field PWAS 1, (b) near field S9225 1, and (c) far field PWAS 2 with loading frequency of 0.5 Hz.

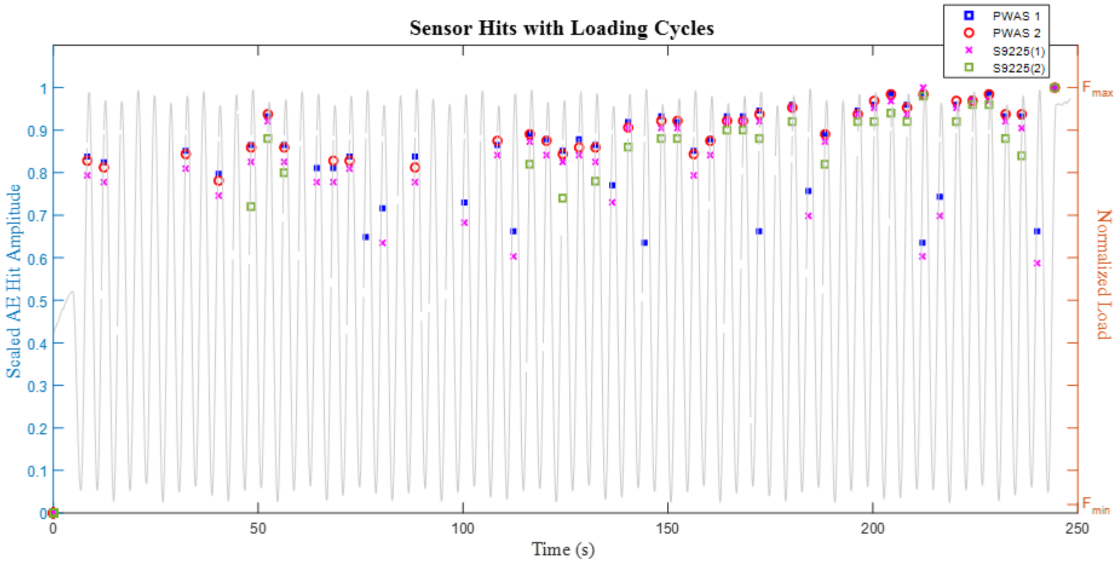

Figure 2.21 Sensor hits and loading for 60 cycles with loading frequency of 0.25 Hz.

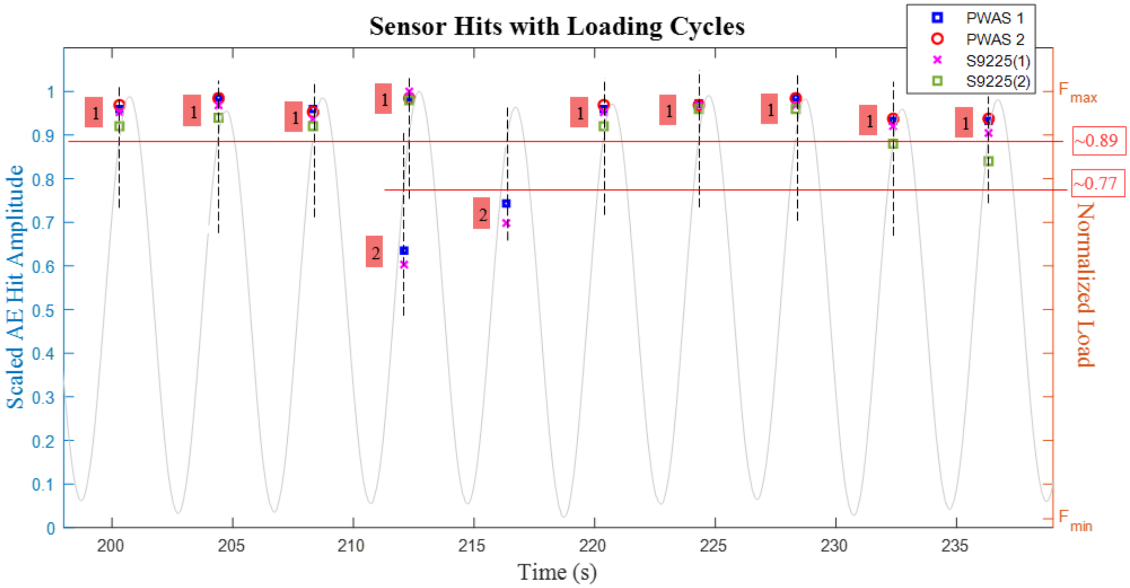

Figure 2.22 Sensor hits and loading for 10 cycles with loading frequency of 0.25 Hz assigned to groups 1 or 2.

A typical group 1 waveform from all four sensors can be seen in Figure 2.23. Here, there are consistently high amplitudes and had frequency peaks at ~150 Hz, ~275 Hz, and ~375 Hz. Group 2 waveforms have only low frequency content and have lower amplitudes. The group 2 corresponding sensor signal waveforms for the hit at 212.34 s can be seen in Figure 2.24.

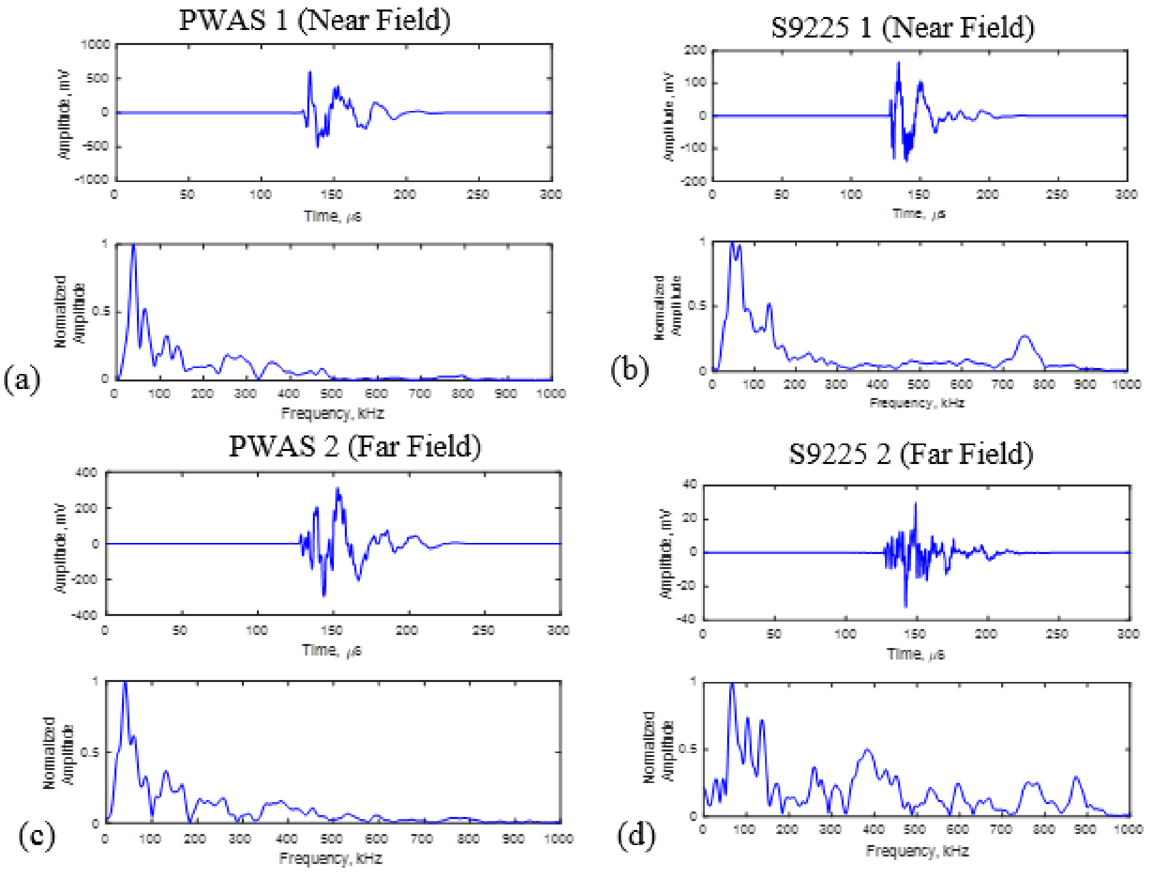

Figure 2.23 Group 1 waveforms for (a) near field PWAS 1, (b) near field S9225 1, (c) far field PWAS 2, and (d) far field S9225 2 with loading frequency of 0.25 Hz.

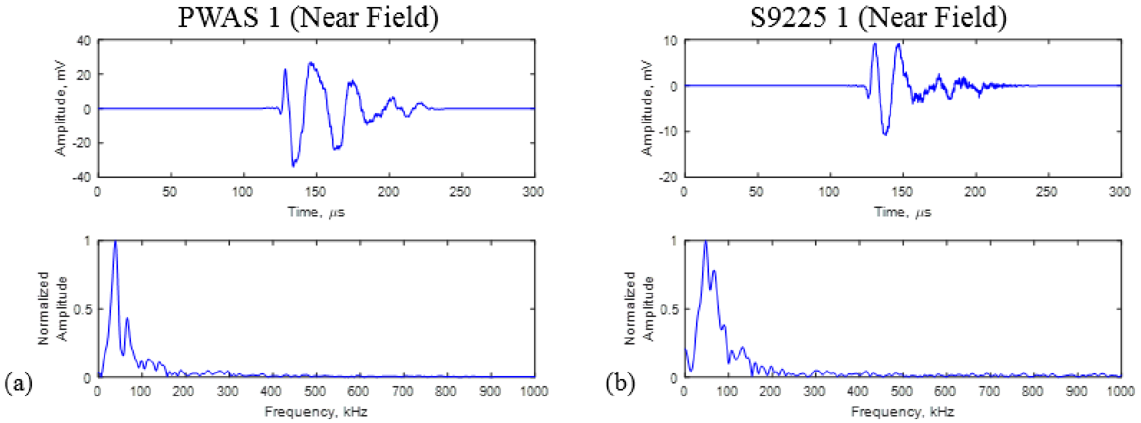

Figure 2.24 Group 2 waveforms for (a) near field PWAS 1, and (b) near field S9225 1 with loading frequency of 0.25 Hz.

2.5.5 *Waveform groups for 60 cycles at 0.1 Hz*

The specimen was sinusoidally loaded to a maximum load of 12.3 kN, R=0.1 for 60 cycles at a loading frequency of 0.1 Hz. Many hits appeared during these 60 cycles as seen in Figure 2.25. This figure also shows the normalized cyclic loading that was recorded from the strain gage. A select set of 10 cycles was chosen to visualize the results of the load at which the hits occurred. This plot along with the group numbers (as seen in blue), can be seen in Figure 2.26. All signals were captured during the loading of the specimen and none during unloading. Here, only one signal signature appeared during these 60 cycles that appeared to be a group 1 waveform. The hits appeared at different amplitudes and loads. The first load was at 90% of the maximum load, which corresponds to 11.07 kN (2488.5 lbf), and the second load occurred at 52% of the maximum load, which corresponds to 5.396 kN (1437.8 lbf). The group 1 waveform that appeared at 488.68 s can be seen in Figure 2.27. As you can see, this group 1 waveform is like the signal signatures of group 1 from the previous sections because of the low frequency content as well as having peaks at ~150 Hz, ~275 Hz, and ~375 Hz.

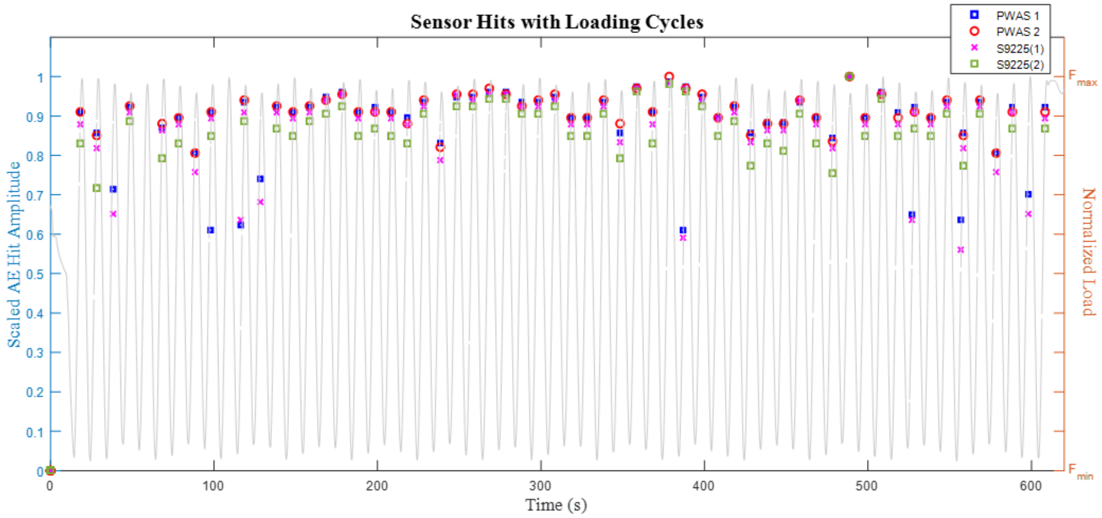

Figure 2.25 Sensor hits and loading for 60 cycles with loading frequency of 0.1 Hz.

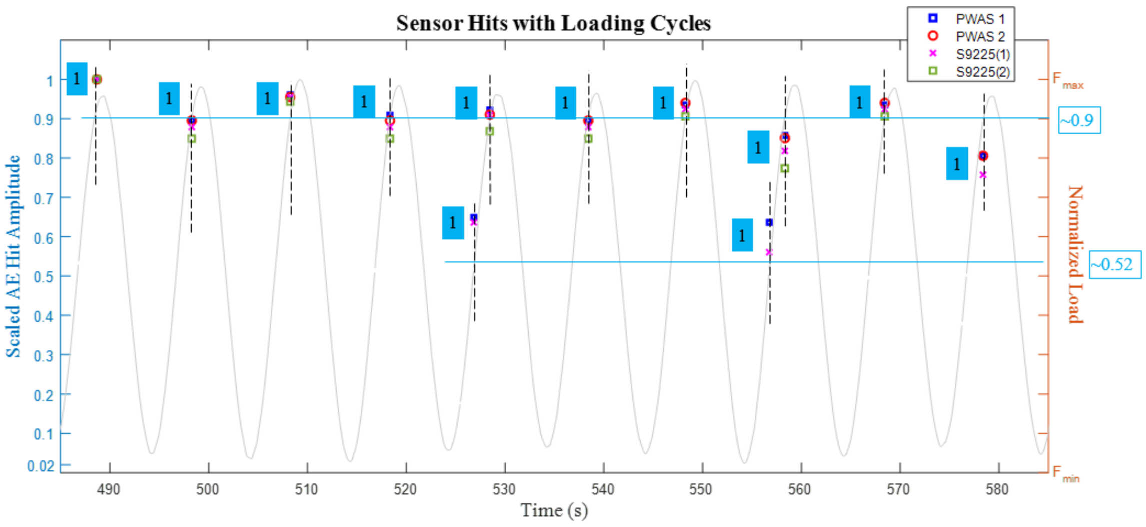

Figure 2.26 Sensor hits and loading for 10 cycles with loading frequency of 0.1 Hz assigned to group 1.

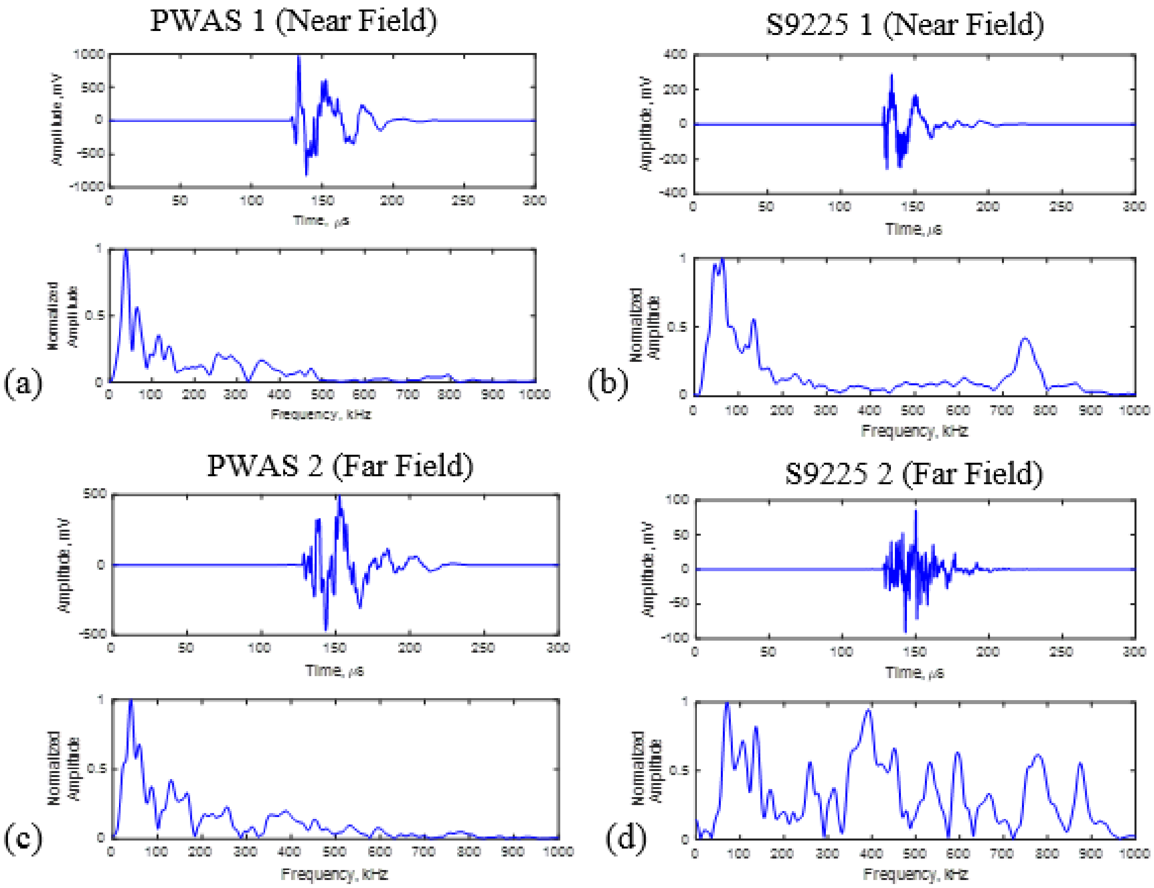

Figure 2.27 Group 1 waveforms for (a) near field PWAS 1, (b) near field S9225 1, (c) far field PWAS 2, and (d) far field S9225 2 with loading frequency of 0.1 Hz.

2.5.6 Waveform groups for 60 cycles at 0.07 Hz

During the 60 cycles at 0.07 Hz, a total of 273 hits occurred from all four sensors during a 60 cycle sinusoidal loading (65 hits from PWAS 1, 56 hits from PWAS 2, 94 hits from S9225 1 and 58 hits from S9225 2). All the hit amplitudes from the 60 cycles were normalized and plotted on one graph along with the normalized sinusoidal load (recoded from the strain gage) and can be seen in Figure 2.28. The hits from a select 10 cycles were chosen to analyze. These 10 cycles had hits that varied the most in amplitude and percent of the maximum load in which the hit occurred. The 10 cycles with grouped waveforms (seen in green) can be seen in Figure 2.29. All signals were captured during the loading of the specimen and none during unloading.

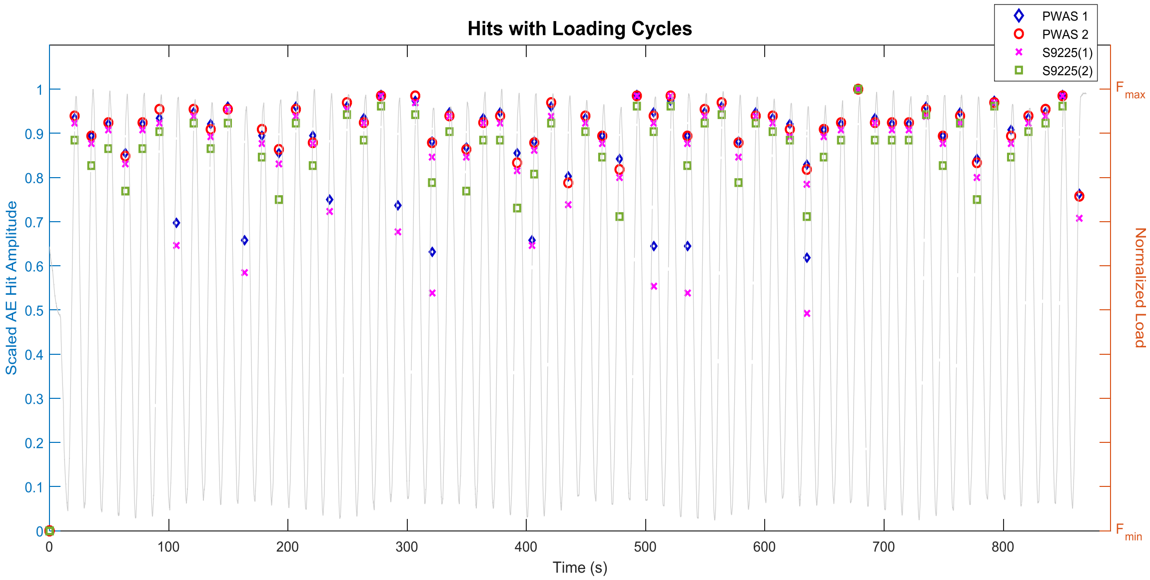

Figure 2.28 Normalized hit and normalized load for 60 cycles for AE hits from all sensors with loading frequency of 0.07 Hz.

As seen in Figure 2.29, there are two different groups. Group 1 occurred most often and tended to have a higher amplitude and occurs at ~92% of the maximum load which is 11.316 kN (2543.8 lbf). Typically, in group 1, all four sensors captured an AE event. A typical group 1 waveform occurring at 363.81 s can be seen in Figure 2.30. The group 1 frequency domain has a majority of low frequency content but also has frequency peaks at ~150 Hz, ~275 Hz, and ~375 Hz. On some occasions, the group 1 signals had low amplitudes and occurred at 57% of the maximum load which is 7.011 kN (1576.05 lbf) but still had the typical group 1 waveform. An example of this low amplitude group 1 hit cluster occurs at 404.69 s. Group 2 waveforms occurred at ~92% of the maximum load which is 11.316 kN (2543.8 lbf). Group 2 signals have low amplitudes and only occur in the near field sensors. They have only low frequency content which can be seen in Figure 2.31.

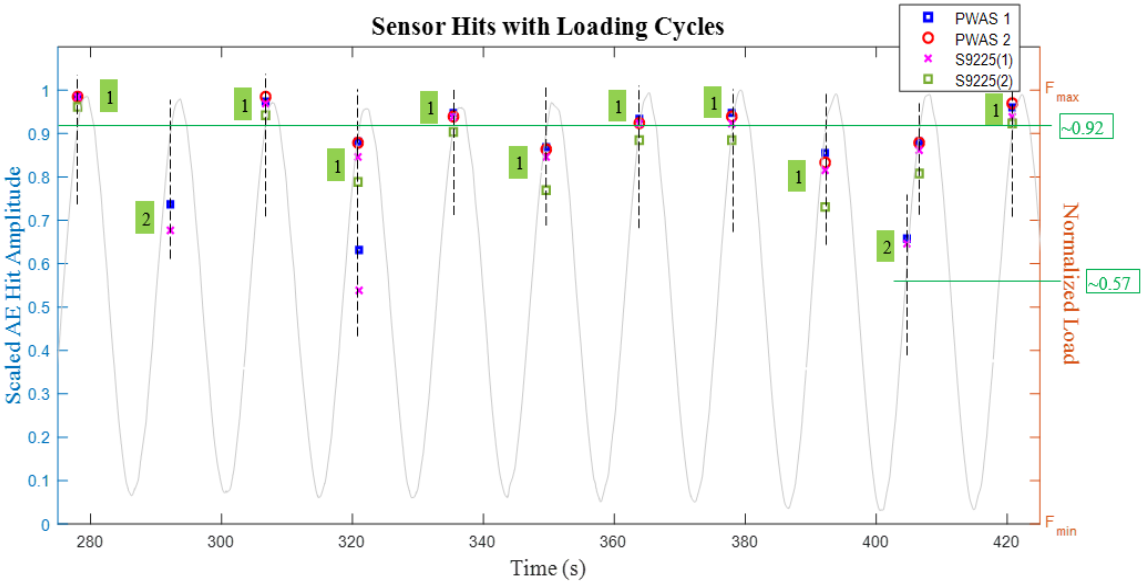

Figure 2.29 10 cycles with waveforms assigned to either group 1 or 2 with loading frequency of 0.07 Hz.

2.6 SUMMARY AND CONCLUSIONS

Acoustic emission signal detection is a very precise process. The signal signatures can change as a result of even the smallest change in any parameter. Because of this, AE signals resulting from the data collection process were studied. The results show that the change in loading frequency does not change the signal signature (group 1 and group 2 remain the same for all evaluated loading frequencies). It is important to mention that the percent of the maximum load the hits occur at increase as the loading frequency decreases.

Due to parameter changes, it is important to collect as much data as possible to monitor the signals. This leads us to improve the method of data collection. This method includes cameras to video tape and capture images of the crack, eddy current measurements to measure the crack length, and analyzing the impedance of the PWAS to ensure debonding does not occur.

It is also important to mention that out of all the data collected, AE signals were only captured during the loading of the specimen and not during the unloading. This proves that differentiating between crack growth signals and crack rubbing and clapping signals will be more difficult since crack growth signals will likely appear during loading of the specimen as well.

The repeatability of the experiment is important to note as well. It appears that the signals in Group A and Group G reviewed from Y. Bhuiyan [19] in section 2.2.2 were similar to AE signals in Group 1 and Group 2 (section 2.5), respectively. This proves that AE signals can be repeated in the case of two different LCF specimen

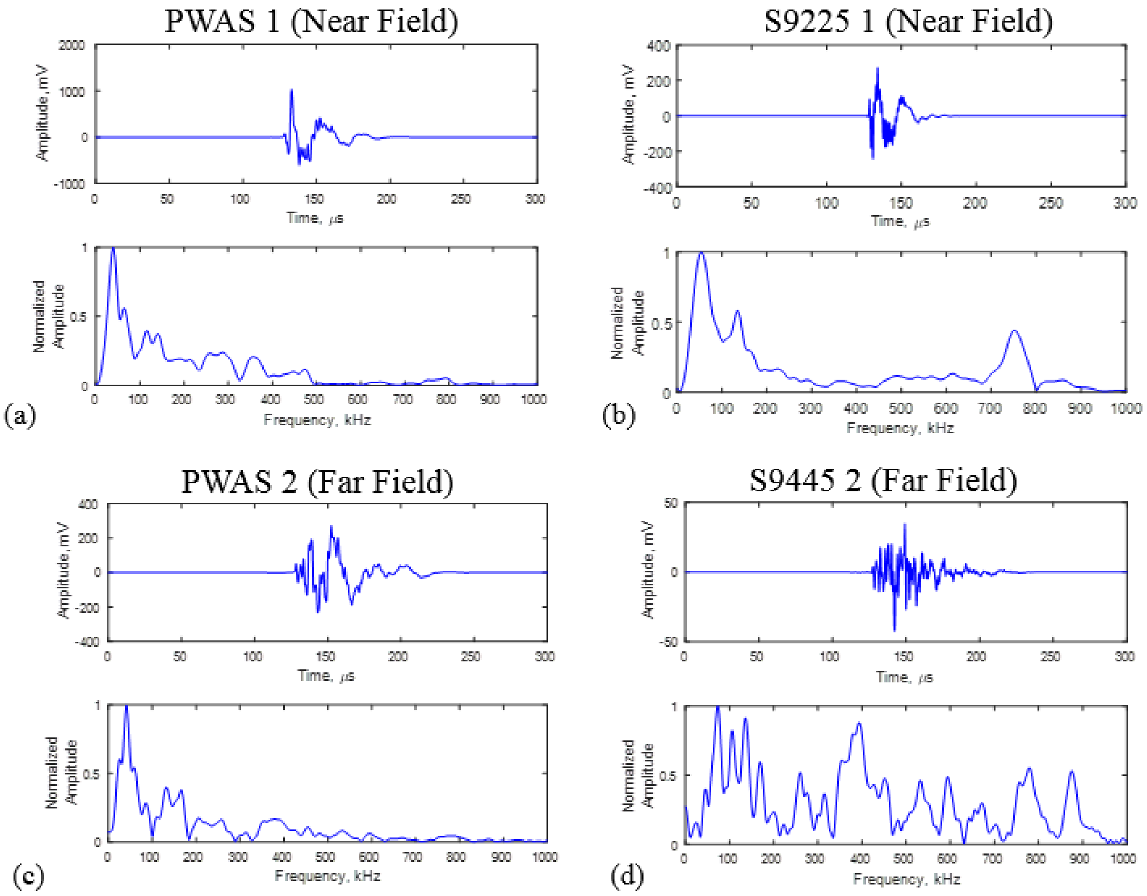

Figure 2.30 Group 1 waveform for (a) near field PWAS 1, (b) near field S9225 1, (c) far field PWAS 2, and (d) far field S9225 2 with loading frequency of 0.07 Hz.

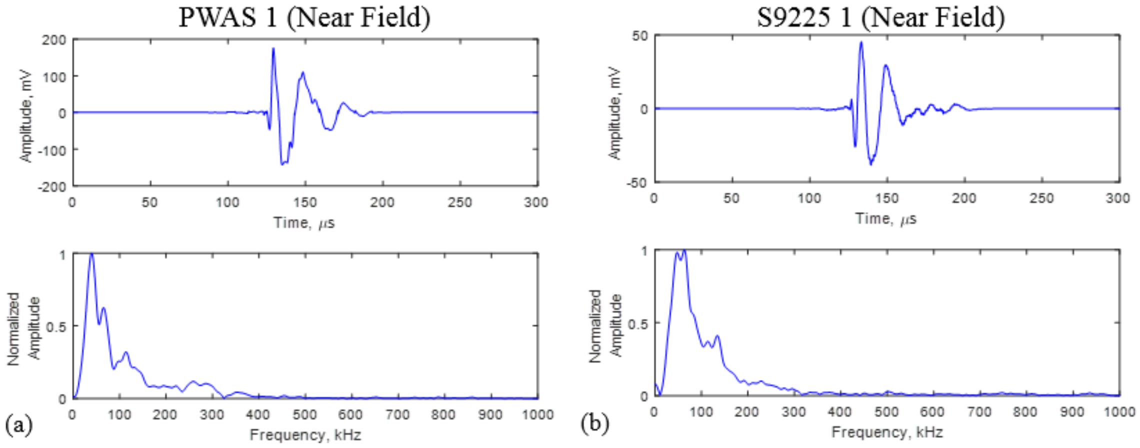

Figure 2.31 Group 2 waveform for (a) near field PWAS 1, and (b) near field S9225 1 with loading frequency of 0.07 Hz.

CHAPTER 3

INTRODUCTION TO ARTIFICIAL INTELLIGENCE TECHNIQUES

As previously mentioned, the goal of this research is to be able to non-destructively evaluate aerospace structures. In order to reach that goal, artificial intelligence (AI) needs to be implemented to understand the physical meaning behind the signal processing results and then classify future data without the help of human intelligence. Two major types of AI are machine learning and deep learning.

Machine learning starts with determining signal signatures or extracting features from a data set. Feature extraction can be performed subjectively or objectively. Once a method of feature extraction has been completed, unsupervised machine learning algorithms can be used to cluster the data. Once the data has been clustered, classification models can be trained for a computer to classify future data.

Deep learning is more complicated and requires more data for classification in comparison to machine learning. The major concept of deep learning is neural networks. A neural network imitates the process of neurons firing in the human brain. There are many different types of neural networks including artificial neural networks, LSTM networks, and convolutional neural networks.

3.1 ARTIFICIAL INTELLIGENCE STATE OF THE ART

Artificial intelligence (AI) is defined as the theory and development of computer systems able to perform tasks that normally require human intelligence, such as visual perception, speech recognition, decision-making, and translation between languages [25]. AI is an extremely smart human aid that has the capability to learn from experience and adjust itself to new inputs to improve performance. AI is an extremely prevalent topic used in many aspects of our everyday lives such as music recommendations, mobile banking fraud detection, google search suggestions, etc. Artificial intelligence has two major branches. The first branch is machine learning and the second branch is deep learning. Machine learning is based on extracting features that help place an input into a certain category. In feature extraction, principal component analysis (PCA) is an extremely important concept that reduces the dimensionality of the extracted features. Those features are then learned through machine learning models such as support vector machine (SVM), k-nearest neighbor, discriminant analysis (DA), etc. Smarsly et. al [26] defines AI as a term that describes the ability of a computational entity to perform activities in a fashion that usually characterizes human thought which is how deep learning is performed. Deep learning takes the entire input and categorizes it in a way like neurons in the human brain. A popular deep learning process is called artificial neural networks (ANN).

Artificial intelligence has also made many appearances in the engineering industry. The engineering industry uses AI for applications like sophistication of automobiles, using image processes to identify structural abnormalities, damage detection in structural health monitoring (SHM), etc. SHM is a research subject that could greatly improve with the help of artificial intelligence. In the aerospace field, SHM could help reduce turn-around time for aircrafts, reduce labor costs for maintenance, detect damages, and predict the life of the aircraft structure. Manson and Worden [27] used kernel density function (KDF) and artificial neural networks (ANN) to study the effect of panel removal on the transmissibility of a Gnat aircraft trainer starboard wing.

Many researchers have used AI techniques in SHM for monitoring acoustic emission (AE) vibration signals. Elforjani and Shanbr [28] extracted features from AE signals and used machine learning techniques such as ANN, Gaussian process (GP) and SVM to determine the remaining useful life (RUL) of ball bearings. Ahn et. al [29] used PCA and SVM for acoustic emission pipeline leak-early detection. Nasir et. al [30] used feature extraction and AI to monitor the AE circular sawing process of Douglas fir wood under extreme cutting conditions. Jahanbakhshi et. al [31] studied noise pollution from AE due to a John Deere combine harvester using ANN. Manson et. al [32] used artificial neural networks to detect damage on an aircraft wing through transmissibility.

3.2 MACHINE LEARNING CLUSTERING TECHNIQUES

As previously seen in Chapter 2, AE waveforms can confidently be separated between noise signals and signals originating from the damage. Once the signals originating from the damage can be extracted, their waveforms are subjectively grouped and hypothesized whether the group of signals originate from crack growth or crack rubbing and clapping. These signals must now be objectively grouped or clustered to gain pattern recognition. This method of grouping clusters to then determine their meaning is called unsupervised learning and is the most appropriate method for clustering of fatigue crack damage. Some unsupervised methods that are widely used for feature extraction in damage detection is the hierarchical tree, principal component analysis (PCA), and *k*-means clustering.

3.2.1 Hierarchical clustering analysis to determine highest variance features

Hierarchical clustering analysis is vastly present in the biomedical field for signal processing such as cancer classification, breast carcinoma identification, blood plasma lipidomic identification, etc., but it has expanded to damage detection in SHM [33]. The simplified hierarchical clustering procedure is as follows; the data points are evaluated based on the feature distance then the points are grouped into a binary hierarchical linkage and finally, the hierarchical tree is cut into clusters. Each of these steps are detailed below.

The feature distance evaluation between each pair of points where each point represents a hit or measurement is expressed in equation (7).

$$Y_{r,s} = Dis(F^r, F^s) \tag{7}$$

where *r* and *s* signify two different measurements, *F* is the ending point of the feature vector in a high-dimensional space, *Y* is the distance between the two features of *r* and *s* and *Dis* is the possible calculation of distance. This distance calculation can be done in many ways including Euclidean distance, Chebyshev distance, Minkowski distance, etc. The binary hierarchical tree is expressed in the equation below.

$$C = L(Y_{r_1,s_1}, Y_{r_2,s_2}) \tag{8}$$

where C is the derived clusters and L is the linkage calculation. One linkage will be the shortest feature distance between points. Finally, the hierarchical tree is cut into clusters. For this process, the relative distance between clusters is normalized. The measurements with the highest relative distance will include all the measurements. As the relative distance decreases, the dissimilarity between measurements also decreases. For example, a clustered hierarchical tree is shown for 16 observations in Figure 3.1.

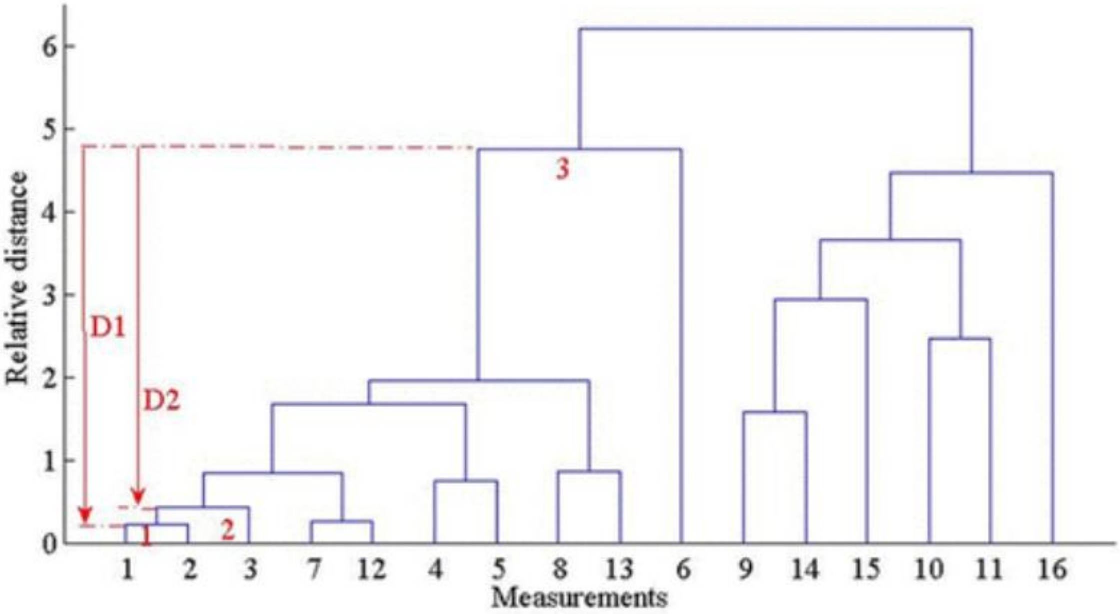

Figure 3.1 Hierarchical tree split into clusters based on relative distance.

In this figure, cluster 3 (written in red) describes all the measurements due to damage and all the measurements below it in the tree are due to damage. Clusters can be represented by D1 and D2. Cluster 2 is a sub-cluster of cluster 3, and cluster 1 is a sub-cluster of cluster 2. As the relative distance of cluster D decreases, the more similar the measurements are within that cluster. This hierarchical tree allows one to understand the correlation between all the 16 observations.

3.2.2 The k-means algorithm approach to pattern recognition

The *k*-means algorithm approach is an unsupervised learning method that finds optimal solutions to the data set with respect to the nearest mean value [34]. The *k* is the specified number of clusters desired. The *k*-means algorithm works by finding the centers of each *k* group through an iterative process starting with *k* random data points and the average between them. The random data point or feature vector is assigned to a cluster based on its distance from the mean vector. The iterations start with finding the feature vector that is closest to the mean vector and then iterates to the next closest vector and repeats until all the data points have been assigned to a cluster [35].

3.2.3 Principal component analysis

Principal component analysis (PCA) is based on projecting data by means of a linear transformation to get a new data set on a new Cartesian coordinate system. The axes of this new cartesian coordinate system are based on the largest variance of the data set and are called the principal component scores [36]. The new linear combination of the data with the least variance is eliminated. It is important to normalize the data. If the data is not normalized, it will create importance of one feature over another. Unless there is a specific parameter such as rise time, peak amplitude, etc. that is desired to receive more importance over another, it is recommended to normalize the data [37]. Obtaining the new set of Cartesian coordinates can follow the equations below where $\{x\}$ and $\{z\}$ denote vectors in the measured and reduced space, respectively. The covariance matrix, $[\Sigma]$, can be found from the equation below.

$$[\Sigma] = \sum_{i=1}^{N} (\{x\}_i - \{\bar{x}\})(\{x\}_i - \{\bar{x}\})^T \tag{9}$$

where $\{x\}_i = (x_{1i}, x_{2i}, \ldots, x_{pi})$ and $i = (1, \ldots, N)$, $\{\bar{x}\}$ is the vector of all the means of the *x*-data and N is the number of hits recorded. The covariance matrix can be decomposed to be,

$$[\Sigma] = [A][\Lambda][A]^T \tag{10}$$

where $[\Lambda]$ is diagonal and $[A]$ is the transformation matrix. The transformation to principle components is then expressed as,

$$\{z\}_i = [A]^T(\{x\}_i - \{\bar{x}\}) \tag{11}$$

After completion of the equations, $\{z\}_1$, the highest variance component can be plotted against $\{z\}_2$ which is the second highest variance component. Each hit will be placed on the graph based on their variance component values or their component scores. An example of PCA can be seen in the figure below.

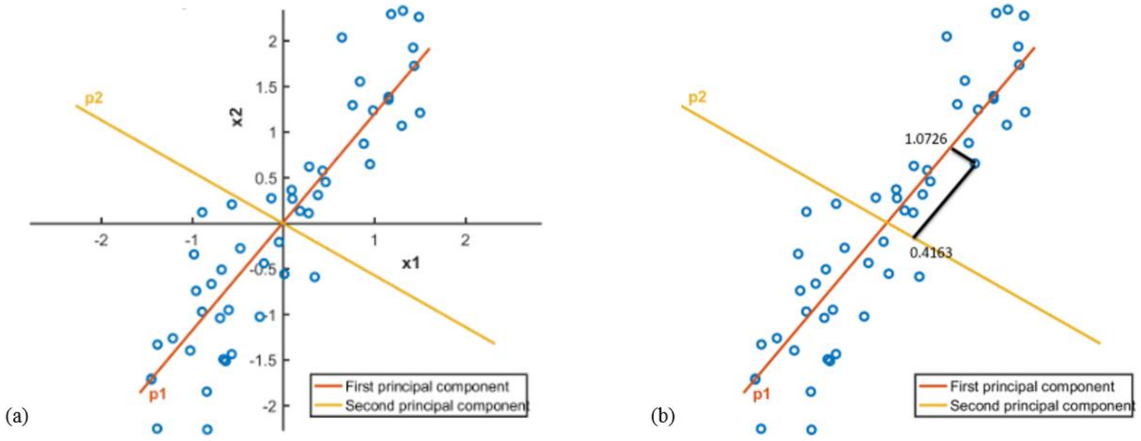

Figure 3.2 (a) Linear principal components viewed on the original axis and (b) the principal components shown as the new coordinate system. [38]

3.3 MACHINE LEARNING CLASSIFICATION MODELS

The idea of machine learning (ML) is that one can learn relationships from a series of data and the data can be classified using either supervised, unsupervised and semi-supervised learning. Supervised learning is clustering data based on knowing a certain feature correlates to a known type of source (noise, damage, etc.). Unsupervised learning is clustering based on high variance features and then deciding the type of source it came from. Semi-supervised learning is a mixture between the two. For instance, you may know there are exactly three sources so the data can be organized into three clusters and the source features are then determined. ML classification models are essential when attempting to non-destructively evaluate an aerospace structure by assigning an AE event to a cluster. This section will discuss supervised PR classification models including discriminant analysis (DA), support vector machines (SVM), k-nearest neighbor (KNN), decision trees (DT), and Naïve Bayes (NB). All these PR algorithms are supervised methods and are well suited for the applications discussed in the next chapter.

To use machine learning classification models, a dataset with extracted features must be present. Supervised learning techniques involve training a classification model with data and then introducing new data to test the accuracy of the model. Typically, when training a model, you will split your data into a training set and a testing set. The training set will sometimes be referred to as the original data and the testing set will sometimes be referred to as the new data.

3.3.4 Discriminant analysis model classification

Discriminant analysis (DA) is a supervised learning technique used for clustering. A quadratic discriminant analysis can be done for a set of PCA AE data. The quadradic discriminant equation can be seen in the equation below [36].

$$p\left(\underline{x}, \underline{\bar{x}}, [\Sigma]\right) = \frac{1}{(2\pi)^{d/2}\sqrt{|\Sigma|}} exp\left\{-\frac{1}{2}\left(\underline{x} - \underline{\bar{x}}\right)^{T} \Sigma^{-1} \left(\underline{x} - \underline{\bar{x}}\right)\right\} \tag{12}$$

where $\underline{\bar{x}}$ is the mean vector, $\underline{x}$ is the feature vector, *d* represents the number of dimensions and $|\Sigma|$ represents the determinant of the covariance matrix. Discriminant analysis assumes classification with a boundary and a normal probability distribution, but there is no assumption of independence in each predictor. There are two basic types of discriminant analysis; linear and quadratic. Linear DA assumes the size and shape of the distribution is uniform for all clusters, meaning equal covariance matrices. An example of this can be seen in Figure 3.3a. Quadratic DA assumes the size and shape of the distribution is different for each cluster, so the covariance matrices are not equal. An example of quadratic DA can be seen in Figure 3.3b.

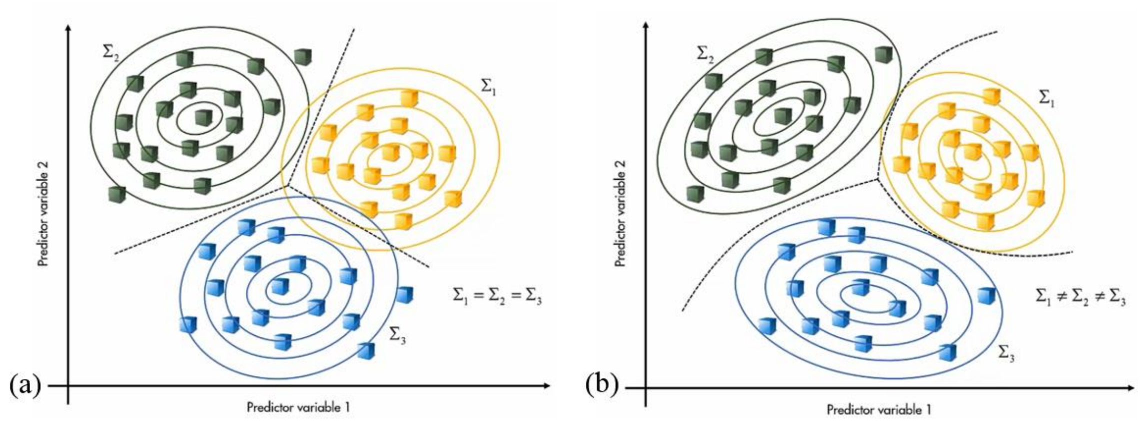

Figure 3.3 (a) Linear discriminant analysis and (b) quadratic discriminant analysis. [38]

3.3.5 Support vector machine model classification

Support vector machine (SVM) is a supervised ML technique. This technique separates between clusters based on a straight line in two dimensions, otherwise known as hyperplanes [39]. The basic concept of the method is finding arbitrary hyperplanes that separate clusters (Figure 3.4a) and then using those hyperplanes to find the optimal hyperplane which is furthest from all the data (Figure 3.4b). The optimal hyperplane for a linear SVM can be found from equation (13).

$$D(\{x\}) = \sum_{i=1}^{N} \alpha_i y_i < \{x\}_i, \{x\} > \tag{13}$$

where N is the number of datapoints, α_i are the Lagrange multipliers, and y_i is the cluster label. There also exists a nonlinear SVM which is based on discriminant analysis and is expressed by,

$$D(\{x\}) = \sum_{i=1}^{N} \alpha_i y_i k(\{x\}_i, \{x\}) \tag{14}$$

where $k(\{x\}_i, \{x\})$ is the kernel function. Equations (13) and (14) follow the rule that if $D(\{x\}) > 0$, it's assigned to cluster 1 and if $D(\{x\}) < 0$, it's assigned to cluster 2. This is the case for only two clusters. When there is an example of more than two clusters, multiclassification problems use a combination of multiple binary classifiers to create hyperplanes. The method of multiple binary classifiers is similar to linear discriminant analysis but instead, SVM uses the method of largest margins between hyperplanes rather than distributions.

SVM can also be used as an unsupervised learning approach as well. For the unsupervised learning approach, the algorithm is based on the origin set of data and a one-cluster hyperplane with the largest possible hyperplane is used.

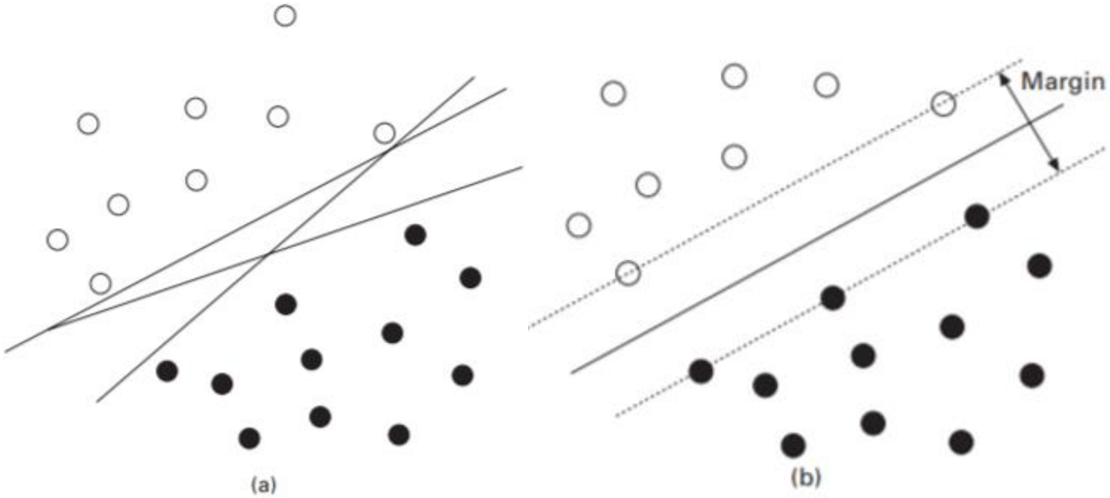

Figure 3.4 SVM clustering for (a) arbitrary hyperplanes, and (b) optimal hyperplane. [39]

3.3.6 k-nearest neighbor model classification

k-nearest neighbor is like *k*-means clustering except that *k*-nearest neighbor is a supervised learning technique. A model is trained with already classified data in a specified number of clusters. When new data is introduced, the new data is clustered based on the already classified data the new data is closest to. The *k* value is specified to compare the new data to *k* known datapoints. In Figure 3.5, there are three different clusters, green, blue and yellow. As you can see in the figure, if a new datapoint is introduced (such as the grey one) it would be clustered as yellow because two out of the *k* =3 closest datapoints are also yellow.

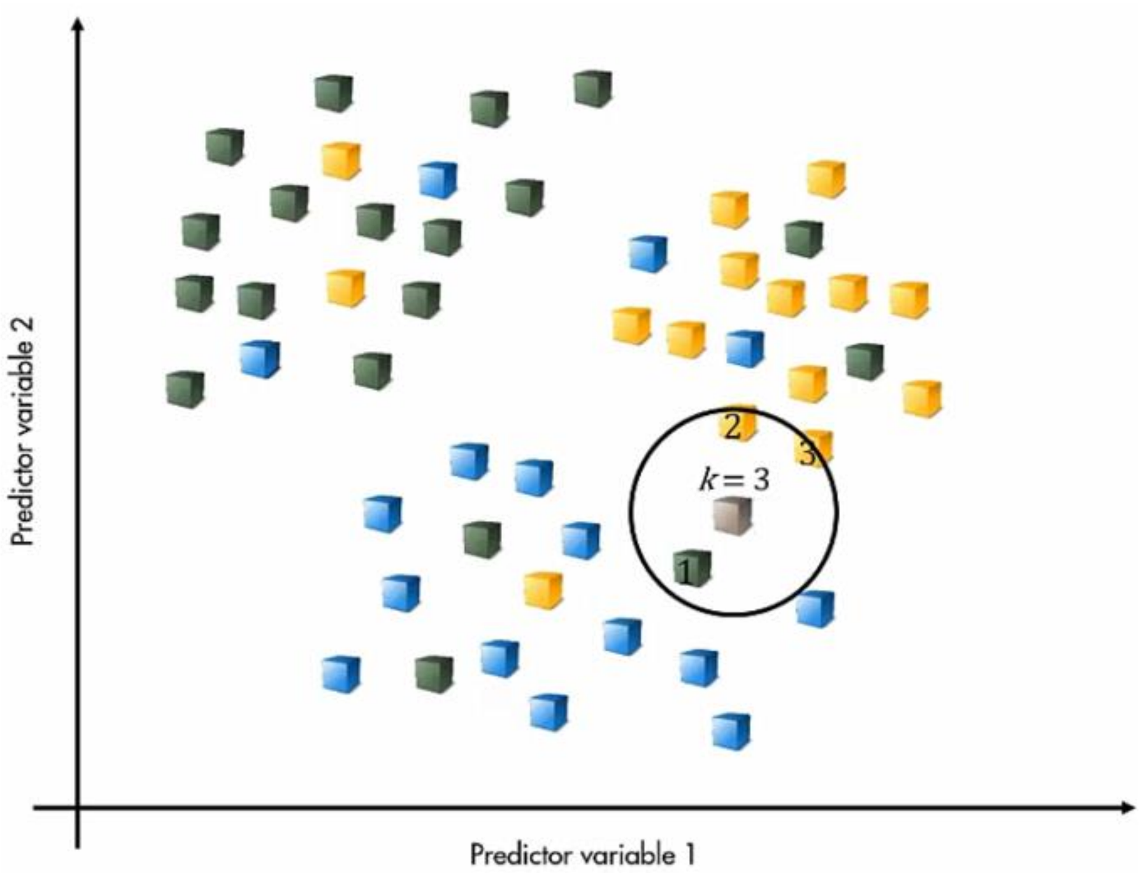

Figure 3.5 Example of k-nearest neighbor clustering. [38]

3.3.7 Decision trees model classification

A decision tree model is considered a supervised classification model. It creates clusters by building a sequence of yes or no questions. The classified testing data is used, and boundaries are made to split them up into clusters by considering all the possible splits in each variable. When new data is introduced, it is clustered very quickly since the information simply runs through the binary sequence. A simple example of clustering data into three different groups can be seen in Figure 3.6.

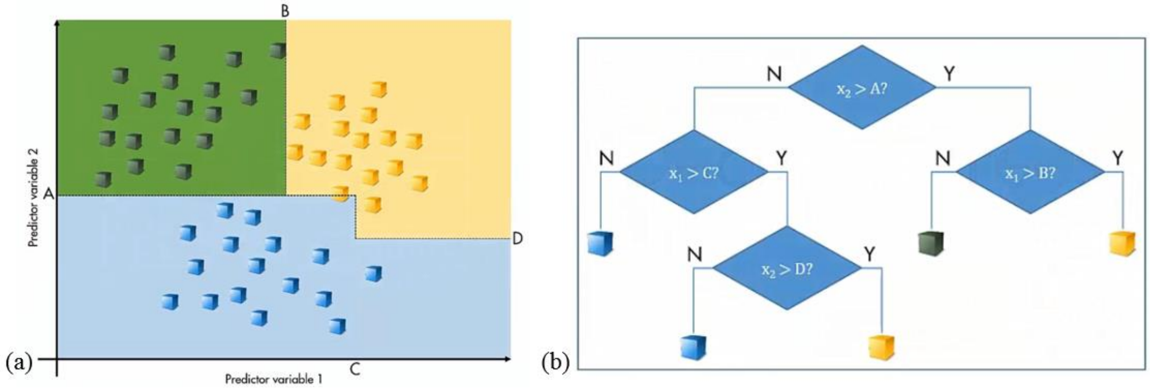

Figure 3.6 (a) Classified data split into various boundaries, and (b) decision tree binary sequence used to cluster new data. [38]

3.3.8 *Naïve Bayes model classification*

Naïve Bayes classification model is a supervised learning technique that uses a Gaussian mixture model to cluster training data. When looking at the training data in a feature plot, we assume the dataset comes from an underlying distribution as seen in Figure 3.7a. Using an underlying distribution can reduce the influence of outliers. When new data is introduced, a probability is calculated based on where it lies on the distribution. The probabilities are solved using equation (12) from sub-section 3.3.4. The new data point is classified based on the classifier with the highest probability. An example of this can be seen in Figure 3.7b, where a new datapoint that was initially introduced as grey has been placed in the blue cluster.

3.4 DEEP LEARNING NEURAL NETWORKS

Neural networks are a form of supervised learning. There are many kinds of neural networks, such as classical neural networks and convolutional neural networks. Neural networks are a well-established method of machine learning (ML) and are based on the neurons that add to the structure of the brain [39]. This learning technique is a computing paradigm to the way we learn with our brains. The basic organization of a neural network is described by the multilayer perception (MLP). MLP is a collection of neurons (or nodes) arranged in layers with an input, hidden layers, then an output [40]. The MLP diagram is shown in Figure 3.8.

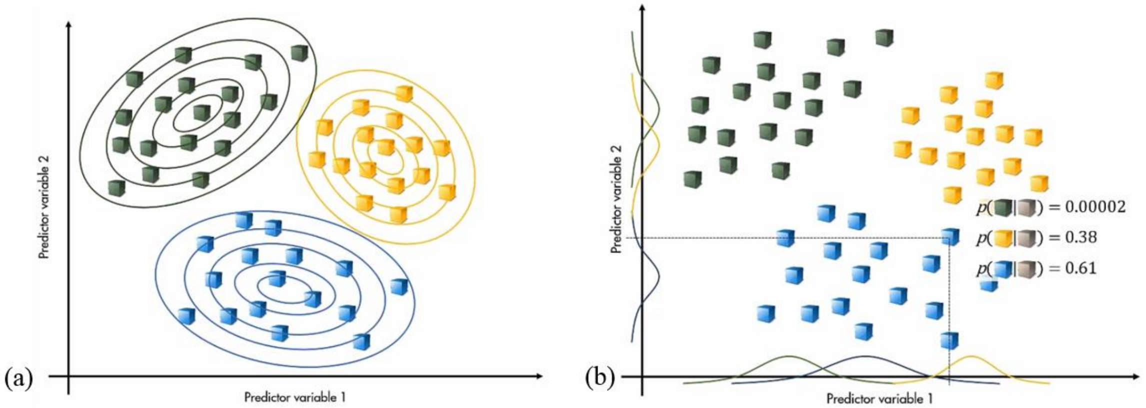

Figure 3.7 (a) Gaussian Mixture model distributions for testing data and (b) new data point probability based on Naïve Bayes classification model. [38]

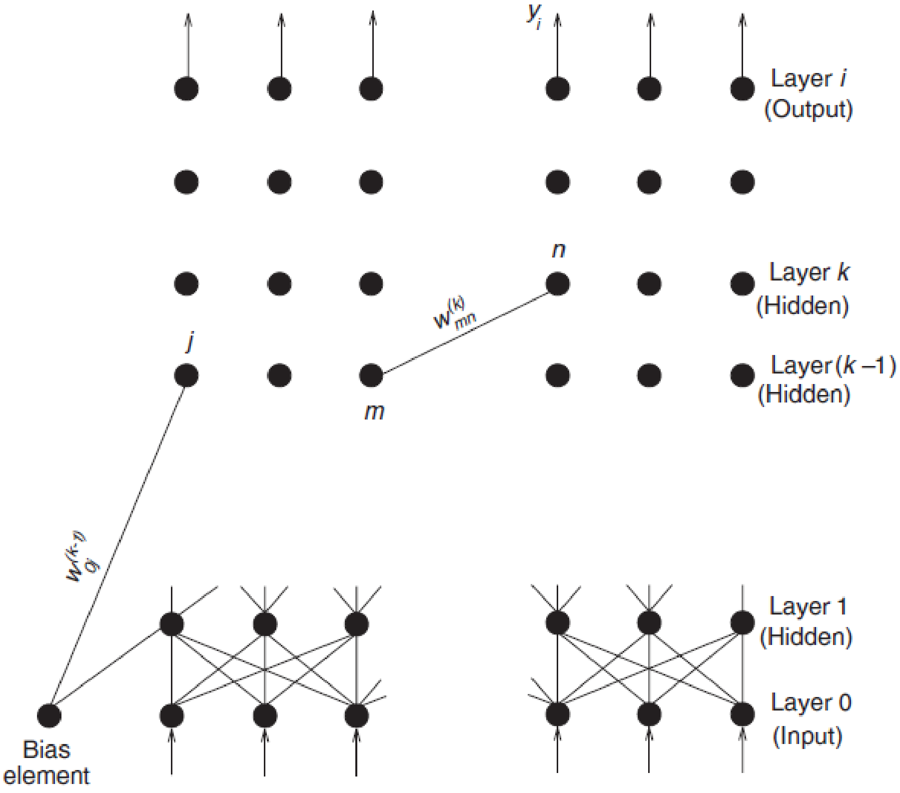

Figure 3.8 Multilayer perception (MLP). [39]

Each node *i* is connected to each node *j* in the figure and they are connected through weights (ω_{ij}). The signals passing through the MLP can be described by,

$$x_i^{(k)} = f\left(z_i^{(k)}\right) = f\left(\sum_j, \omega_{ij}^{(k)} x_j^{(k-1)}\right) \tag{15}$$

where $x_i^{(k)}$ is the signal from the node *i* on layer *k*, $z_i^{(k)}$ is the excitation of the node, *f* is a nonlinear activation function, and $x_j^{(k-1)}$ is the signal from the previous layer (k-1) at node *j*. Typically, there is a training phase for neural networks that needs to take place before the method can actually be used. For training, a set of inputs is run through the MLP resulting in outputs. These outputs are then compared to the desired outputs. If the training outputs compared to the desired outputs are small enough, then the weights (ω_{ij}) are not adjusted. If the compared results are not small enough, the error is sent through the network backwards and the weights can be adjusted that way [39].

There are two major types of neural networks that will be used in this thesis: classical neural networks and convolutional neural networks. Classical neural networks are described by the passing of numbers or vectors through the MLP to classify data. Convolutional neural networks are when a collection of images is passed through the MLP.

3.4.1 Classical neural networks: LSTM

There are many different types of classical neural networks, but the one being used in this thesis is called long short-term memory (LSTM) networks. An LSTM is when the input to the neural network is an ordered sequence where information from earlier in the sequence may be important. The basic structure of an LSTM can be seen in Figure 3.9. What makes LSTM's different from other classical neural networks is its internal state and recurrent neural network. The internal state is what the node uses as a working memory space which means information can be stored or retrieved over many time steps. The recurrent neural network reuses the output from a previous step as an input for the next step. An example of an LSTM network is Apple iMessage word suggestion. As you are typing a sentence, iMessage will suggest words that will be typed next as a shortcut to spelling out full words. These suggestions are based on sentences you have typed in past texts (internal state) or based on words typed earlier in that sentence (recurrent neural network).

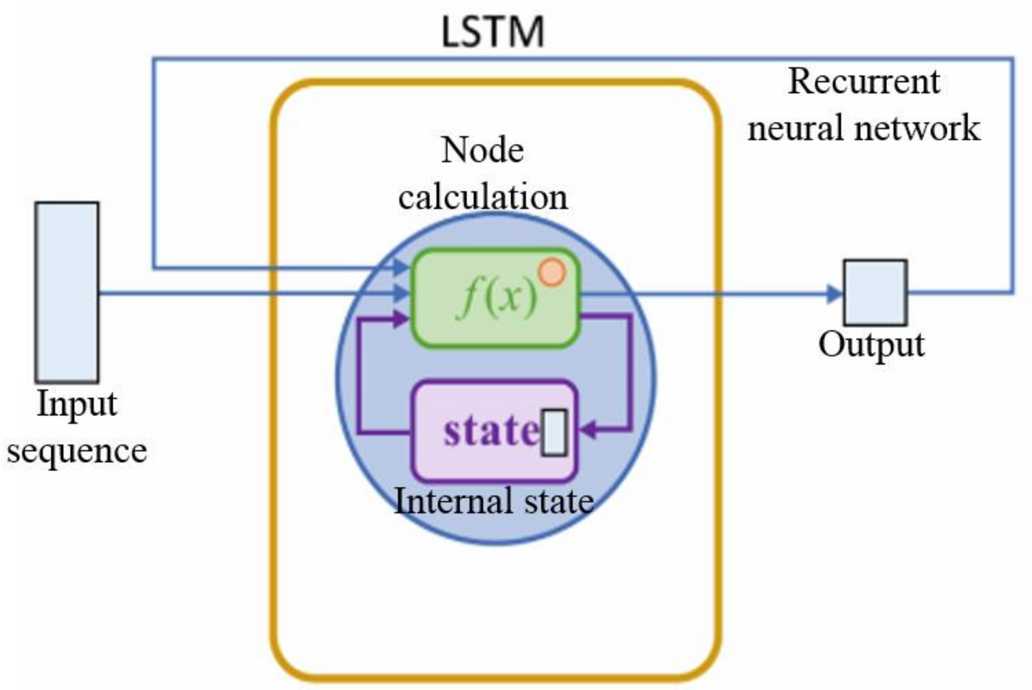

Figure 3.9 Structure of the LSTM neural network.

3.4.2 *Convolutional neural networks*

The convolutional network is a network with images as its input. These images are converted to red, green, blue (RGB) matrices and are passed through the constructed convolutional neural network. The basic construction of a convolutional neural network with an example of a 5 × 5-pixel input image to classify it as either a cat or a dog can be seen in Figure 3.10. It starts with the input image followed by the convolution layer. The convolution layer applies filters to downsize the original image to create a feature. The feature is made from the sum of the product of the values in the filter matrix and RGB matrix. The feature then passes to the rectified linear unit (ReLU) which applies a threshold to remove all negative values. The image then gets passed through the maximum pooling layer which performs down-sampling of the image to reduce its pixel size. Max pooling layer creates a smaller matrix by taking the maximum value from the selected pooling region size (the example from Figure 3.10 has a pooling size of 3 × 3). Once the size of the image is reduced, it passes through the fully connected layer which is like the MLP. Finally, the image is normalized by the Softmax layer and the output it presented from the classification layer.

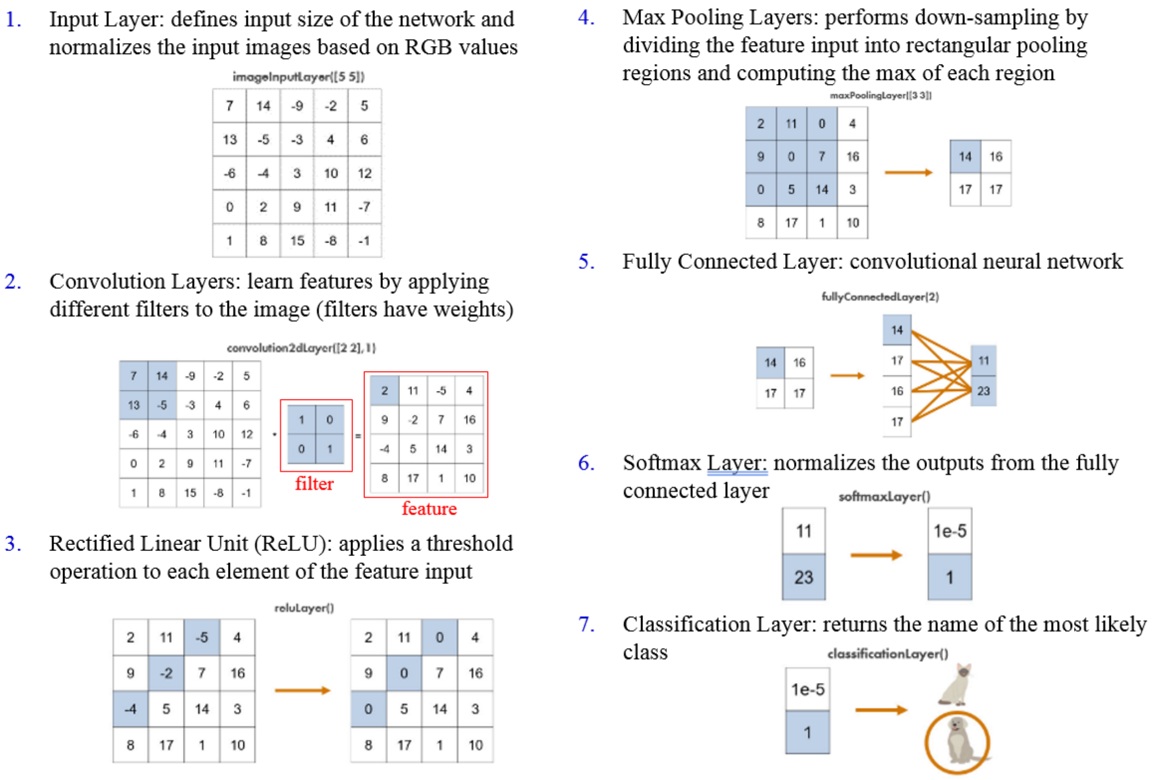

1. Input Layer: defines input size of the network and normalizes the input images based on RGB values
2. Convolution Layers: learn features by applying different filters to the image (filters have weights)
3. Rectified Linear Unit (ReLU): applies a threshold operation to each element of the feature input
4. Max Pooling Layers: performs down-sampling by dividing the feature input into rectangular pooling regions and computing the max of each region
5. Fully Connected Layer: convolutional neural network
6. Softmax Layer: normalizes the outputs from the fully connected layer
7. Classification Layer: returns the name of the most likely class

Figure 3.10 General construction of a convolutional neural network.

CHAPTER 4

MACHINE LEARNING FEATURE EXTRACTION AND MODEL CLASSIFICATION FOR EXPERIMENTAL AE SIGNALS

Acoustic Emission (AE) is a well-established method of determining the structural health of a specimen. When determining whether a specimen is deemed “healthy,” it is important to understand the signal signatures in AE waveforms based on the source. The source can be from environmental noise, crack rubbing and clapping of the faying surfaces or crack growth occurring from the crack tips.

Considering artificial intelligence, we want to have a computer classify our AE signals to help us determine crack growth signals and find information within those crack growth signals that will determine the length of the crack. The first step to achieving this goal is through feature extraction. Feature extraction can be a subjective or objective process. To subjectively extract features, a deep understanding of the signals and what they mean must be known to the researcher. If the researcher is using data that they are unsure of, the extracted features may overfit once it’s applied to a classification model. To reduce or eliminate overfitting, features can be extracted using an objective method. Objective methods of feature extraction include using statistical observations like mean, kurtosis factor, standard deviation, etc. For the purpose of understanding the machine learning process, the methods used to extract features in this chapter are subjective.

4.1 EXPERIMENTAL SET-UP AND PROCEDURE

The specimen is a 101 mm wide and 305 mm long and 1 mm thick 2024 T3 aluminum plate. The specimen has a 1 mm hole drilled into the geometric center of the plate for crack initiation. The plate was placed into an MTS machine with a maximum load of 14.05 kN and a minimum load of 1.405 kN with a loading frequency of 10 Hz. The crack initiated at 322 kcycles. Once the crack initiated, the specimen was removed from the MTS machine and was prepared with two PWAS and two S9225 sensors. The PWAS were located at 6 mm and 25 mm from the crack and the S9225 sensors were placed 6 mm and 25 mm away from the crack mirroring the PWAS. On the opposite side of the specimen, a strain gage was applied about 35 mm from the crack. The strain gage is used to monitor the load applied to the specimen. The specimen was equipped with a non-reflective boundary (NRB) to reduce reflection from the AE waves. A picture of the specimen can be seen in Figure 4.1. The method of collecting the AE waves included the Mistras AE instrumentation connected to the sensors through a pre-amplifier. Periodically, to ensure the PWAS were well bonded, an impedance measurement was taken with an Omicron Lab EMIS instrument. This method can be seen in Figure 4.2. To reduce the number of factors that affect how the AE signals look, the specimen is applied with a constant stress intensity factor (SIF). To do this, the cyclic frequency is applied at 4 Hz starting at a load of 14.05 kN and periodically reduced to 6.29 kN using the Fedderson correction factor [41]. The crack grew from ~3.5 to ~9.4 mm in an additional 188 kcycles.

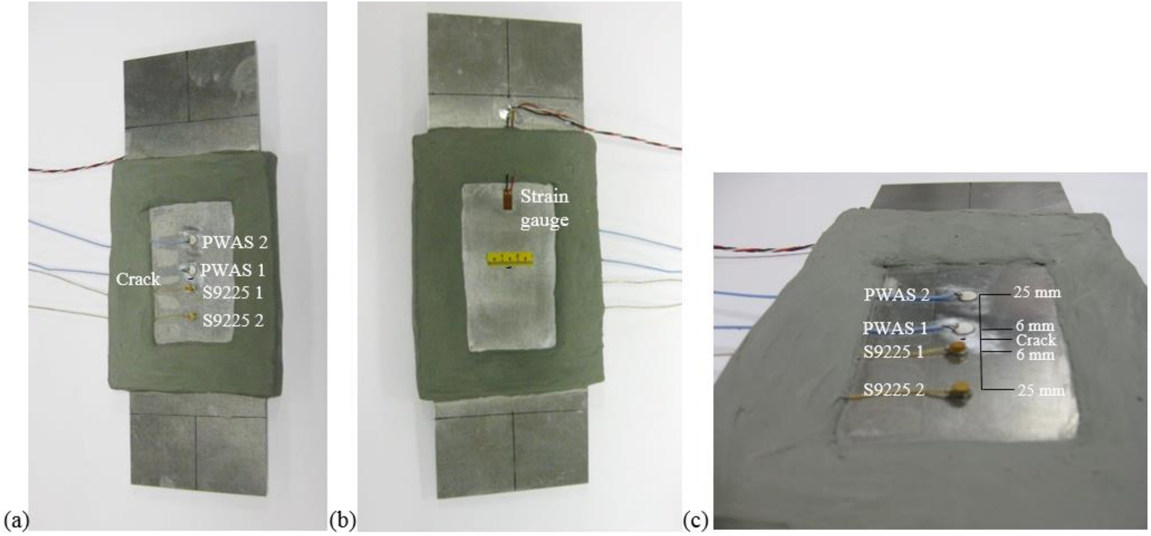

Figure 4.1 (a) AE sensor side of the specimen, (b) strain gauge side of the specimen, and (c) sensor side of the specimen with sensor distances from the crack.

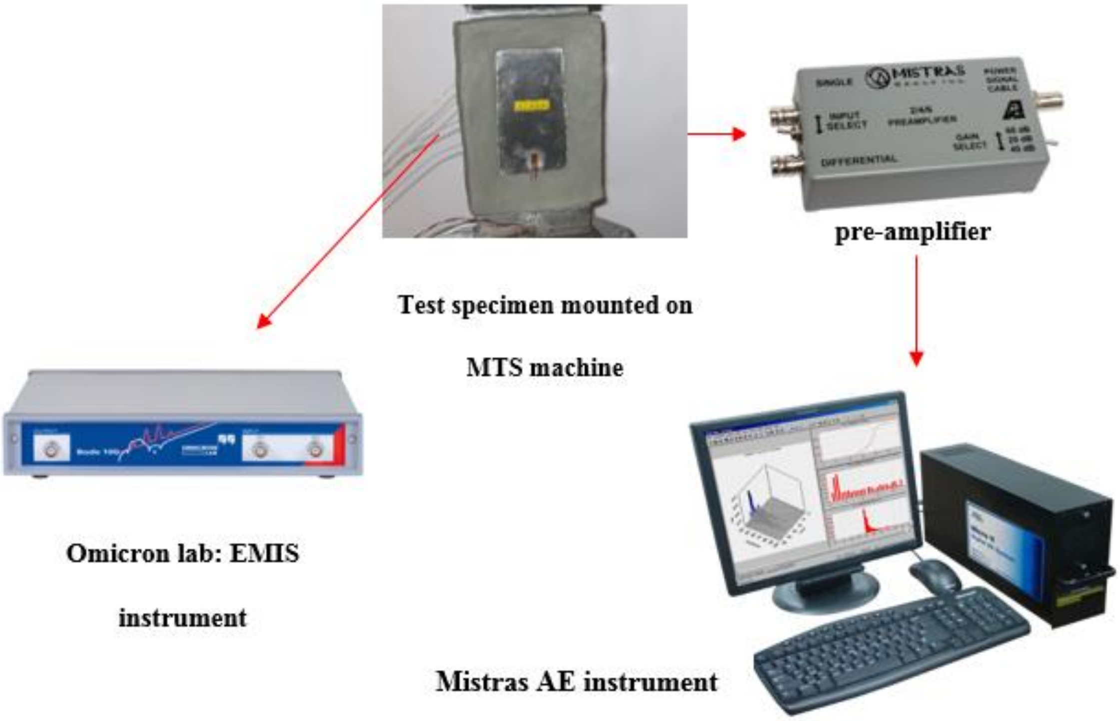

Figure 4.2 Methodology for HCF testing in the MTS machine.

4.2 Signal Detection Processing: Feature Extraction

We know there are three types of signals that are being detected. The first type of signal is due to noise. These noise signals are determined when there is a signal detected from one sensor and no other sensors in a range of 300 μs before and after the signal. A noise signal can also be present in all four sensors, but the time of arrival is the exact same. Another type of signal detected will be from crack faces rubbing and clapping, called Type 2 (T2). These signals appear in all four sensors within a 300 μs range when there is no crack growth. The third type of signal is due to crack growth called, Type 1 (T1). These signals appear in all four sensors within a 300 μs range when there is crack growth. For both T1 and T2 signals, the time of arrival of the waveform appears in the near field sensors prior to being detected by the far field sensors. By observation, as the crack grows, the T1 signals change but the T2 signals tend to remain the same. It is also observed that when the crack length is low, the crack-related AE signals are dominated by T1 signals since there is less crack surface for T2 signals to occur. Once the crack length grows, the T2 signals are dominating. For the SIF-controlled HCF specimen in question, T2 signals become dominant at a crack length of ~8 mm. We want to understand the features that best distinguish the differences between the noise, T1 and T2 signals. The features chosen to distinguish between T1 and T2 signals are based on time and frequency domains of the signal detected.

4.2.1 Distinguishing features between T1 and T2 time and frequency domain signals

The overall goal is to take recorded AE signals and be able to determine the crack length. Crack length can be determined through T1 signals (crack growth) since they change as the length of the crack changes. A typical T1 and T2 signal from the specimen with a crack length of ~7 mm can be seen in Figure 4.3. A table of significant differences between T1 and T2 signals can be found on Table 4.1. These features must be applied to a larger set of features to eliminate noise signals from the T1 and T2 signal clusters.

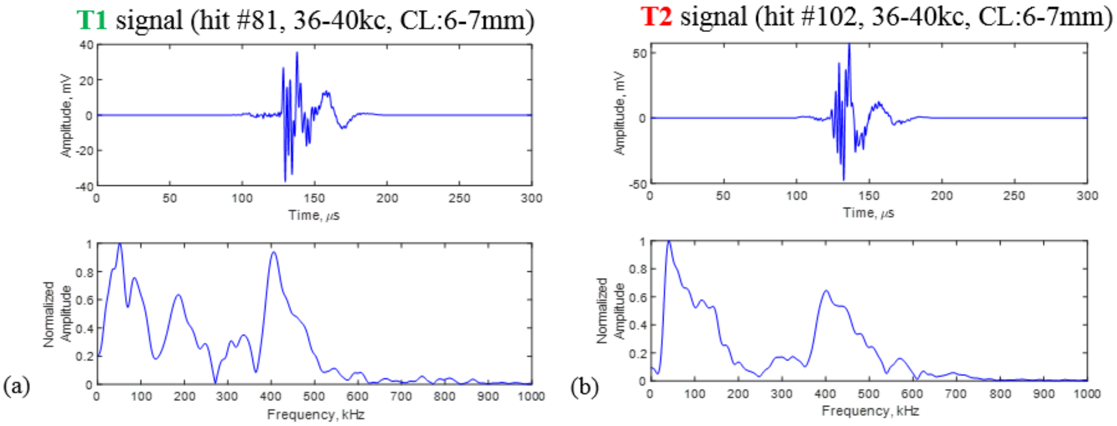

Figure 4.3 (a) Typical T1 signal at ~7 mm and (b) typical T2 signal at ~7 mm.

Table 4.1 Features that distinguish between T1 and T2 signals

Domain	**T1**	**T2**
Time domain	The first peak in the time domain is larger than the second peak	The first peak in the time domain is smaller than the second peak
	The time between each peak is about 2.4-2.6 μs	The time between each peak is about 2.2-2.3 μs
	About even A0 and S0 content	A0 content is dominant over S0 content
Frequency domain	Frequency peaks at ~200 kHz and ~300 kHz	No frequency peaks at ~200 kHz and ~300 kHz
	Frequency drop at ~120 kHz	No frequency drop at ~120 kHz

4.2.2 Features distinguishing T1, T2 and noise AE signals

Since we are trying to find crack length based on the recorded signals, we want to favor the features to T1 signals. If the feature is not favored towards a T1 signal, its value is set equal to zero. A list of fourteen features used to distinguish between a T1, T2 and noise signal are found in the following bullets.

Time domain features:

- **F1:** The number of peaks the signal has with a minimum peak prominence of 6 mV and 25% of the maximum amplitude between 120 and 145 μs must be $3 < n < 9$.

- **F2:** If F1 is true, the difference in time from the first to the second peak must be $2.3 < t < 2.8$ μs and the minimum value between the first and second peak must drop below -5 mV.

F2 helps to separate T1 and T2 signals because the difference in time between first and second peak is less than 2.4 μs for T2 signals. It also helps to distinguish between crack and non-crack-related signals because non-crack-related signals typically don't have a valley less than -5 mV when F1 criteria is true.

- **F3:** If F2 is true, then the ratio of the first to second peak must be greater than 1.

This helps to separate T1 and T2 signals because the ratio of the first to the second peak is less than 1 for T2 signals.

- **F4**: If F1 is true, the ratio of the S0 mode to the A0 mode is evaluated.

<u>Frequency domain features:</u>

- **F5:** The mean of the values between 0-150 kHz and the mean of the values between 360-600 kHz must add up to be greater than 0.6.
- **F6:** The mean of the values between 150-270 kHz and the mean of the values between 270-360 kHz must add up to be greater than 0.4.

This helps to distinguish between T1 and T2 signals because T2 tends to have less frequency content in the 150-360 kHz range.

- **F7:** The maximum value of the amplitude for 150-270 kHz must be greater than 0.2 for 170-225 kHz (and be between 175.5-220 kHz), greater than 0.15 for 270-360 kHz, and greater than 0.5 for 360-600 kHz.

This helps to distinguish between T1 and T2 signals because T2 tends to have lower frequency content in the 150-360 kHz range.

- **F8:** The maximum value of the amplitude for 270-360 kHz must be greater than 0.2 for 170-225 kHz (and be between 175.5-220 kHz), greater than 0.15 for 270-360 kHz, and greater than 0.5 for 360-600 kHz.

This helps to distinguish between T1 and T2 signals because T2 tends to have lower frequency content in the 150-360 kHz range.

- **F9:** The maximum value of the amplitude for 170-225 kHz must be greater than 0.2 for 170-225 kHz (and be between 175.5-220 kHz), greater than 0.15 for 270-360 kHz, and greater than 0.5 for 360-600 kHz.

This helps to distinguish between T1 and T2 signals because T2 tends to have lower frequency content in the 150-360 kHz range.

- **F10:** The mean from 0-1,000 kHz must be greater than 0.14.
- **F11:** The ratio of the sum of the maximum amplitudes for 0-150 kHz and 360-600 kHz divided by the sum of the maximum amplitudes for 150-270 kHz and 270-360 kHz is less than 3.5, greater than 0.25 for 150-270 kHz, greater than 0.15 for 270-360 kHz and greater than 0.5 for 360-600 kHz.
- **F12:** There must be a valley between 75-175 kHz that drops below 0.38.

This helps to distinguish T1 and T2 signals because T2 doesn’t drop below 0.38 in this frequency range.

- **F13:** The number of peaks between 150-270 kHz with a minimum peak prominence of 0.06 that are greater than 0.2 must be between 0 < n < 4.

This helps to distinguish between T1 and T2 signals because T2 doesn’t have a peak in this frequency range.

- **F14:** The number of peaks between 270-360 kHz with a minimum peak prominence of 0.06 that are greater than 0.2 must be between $0 < n < 4$.

There is no limit to the features that are used to separate signals into clusters. The chosen fourteen features are simply the features that were most useful in distinguishing the signals. There may be features that exist and are very good at distinguishing between the different types of signals but are unknown to us at the present time. There needs to be more features that will eventually take the T1 signals and separate them into sub clusters based on crack length.

Once the features have been determined, a table can be created where each column represents a feature and each row represents a signal or hit. An example of this table can be seen in Table 4.2. In aiding principal component analysis, all the values of the features were normalized. A set of hits that contain various T1, T2 and noise AE signals were selected in the 6-8 mm crack length range which fell in the 36-48 additional kcycle range. They are termed “additional” because they represent the number of cycles after crack initiation has occurred. As already mentioned in the bullets, there are certain features that help to distinguish between T1 and T2 signals. The supporting features include F2, F3, F6, F7, F8, F9, F12, F13 and F14.

To better understand how each feature helps to separate the hits into T1, T2 and noise signals, a parallel coordinate plot was created. A parallel coordinates plot for all data as well as the median of the data can be seen in Figure 4.4. In Figure 4.4a, each line signifies a hit signal and the coordinate value comes from the normalized value from Table 4.2. In Figure 4.4b the dashed lines signify 25% and 75% of T1 and T2 signals. As you can see, all fourteen features help to separate T1 signals from noise signals. F1, F5 and F11 help to separate T2 signals from noise and F2, F3, F6, F7, F8, F9, F12, F13 and F14 are the features that help to separate T1 and T2 signals.

Table 4.2 Features and hit numbers table for T1, T2 and noise AE signals

Cycles	**Hit #**	**F1**	**F2**	**F3**	**F4**	**F5**	**…**	**F12**	**F13**	**F14**
36-40 kcycles CL=6-7 mm	1	0	0	0	0	0	…	0	0	0
	3	0	0	0	0	0		0	0	0
	5	0	0	0	0	0		0	0	0
	12	0	0	0	0	0		0	0	0
	72	0	0	0	0	0		0	0	0
	76 (**T1**)	0.7142	0.9637	0.9615	0.46984	0.7530		0.9105	1.000	1.000
	81 (**T1**)	0.7142	1.0000	0.9615	0.43514	0.8009		0.9234	1.000	1.000
	102 (**T2**)	0.7142	0	0	0.09559	0.8905		0	0	1.000
	5	0	0	0	0	0		0	0	0
	8	0	0	0	0	0		0	0	0
40-44 kcycles CL=7-7.4 mm	50	0	0	0	0	0	…	0	0	0
	70	0	0	0	0	0		0	0	0
	80	0	0	0	0	0		0	0	0
	90	0	0	0	0	0.6052		0.7168	0	0
	140 (**T1**)	0.7142	0.6519	1.0000	0.35920	0.7211		0.9692	1.000	1.000
	151 (**T1**)	0.7142	0.7138	1.0000	0.23707	0.7451		0.8707	1.000	1.000
	252 (**T1**)	0.7142	0.7131	0.9615	0.35782	0.6893		0.9980	1.000	1.000
44-48 kcycles CL=7.4-8 mm	69 (**T1**)	0.7142	0.8087	0.9615	0.28000	0.5078	…	0.9675	1.000	0
	132 (**T2**)	0.8571	0	0	0.07689	0.8648		0	0	1.000
	137 (**T2**)	1.0000	0	0	0.06080	0.8620		0	0	1.000
	152 (**T2**)	0.7142	0	0	0.07361	0.8575		0	0	0
	331 (**T2**)	0.8571	0	0	0.06409	0.8827		0	0	0
	342 (**T2**)	0.8571	0	0	0.03516	1.0000		0	0	0
	84	0	0	0	0	0		0	0	0
	92	0	0	0	0	0		0	0	0
	105	0	0	0	0	0		0	0	0
	106	0	0	0	0	0		0	0	0

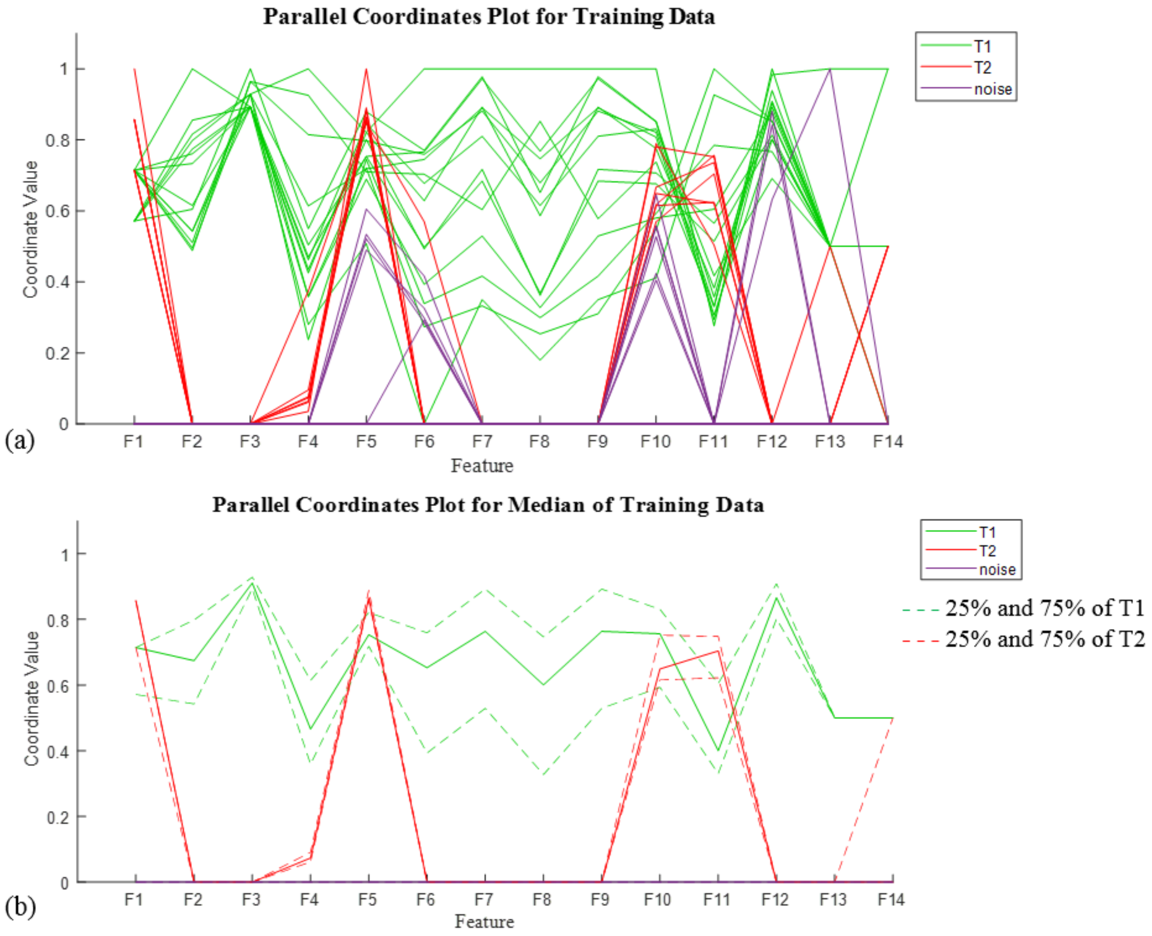

Figure 4.4 (a) Parallel coordinate plot to help distinguish features and (b) parallel coordinate plot to help distinguish the median of features.

4.3 PRINCIPAL COMPONENT ANALYSIS

Principal component analysis is done to reduce the dimensionality of the features. Once dimensionality is implemented, the PCA scores can be used as features as well. It is important to be able to visualize how all these features help to separate the hits into T1, T2 and noise signals with the use of a plot. The principal component plot as well as the Pareto chart can be seen in Figure 4.5. The green (T1), red (T2) and purple (noise) labels were manually placed into the chart to see the separation between the signals for 4-48 kcycles and a crack length of 3.5-8 mm. Hit number 13 is visually classified as T1 and seen as an outlier but for classification purposes, it will be labeled T2. In the T1 cluster in Figure 4.5a, you can see the hits were able to be further clustered into 3.5-6 mm and 6-8 mm. This is very promising for being able to determine crack length from an AE signal. In Figure 4.5b, you can see the Pareto chart, which shows that the first two principal components (as seen in Figure 4.5a) account for 89.13% of the variance and the first four principal components account for 95.65% of the variance.

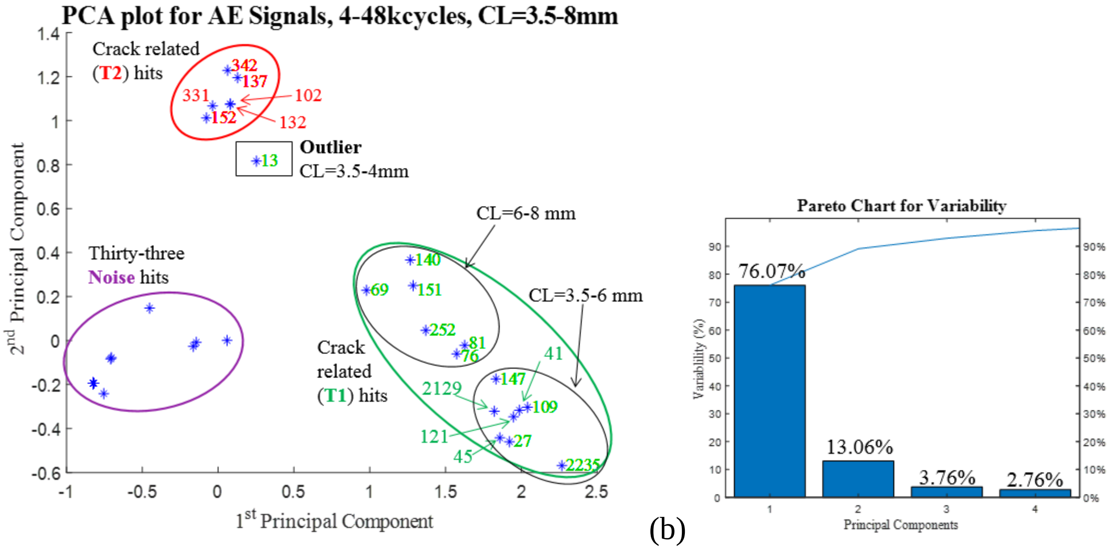

(a) (b)

Figure 4.5 (a) PCA plot for 4-48 kcycles and crack length of 3.5-8 mm and (b) Pareto chart describing the variance of the first four principal components.

As mentioned previously, clusters from PCA are manually separated, but it is important to find a method of automatic clustering when the signals are not as clear as the ones presented above. Two ways of clustering based on principal components are k-means clustering and hierarchical clustering. These clustering methods are not based on classification, so they do not describe the meanings of each cluster. *k*-means clustering is an iterative process and is based off the distance the hits are from each other. The results of *k*-means clustering can be seen in Figure 4.6 and as you can see, the results are very good. Hierarchical clustering is also based on distance between hits in the PCA plot, but it is presented in a tree. Hierarchical clustering is a good method to use when one is interested in sub-clustering. The results for hierarchical clustering of the crack-related hits can be seen in Figure 4.7. Aside from the outlier, the results are very good. The T1 and T2 hits were manually colored into green and red font, respectively.

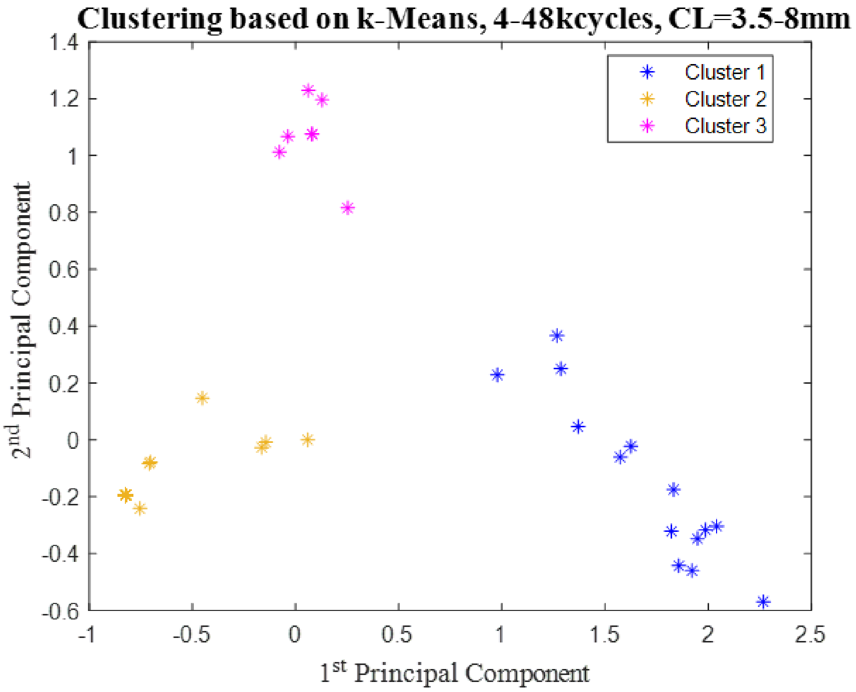

Figure 4.6 *k*-means clustering results based on first and second principal component.

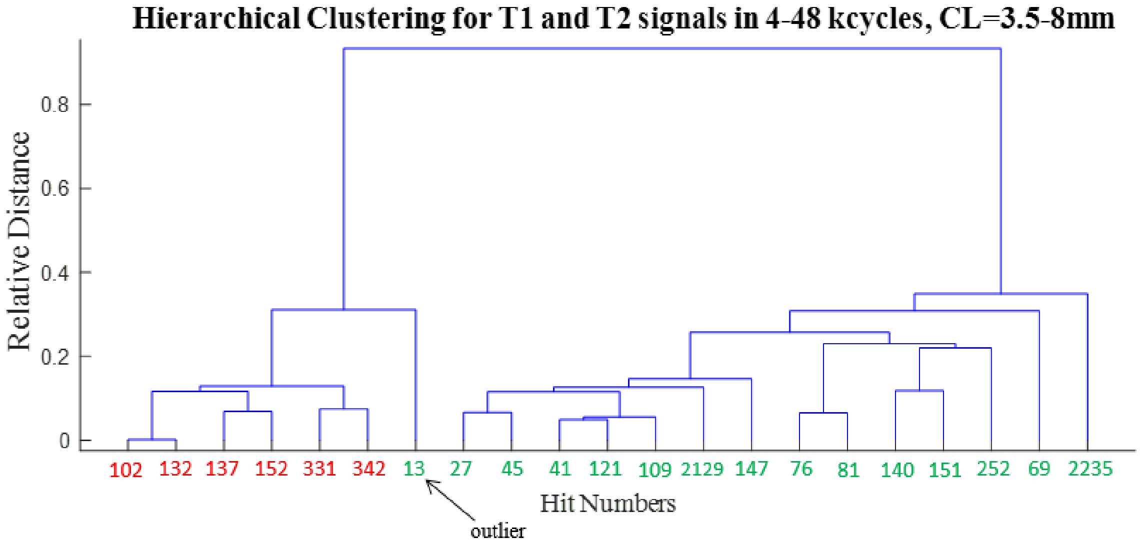

Figure 4.7 Hierarchical clustering of crack-related hits.

4.4 CLASSIFICATION MODELING

Now that the hits have been clustered, it is time to see if they can be classified into T1, T2 and noise signals. The classification methodology for machine learning purposes includes splitting the collected data into a training set and a testing set. A classification model can be trained by running the training data through the model. The model changes the weighting factors based on the training data to effectively classify the training data into their already-specified classification (noise, T1 or T2). Once you have a trained model, it is important to test how effective that model is when new data is introduced. The testing data is run through the trained classification model and the model's accuracy can be determined. There are many different types of classification models, but five specific ones were chosen to see how well the data could be classified. The five models tested are *k*-Nearest Neighbor (KNN), Decision Tree (DT), Naïve Bayes (NB), Discriminant Analysis (DA), and Support Vector Machine (SVM). With only 54 strong signals, it is predicted that the accuracy results for the classification models will be very high. The 54 hits were separated into 50% testing data and 50% training data. As predicted, KNN, DT, and SVM all had an accuracy of 100%. The scatter plot of the predicted cluster hits as well as the confusion matrix for the test data can be seen in Figure 4.8. Naïve Bayes and DA gave accuracy results of 84.26% and 96.06%, respectively, and their scatter plots and confusion matrices can be seen in Figure 4.9 and Figure 4.10, respectively. In Figure 4.9a and Figure 4.10a, there is a box around the hits that were misclassified. In Figure 4.9b, four noise signals were predicted as T1 and in Figure 4.10b, one noise signal was predicted as T2. A guide for the meaning of each symbol in the scatter plot can be seen in the following three bullets.

- The “*” indicates the training data that were visually clustered and used to train the classification model.
- The “+” indicates the testing data that were visually clustered and run through the trained classification model.
- The “o” indicates the predicted cluster that the testing data falls under based on the classification model.

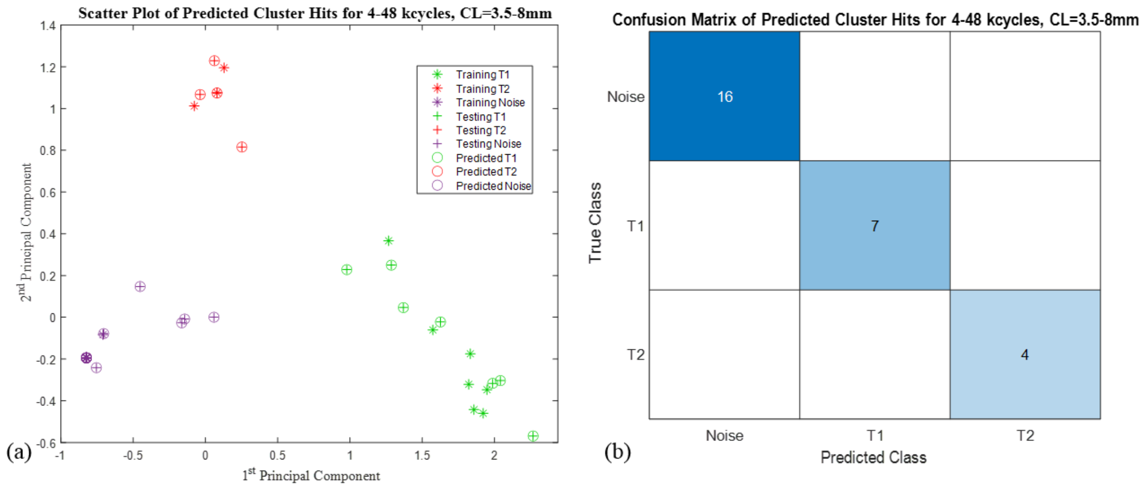

Figure 4.8 (a) Scatter plot, and (b) confusion matrix for test data with 100% classification accuracy for KNN, DT, and SVM models.

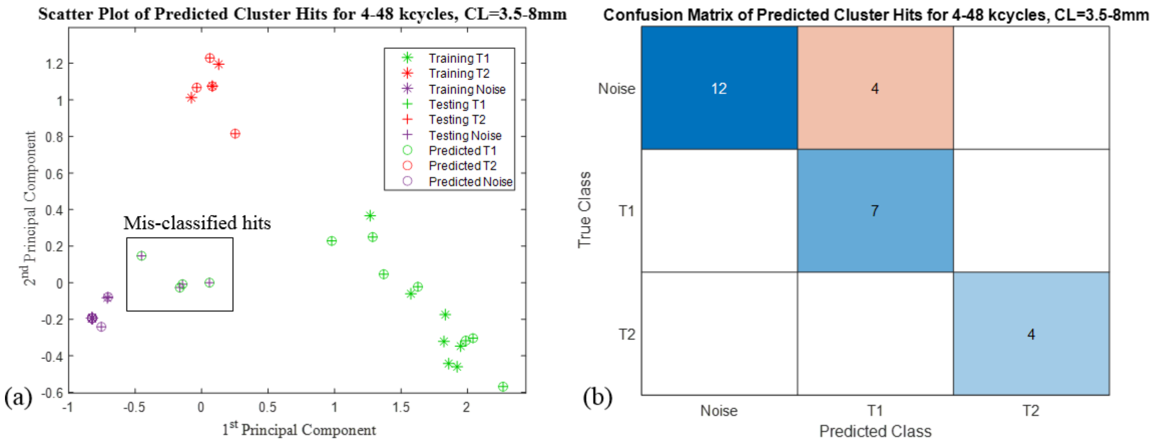

Figure 4.9 (a) Scatter plot, and (b) confusion matrix for test data with 84.26% classification accuracy for NB model.

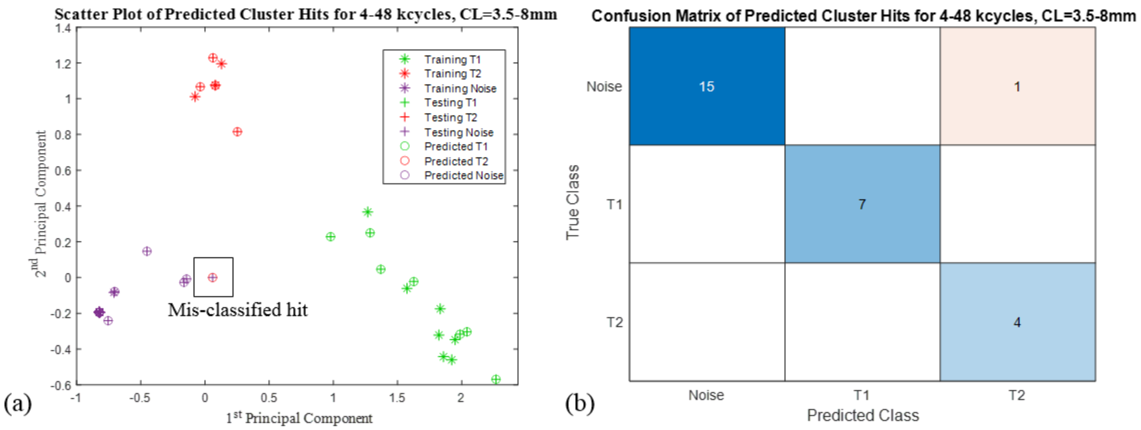

True Class	Noise	T1	T2
Noise	15		1
T1		7	
T2			4

Figure 4.10 (a) Scatter plot, and (b) confusion matrix for test data with 96.06% classification accuracy for DA model.

4.5 SUMMARY AND CONCLUSIONS

Subjective feature extraction to distinguish between the three different types of AE signals was performed and the highest accuracy of the classification models proved to be 100%. Hit number 13 was an outlier which caused some issues in distinguishing. In the future, there may be more than just one outlier, so an objective method for feature extraction is necessary. AE signals can change greatly from specimen to specimen. In the future, a larger dataset should be used to reduce the model from overfitting.

CHAPTER 5

DEEP LEARNING CLASSICAL AND CONVOLUTIONAL NEURAL NETWORKS

5.1 INTRODUCTION

Deep learning is the part of AI that introduces artificial neural networks to classify data. These neural networks can be supervised or unsupervised and provide a more objective method of learning. Rather than finding specific features that distinguish between outputs, neural networks take the raw data as its input. Neural networks are more advanced and complex than machine learning feature extraction and model classification techniques, but they have the capability to perform with higher accuracy and less error. In this chapter, sequence-based classical neural networks and pretrained convolutional neural networks are created and explored with experimental AE signals from an HCF crack growth specimen.

5.2 EXPERIMENTAL PROCEDURE AND DATA

The experimental data used for the neural networks is collected from the same specimen as seen in Chapter 4. A 101 mm by 304 mm thin aluminum specimen was initiated with a crack by drilling a 1 mm hole in the geometric center of the specimen and placing the specimen in an MTS machine with a maximum load of 14.05 kN and a minimum load of 1.405 kN with a loading frequency of 10 Hz. The crack initiated at 322 kcycles. Once the crack initiated, the specimen was removed from the MTS machine and was prepared with two PWAS and two S9225 sensors. The PWAS were located at 6 mm and 25 mm from the crack and the S9225 sensors were placed 6 mm and 25 mm away from the crack mirroring the PWAS. On the opposite side of the specimen, a strain gage was applied about 35 mm from the crack. The strain gage is used to monitor the load applied to the specimen. The specimen was equipped with a non-reflective boundary (NRB) to reduce reflection from the AE waves. The method of collecting the AE waves included the Mistras AE instrumentation connected to the sensors through a pre-amplifier. Periodically, to ensure the PWAS were well bonded, an impedance measurement was taken with an Omicron Lab EMIS instrument. To reduce the number of factors that affect how the AE signals look, the specimen is applied with a constant stress intensity factor (SIF). To do this the load is applied at 4 Hz starting at a load of 14.05 kN and periodically reduced to 6.29 kN using the Fedderson correction factor [41]. The crack grew from ~3.5 to ~9.4 mm in an additional 188 kcycles.

The data used for analysis consisted of 184 waveforms captured from PWAS 2. This dataset includes all 54 hits used in Chapter 4. An additional 130 hits were added to the dataset because neural networks give higher accuracies with larger amounts of data. Due to the need for a larger amount of dataset, some hits were included that were not clear whether it originated from crack growth or crack rubbing and clapping. As a result, the neural networks were trained to classify a signal as crack-related or noise.

5.3 CLASSICAL NEURAL NETWORK: LSTM

Long Short-Term Memory (LSTM) neural network is a type of classical neural network where the input is an ordered sequence where information from earlier in the sequence may be important. Rather than the input being an image, the input is a signal vector. For our case, we have used the frequency domain signal vector as the input. Within the node calculation, there is an internal state. The node uses this internal state as a working memory space, which means information can be stored or retrieved over many time steps. Once the sequence has been outputted, it has a recurrent neural network which reuses the output from a previous step as an input for the next step. LSTM's do not have readily available pre-trained networks, so they are much more sensitive to input data. The more data they have to train with, the better the outcome will be.

For classification purposes like this, it is best to have at least 150 data points for each cluster, but we do not have enough data for that. The dataset used here consisted of 184 frequency domain signal sequences containing 64 crack-related signals and 66 noise signals. The data was split to have a training set (88% of the data) and a testing set (12% of the data). The LSTM was trained with the training data and took 1 hour and 13 minutes. A plot of the accuracy and loss during the training process can be seen in Figure 5.1. At the end of the training process, the accuracy came out to be 94.53% with a loss of 0.1432. When the testing data (12% of the signals) was run through the trained model, the accuracy came out to be 95.45%. A confusion matrix of the classified testing data can be seen in

Figure 5.2. In this figure, you can see that the model misclassified only one hit which is very good for a model trained with such a small amount of data.

5.4 CONVOLUTIONAL NEURAL NETWORKS

The deep learning process we are using here is a convolutional neural network. Neural networks are made up of many layers or steps that come together to form the process of the network. There are many different networks with many different layers. The dataset we are using includes a '.jpg' of the Choi William transform for each signal. The transform is used as the image because it allows for intensities of both the time and frequency domain of a signal. The Choi William transform is a type of wavelet transform that intensifies the Lamb wave modes and adds more detail than that of a wavelet transform [42]. Since we are using images as the input, the network is called a convolutional neural network. Examples of some Choi William transforms can be seen in Figure 5.3. In the figure, you can see a significant difference between the crack-related signals and the noise signals. Since neural networks are very complex and typically take months to create for a trained professional, a pretrained convolutional neural network was used, called AlexNet. The full tree of the layers of AlexNet can be seen in Figure 5.4. There is a total of 25 layers and for AlexNet, it is required that the input layer have a size of $227 \times 227 \times 3$ RGB images. As you can see, some of the layers are repeated because convolutional layers can have many different types of filters. When an image goes through a convolutional or pooling layer, it typically reduces the pixel size of the image. The size of the image is calculated from the input image size, filter/pooling size, padding and stride size as seen in the equation at the bottom of Figure 5.4. Transfer learning is the term used when a pretrained network is modified. Transfer learning was used to update the last fully connected layer (fc8) to have an output of two nodes (one for crack-related and one for noise). An example of how the convolutional layer works can be seen in Figure 5.5. Figure 5.5a is a montage of all 96 filters for the first convolutional layer in AlexNet. Figure 5.5b is filter 79. As you can see, filter 79 will mainly activate the green in the figure. Inputting hit number 27 (4-8 kcycles, 3.5-4 mm) as seen in Figure 5.5c, filter 79 will activate only the green in the figure to result in a black and white photo as seen in Figure 5.5d. This convolution layer example also shows how the image size reduction is performed as well. Refer to the equation in Figure 5.4 to determine the output size of the filtered image in Figure 5.5d.

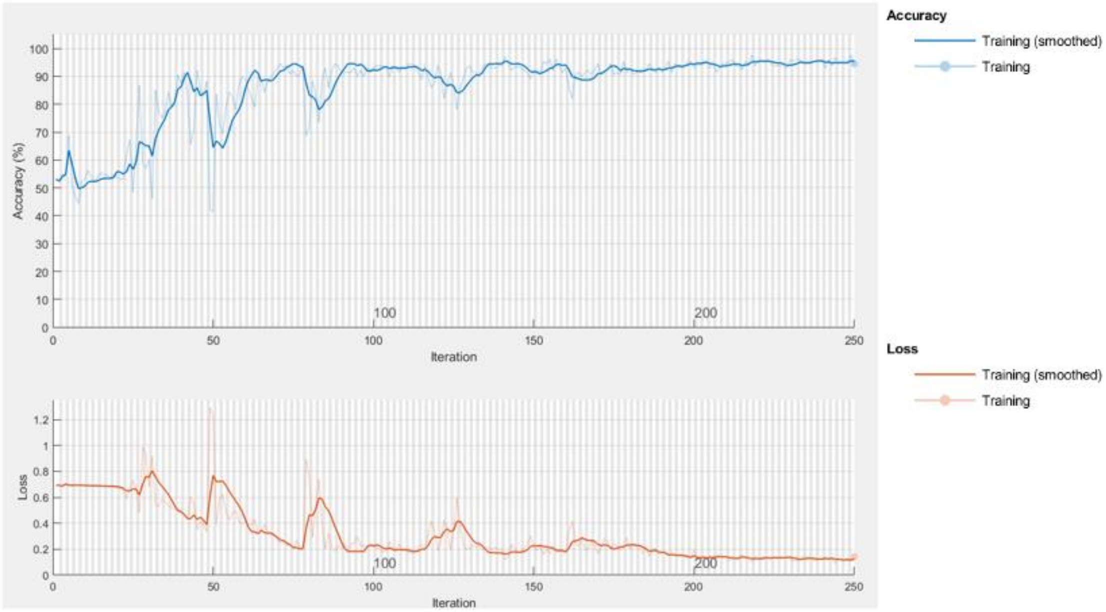

Figure 5.1 Training process for frequency domain LSTM network.

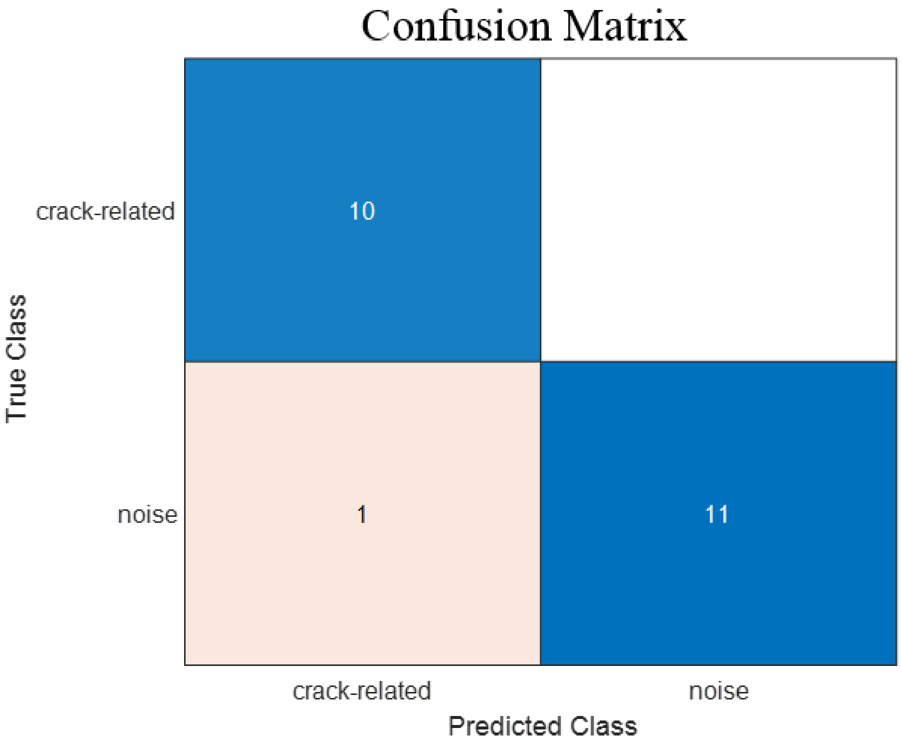

Figure 5.2 Confusion matrix for test data run through trained frequency domain LSTM network.

This dataset included 184 strong and weak signals which includes 64 crack-related signals and 66 noise signals. Since weak signals are included in this dataset, we will attempt to classify the signals into crack-related and noise related. The dataset was split up into a training set (70% of the signals), a validation set (10% of the signals), and a testing set (20% of the signals). The testing and validation set was run through the pretrained network. The accuracy and loss were evaluated throughout the training process and the training graphs can be seen in Figure 5.6. The accuracy is the percentage of training images that the network classified correctly during an iteration. It does not measure how confident the network is about each prediction. The loss is a measure of how far from a perfect prediction the network was, totaled over the set of either training or validation images. The accuracy and validation accuracy reached 100%, the loss reached 4.532e-5 and the validation loss 6.971e-6. The test data was run through the trained neural network and 100% accuracy was reached meaning all the testing data was categorized correctly. The confusion matrix can be seen in Figure 5.7.

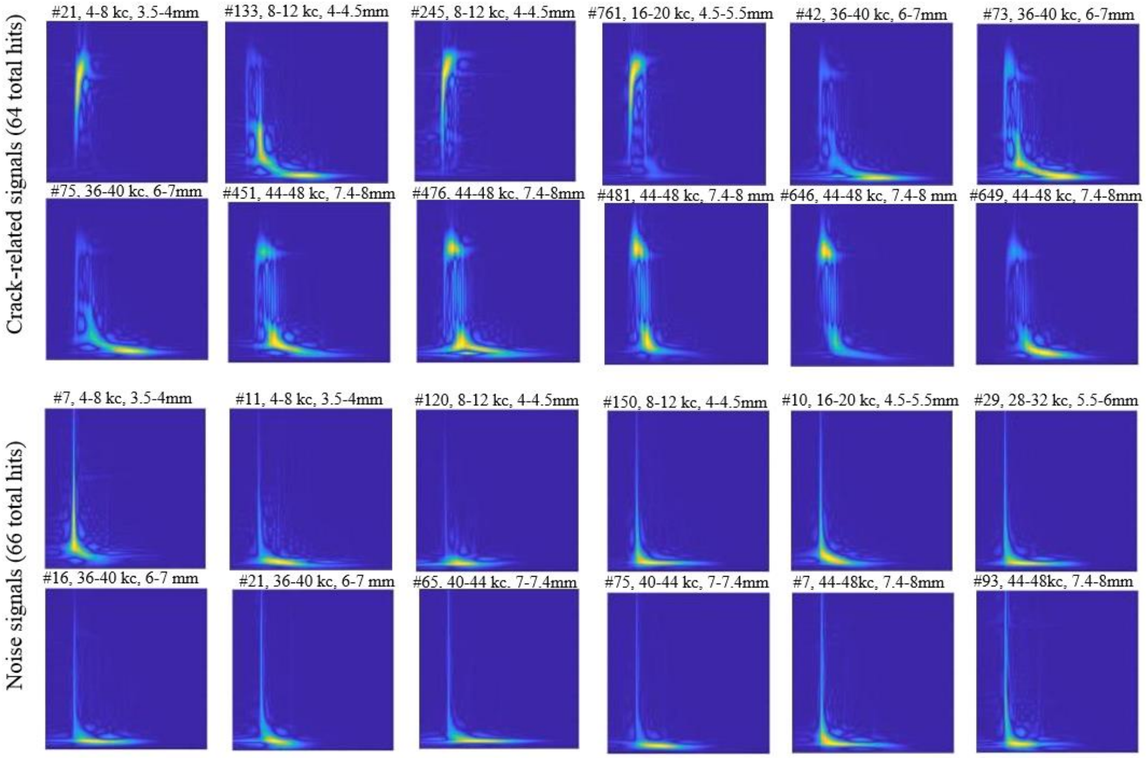

Figure 5.3 Example Choi William transforms for crack-related and noise AE signals.

$$Output\ Image\ Size = \frac{input\ size - (filter\ or\ pooling\ size) + 2(padding) + stride}{stride}$$

Figure 5.4 Pretrained convolutional neural network called AlexNet.

5.5 SUMMARY AND CONCLUSIONS

In summary, deep learning artificial intelligence techniques were explored to classify 184 AE signals into crack-related and noise. An LSTM classical neural network was trained with the frequency domain of the signals. The results had good accuracy, but the model took over an hour to train, so it may not be an efficient technique to use once more AE signals are introduced. A pretrained convolutional neural network called AlexNet was used to train the AE signals. The accuracy was very good with a very small loss. The network training time was just over three minutes which makes it a more efficient deep learning technique than the LSTM. Since we used a pretrained convolutional network (AlexNet), less data is needed to continue to see good results.

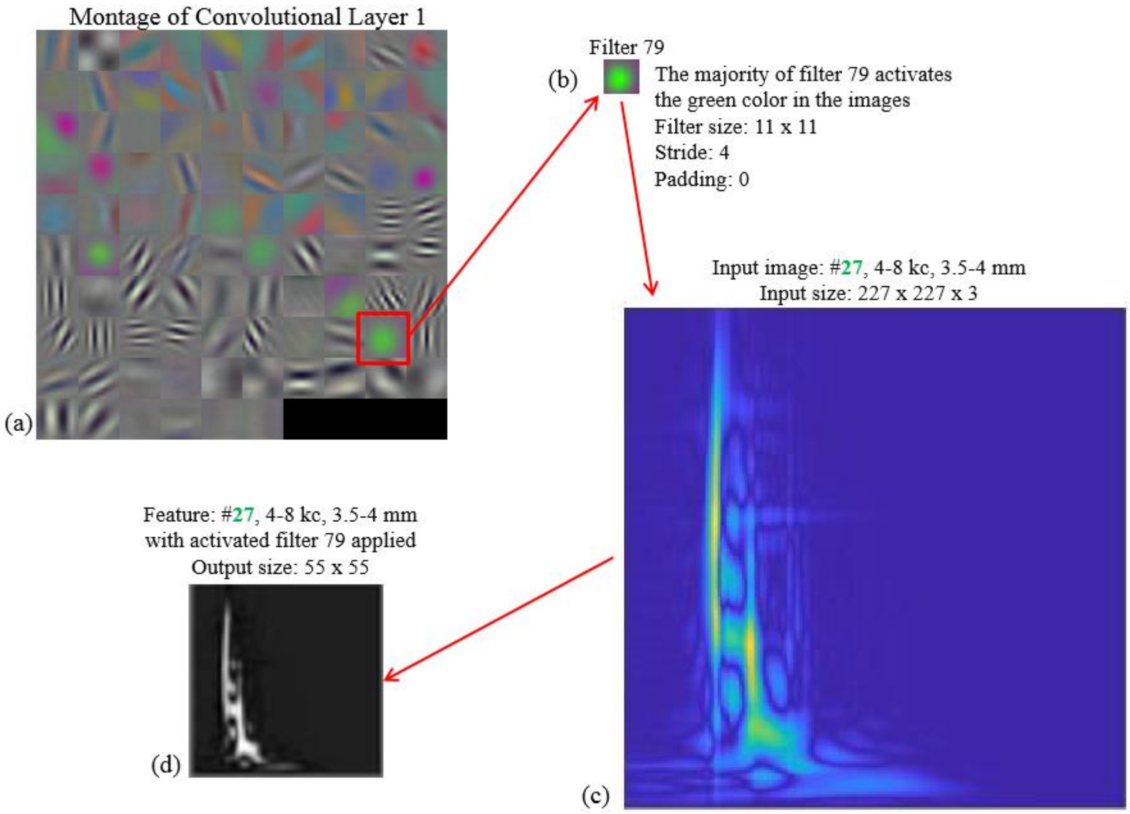

Figure 5.5 (a) Montage of convolutional layer 1 from pretrained AlexNet neural network, (b) a close up of green-activating filter 79, (c) input of hit #27, and (d) hit #27 activated with filter 79.

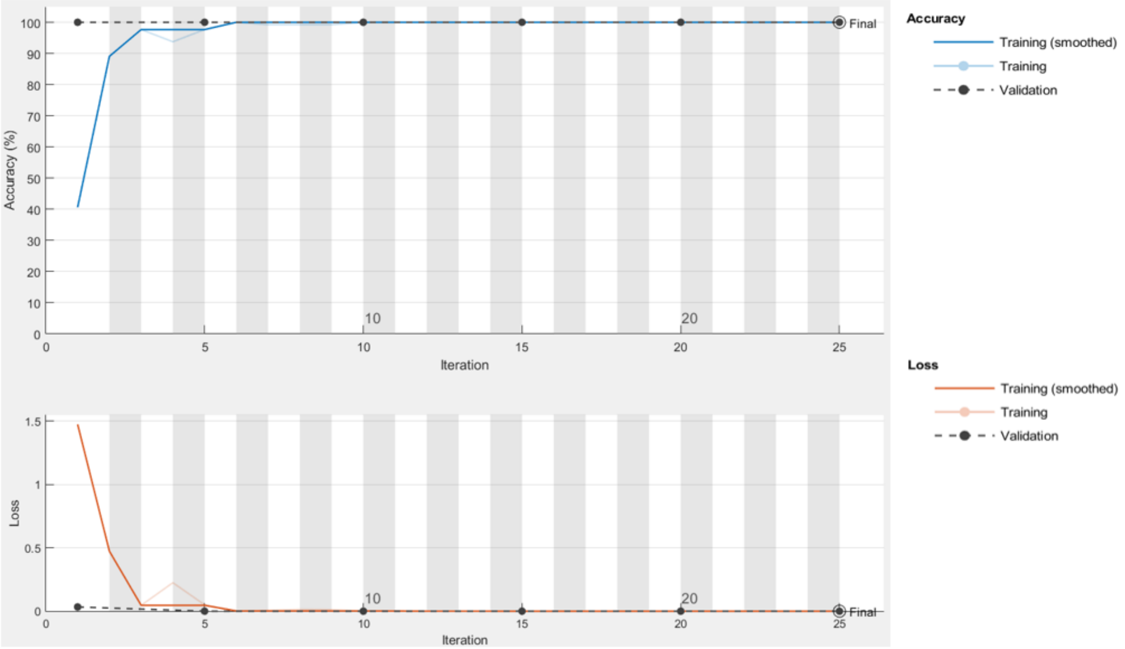

Figure 5.6 Accuracy and loss graphs for training convolutional neural.

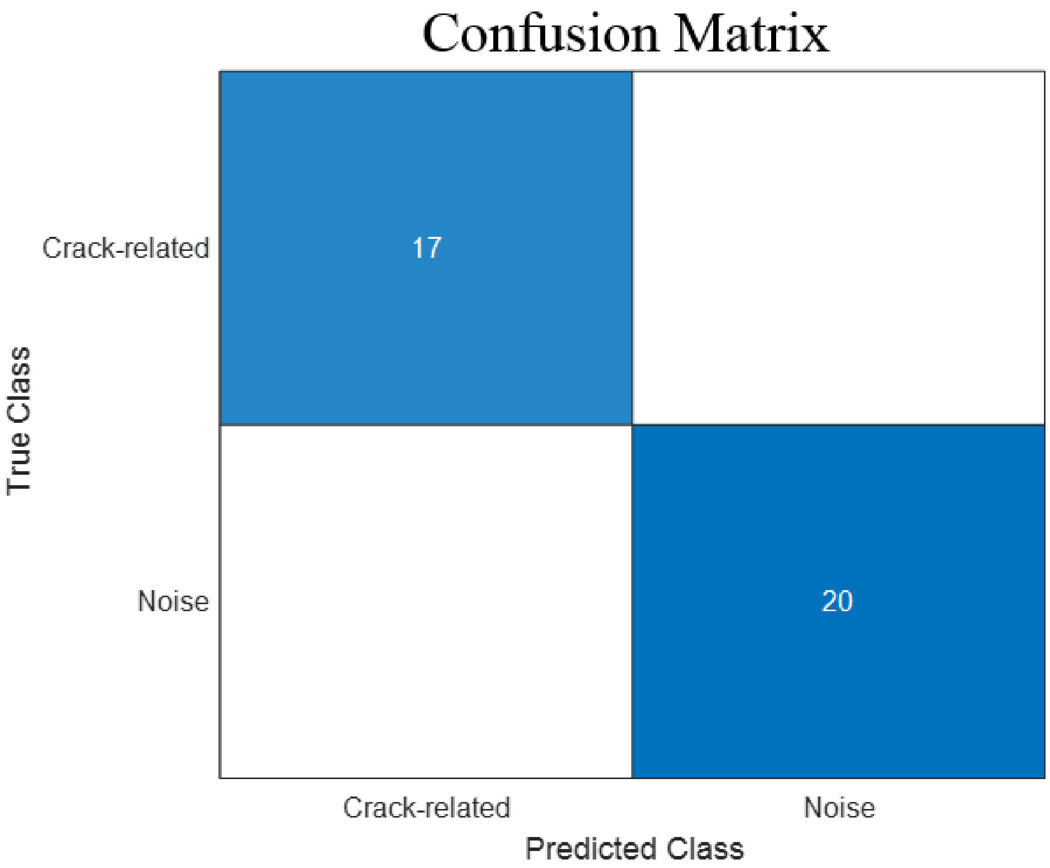

Figure 5.7 Confusion matrix of the testing data run through the trained network.

CHAPTER 6

SUMMARY AND CONCLUSIONS

The work completed for this thesis enhances the understanding and knowledge of damage detection through the results from the active PWAS sensing capabilities, experimental methodology, and artificial intelligence techniques.

The basic understanding of the constitutive equations was introduced in Chapter 1. Through the active sensing of the PWAS, the electro-mechanical impedance and admittance was reviewed for sensor debonding as well as damage detection. Although results for measuring damage did not show a clear trend, the imaginary part of the admittance resulted in a clear correlation between the amount of debonding and the slope of the line in the frequency vs. admittance plot. As the sensor debonded, the slope of the line increased and contained less noise. In conclusion, sensor debonding can be quantifiably measured through the slope of the active sensing by means of the real part of the admittance.

Chapter 2 provides the knowledge for proper methodology for experimental fatigue crack growth monitoring as well as repeatability of AE signal signatures. Section 2.4 clearly outlines the methodology needed to properly and confidently monitor crack growth. The monitoring process includes the use of AEwin to gather AE signal hits, impedance analyzer to monitor the bonding of the PWAS, a magnifying camera to capture photos and videos of the crack tip, an eddy current instrument to measure crack length, and a bridge completion as well as a strain gauge to measure the load being applied. Change in loading frequency affected the percentage of the maximum load the hit occurred at. As the loading frequency decreased, the load at which the signal occurred increased. When discussing repeatability of AE signals, it appears that the signals in Group A and Group G reviewed from Y. Bhuiyan [19] in section 2.2.2 were similar to my AE signals in Group 1 and Group 2 (section 2.5), respectively. This proves that AE signals can be repeated in the case of two different LCF specimen.

Artificial intelligence provided us with a platform for allowing a computer to classify AE signals in place of human intelligence. The machine learning results provide us with the ability to separate signals into crack growth, crack rubbing and noise with the use of feature extraction and classification models. The deep learning results provide us with the ability to separate signals into crack-related and noise. The models and networks used gave great accuracy for classifying AE signals. These AI techniques are part of the transformation from research to industry applications.

6.1 FUTURE WORK

6.1.1 Datasets used for artificial intelligence purposes

Artificial intelligence works best with large datasets. We wish to continue artificial intelligence studies using the experimental data we have already collected from the SIF-controlled HCF specimen data. In the future, we hope to validate our trained classification models, convolutional neural network and classical neural network with other datasets. There are three main datasets we hope to use in the future. The first future dataset comes from AE signals that have already been collected from LCF and HCF specimen. The second dataset can be created from the future laboratory LCF and HCF experimental AE signals. The third dataset comes from simulated AE signals that should be explored in the future. With these datasets, we hope to complete the future work as explained in the following sections.

6.1.2 Machine learning classification models

In the future, we would like to run more data through the already trained classification model as seen in Chapter 4. Due to using strong (high amplitude) AE signals to train the model and the resulting high accuracy, the model may be overfitting. Since a typical dataset includes more than just high amplitude AE signals, the model should be re-trained with more data to include outliers. Since it is sometimes difficult to subjectively determine if a signal is T1 or T2, the model should be trained to have only two output classes, crack-related and noise related. This new classification model is to be trained and tested with more data.

Once this model is trained and test signals have proven it is possible to distinguish between crack-related and noise signals with good accuracy, we want to be able to distinguish the crack-related signals between crack-growth (T1) and crack rubbing and clapping (T2) signals. This may be difficult to do with the features we have subjectively created since they were designed to distinguish between only strong T1 and T2 signals. These features may not apply to new datasets that are created from new specimen that are subjected to different environmental conditions as well as human error. This is where unsupervised learning plays a role in feature extraction. There may be some feature or set of features that all AE signals have no matter what conditions are applied that cannot be seen by the human eye. In the future, features should be created based on statistical observations of the time and frequency domain signals to objectively extract features. Some statistical observations include mean, standard deviation, rise time, peak amplitude, etc.

Through PCA, these statistical features may create natural clusters for the signals to help distinguish between crack growth and crack rubbing and clapping.

6.1.3 New convolutional neural networks

Since we are using a well-established pre-trained network to classify our Choi William transform images, the results have been very good. In the future, the objectively clustered AE signals from section 6.1.2 should be used to distinguish between crack growth, crack rubbing and clapping and noise signals using a new trained convolutional neural network.

Convolutional neural networks allow inputs from multiple channels to help classify AE signals. In the future, data from the PWAS that is 5 mm from the crack in addition to the PWAS that is 25 mm away from the crack should be used to help identify crack growth and crack rubbing and clapping signals.

6.1.4 New LSTM classical neural networks

Since the LSTM network is created from scratch and not a pre-trained network, it is much more sensitive to the inputted signal vector. Therefore, LSTM networks must be trained with a very large dataset. In the future, another frequency domain LSTM should be created and trained to accurately classify signals into crack growth, crack rubbing and clapping and noise signals.

LSTM classical neural networks allow inputs from multiple channels to help classify AE signals. In the future, the data from the PWAS that is 5 mm and 25 mm from the crack should be used to help identify crack growth and crack rubbing and clapping signals from the time and frequency domains.

6.1.5 Regression models

A regression model is typically used when you are trying to determine a continuous variable rather than a discrete one. The crack length is the first continuous variable in question. In the future, a regression model should be used to determine the crack length from crack growth AE signals. Regression models can be used as a classification model or as a neural network. Using the classification model with extracted features from crack growth signals can be used as the input to determine the crack length. Choi William transforms from crack growth AE signal images can also be used as the input to convolutional neural networks to determine crack length. Comparing both networks of different inputs will determine which method has the highest accuracy.

Crack location is the second continuous variable that can be studied with the help of a regression model. A crack-related AE signal changes as it moves further away from its origin. In the future, the data collected from experiments with multiple PWAS sensors at various distances from the crack should be used for analysis. Features could be objectively extracted and used to determine signal distance from the crack. From there, use those features as the input to a regression classification model. The results to the regression convolutional neural network can be compared to the Choi William transform input results.

6.2 MAJOR CONTRIBUTIONS

The goal of this research is to identify crack damage in an aerospace structure and to find its corresponding crack length based on ultrasonic Lamb waves. Many contributions have been outlined in this thesis that help us move towards our goals. The major contributions of this research are outlined in the following paragraphs.

The details and results outlined in Chapter 1 of this thesis prove that the slope of the imaginary part of the impedance provides us with a way to accurately measure how well a PWAS is bonded to a structure. Not only does the slope give the PWAS bonding quality but the amplitude of the resonances also indicates how well the PWAS is bonded to the structure. The larger the amplitude of the resonances, the better the bonding. This is one way that experimental methodology has been improved.

Chapter 2 provides a detailed methodology that improves monitoring crack growth. When growing a fatigue crack, it is important to note when the crack grows and how much it grows. This data is gathered from a camera capturing pictures and videos from the crack tip as well as periodic eddy current measurements of the crack. Chapter 2 also provides confidence in the repeatability of AE signal signatures from LCF experimentation.

One of the largest contributions to this research is the application of artificial intelligence. With the help of artificial intelligence, AE signals can be classified based on reliable models that confidently separate different types of signals. In Chapter 4, feature extraction was introduced which separates signals based on time and frequency domain features. These features were then used to train classification models that help classify the different types of signals. In Chapter 5, neural networks were used to train different types of networks. The LSTM provided us with a network that classified signals based on their frequency domain vectors. The pre-trained convolutional neural network, called AlexNet, provided us with a network that classified signals based on their Choi William transforms. These contributions help to classify signals faster and with less human error.

REFERENCES

[1] Y. Bhuiyan, B. Lin, V. Giurgiutiu, (2017) "Acoustic Emission sensor effect and waveform evolution during fatigue crack growth in thin metallic plates," *Journal of Intelligent Material Systems and Structures,* 1-10.

[2] Y. Bhuiyan, B. Lin, V. Giurgiutiu, (2019) "Characterization of piezoelectric wafer active sensor for acoustic emission sensing," *Ultrasonics* 92, pp. 35-49.

[3] M. Kaphle, A. Tan, D.P. Thambiratnam, T. Chan, (2010) *Analysis of acoustic emission data for structural health monitoring applications,* 6th Australian Congress on Applied Mechanics (ACAM 6), Perth, Western Australia.

[4] G. Wild, S. Hinckley, (2007) "Fiber Bragg Grating Sensors for Acoustic Emission and Transmission Detection Applied to Robotic NDE in Structural Health Monitoring," *IEEE Sensors Applications Symposium,* 6-8 Feb. 2007.

[5] L. Yu, Z. Tian, (2013) "Lamb wave Structural Health Monitoring Using a Hybrid PZT-Laser Vibrometer Approach," *Structural Health Monitoring,* 12(5-6), pp. 469-483.

[6] G. Park, C.R. Farrar, A.C. Rutherford, A.N. Robertson, (2006) "Piezoelectric Active Sensor Self-Diagnostics using Electrical Admittance Measurements," *ASME Journal of Vibration and Acoustics,* 128(4), 469-476.

[7] G. Park, C.R. Farrar, F.L. Scalea, S. Coccia, (2006) "Performance Assessment and Validation of Piezoelectric Active-Sensors in Structural Health Monitoring," *Smart Materials and Structures,* Vol. 15 (6), pp. 1673-1683.

[8] V. Giurgiutiu, A. Zagrai, (2005) "Damage Detection in Thin Plates and Aerospace Structures with the Electro-Mechanical Impedance Method," *Sage Publications,* Vol. 4(2): 0099-20.

[9] W. Na, F. Baek, (2018) "A Review of the Piezoelectric Electromechanical Impedance Based Structural Health Monitoring Technique for Engineering Structures," *Sensors,* Vol. 18, issue 5.

[10] C.R. Farrar, K. Worden, (2007) "An introduction to structural health monitoring," *Royal Society,* Vol. 365, Issue 1851.

[11] M. Mitra, S. Gopalakrishnan, (2016) "Guided wave based structural health monitoring," *Smart Materials and Structures,* Vol. 25, No. 5.

[12] F. Amerini, M. Meo, (2011) "Structural health monitoring of bolted joints using linear and nonlinear acoustic/ultrasound methods," *Structural Health Monitoring,* Vol. 10, issue 6, pp. 659-672.

[13] H. Mei, A. Migot, M.F. Haider, R. Joseph, Y. Bhuiyan, V. Giurgiutiu, (2019) "Vibration-Based In-Situ Detection and Quantification of Delamination in Composite Plates," *MDPI-Sensors,* 19, 1734.

[14] M.F. Haider, A. Migot, Y. Bhuiyan, V. Giurgiutiu, (2018) "Experimental Investigation of Impact Localization in Composite Plate Using Newly Developed Imaging Method," *MDPI-Inventions,* 3, 59.

[15] T.M. Roberts, M. Talebzadeh, (2003) "Acoustic emission monitoring of fatigue crack propagation," *Elsevier,* Journal of Constructional Steel Research, vol. 59, pp. 695-712.

[16] N. Nemati, B. Metrovich, A. Nanni, (2015) "Acoustic Emission Assessment of Through-Thickness Fatigue Crack Growth in Steel Members," *Advances in Structural Engineering,* vol. 18, No. 2.

[17] B.H. Han, D.J. Yoon, Y.H. Huh, (2014) "Damage assessment of wind turbine blade under static loading test using acoustic emission," Journal of Intelligent Material Systems and Structures, Vol. 25, issue 5, pp. 621-630.

[18] V. Giurgiutiu, (2014) *Structural health monitoring with piezoelectric wafer active sensors,* 2nd Edition. Waltham, MA, USA: Elsevier Academic Press.

[19] Y. Bhuiyan, V. Giurgiutiu, (2017) "The signatures of acoustic emission waveforms from fatigue crack advancing in thin metallic plates," *Smart Materials and Structures,* Vol. 27, pp. 15.

[20] A. Terchi, Y. H. J. Au, (2001) "Acoustic emission signal processing," *Measurement + Control,* Vol. 43, October 2001, pp. 240-244.

[21] F. Mustapha, G. Manson, S. G. Pierce, K. Worden, (2005) "Structural health monitoring of an annular component using a statistical approach," *Strain: An International Journal for Experimental Mechanics,* Vol. 41 (3), pp. 117-127.

[22] R. Joseph, Y. Bhuyian, V. Giurgiutiu, (2019) "Acoustic emission from vibration of cracked sheet-metal samples," *Engineering Fracture Mechanics,* Vol. 217, August 2019, 106544.

[23] A. K. Maji, D. Satpathi, T. Kratochvil, (1997) "Acoustic emission source location using Lamb wave modes," *American Society of Civil Engineers,* Vol. 123 (2), February 1997.

[24] Y. Zhang, W. Lu, F. Chu, (2017) "Planet gear fault localization for wind turbine gearbox using acoustic emission signals," *Renewable Energy,* Vol. 109, pp. 449-460.

[25] Dictionary.com, Artifcial Intelligence, Accessed April 23rd, 2020, https://www.dictionary.com/browse/artificial-intelligence?s=t.

[26] Smarsly, K.; Lehner, K.; Hartmann, D. (2007) "Structural Health Monitoring based on Artificial Intelligence Techniques in Civil Engineering." *American Society of Civil Engineers*, 2007, DOI: 10.1061/40937(261)14.

[27] Manson, G. & Worden. K (2003) "Experimental validation of a structural health monitoring methodology: Part III. Damage location of an aircraft wing," *Journal of Sound and Vibration,* Vol. 259, No. 2, pp. 365-385, 2003.

[28] Elforjani, M.; & Shanbr, S. (2018) "Prognosis of Bearing Acoustic Emission Signals Using Supervised Machine Learning," *IEEE Transactions on Industrial Electronics,* 65(7), 5864–5871. doi:10.1109/tie.2017.2767551.

[29] Ahn, B.; Kim, J.; Choi, B. (2019) "Artificial intelligence-based machine learning considering flow and temperature of the pipeline for leak early detection using acoustic emission," *Engineering Fracture Mechanics,* Vol. 210, 1 April 2019, pp. 381-392.

[30] Nasir, V.; Cool, J.; Sassani, F. (2019) "Acoustic emission monitoring of sawing process: artificial intelligence approach for optimal sensory feature selection," The *International Journal of Advanced Manufacturing Technology,* Vol. 102, pp. 4179-4197, 07 March 2019.

[31] Jahanbakhshi, A.; Ghamari, B.; & Heidarbeigi, K. (2017) "Assessing acoustic emission in 1055I John Deere combine harvester using statistical and artificial intelligence methods," *International Journal of Vehicle Noise and Vibration,* Vol. 13, No. 2, 105. doi:10.1504/ijvnv.2017.087906

[32] G. Manson, K. Worden, D. Allman, (2003) "Experimental validation of a structural health monitoring methodology: Part III. Damage location on an aircraft wing," *Journal of Sound and Vibration,* Vol. 259, Issue 2, pp. 365-385.

[33] Y. L. Zhou, N. M. M. Maia, R. P. C. Sampaio, M. A. Wahab, (2016) "Structural damage detection using transmissibility together with hierarchical clustering analysis and similarity measure," *Structural Health Monitoring*, Vol. 16, Issue 6, pp. 711-731.

[34] A. Likas, N. Vlassis, J. J. Verbeek, (2002) "The global k-means clustering algorithm," *Pattern Recognition*, Vol. 36, pp. 451-461.

[35] D. J. C. MacKay, (2003) *Information Theory, Inference, and Learning Algorithms*, Cambrige University Press, ISBN-13:9780521642989, pp. 248-288, 2003.

[36] S. Rippengill, K. Worden, K. M. Holford, R. Pullin, (2003) "Automatic classification of acoustic emission patterns," *Strain: An International Journal for Experimental Mechanics,* Vol. 39 (1), February 2003, pp. 31-41.

[37] G. Manson, K. Worden, K. Holford, R. Pullin, (2001) "Visualization and dimension reduction of acoustic emission data for damage detection," *Journal of Intelligent Materials Systems and Structures*, Vol. 12 (8), pp. 529-536.

[38] MathWorks. Matlab Academy. Machine Learning Course. Certification of completion July 21st, 2020. https://matlabacademy.mathworks.com/R2020a/portal.html?course=mlml#chapter=2&lesson=2&section=6.

[39] D. R. Farrar, K. Worden. (2013) *Structural Health Monitoring: A Machine Learning Perspective*, John Wiley & Sons, Ltd, 631 pages, ISBN 978-1-119-99433-6, 2013.

[40] K. Worden, G. Manson, S. Rippengill, (2009) "Statistical pattern recognition and damage detection in structural health monitoring of civil infrastructure systems," *Structural Health Monitoring of Civil Infrastructure Systems*, pp. 305-335.

[41] Fedderson, C. F., (1967) Discussion, *ASTM STP 410*, pp. 77-79, 1967.

[42] M. A. Hamstad, (2008) "Comparison of wavelet transform and Choi-Williams Distribution to determine group velocities for different acoustic emission sensors," *Journal of the Acoustical Society of America*, Vol. 26, 2008.